International Journal of Polymer Science

Self-healing Nanocomposites

Lead Guest Editor: Sabu Thomas
Guest Editors: Yves Grohens, Poornima Vijayan P, and Hanna J. Maria

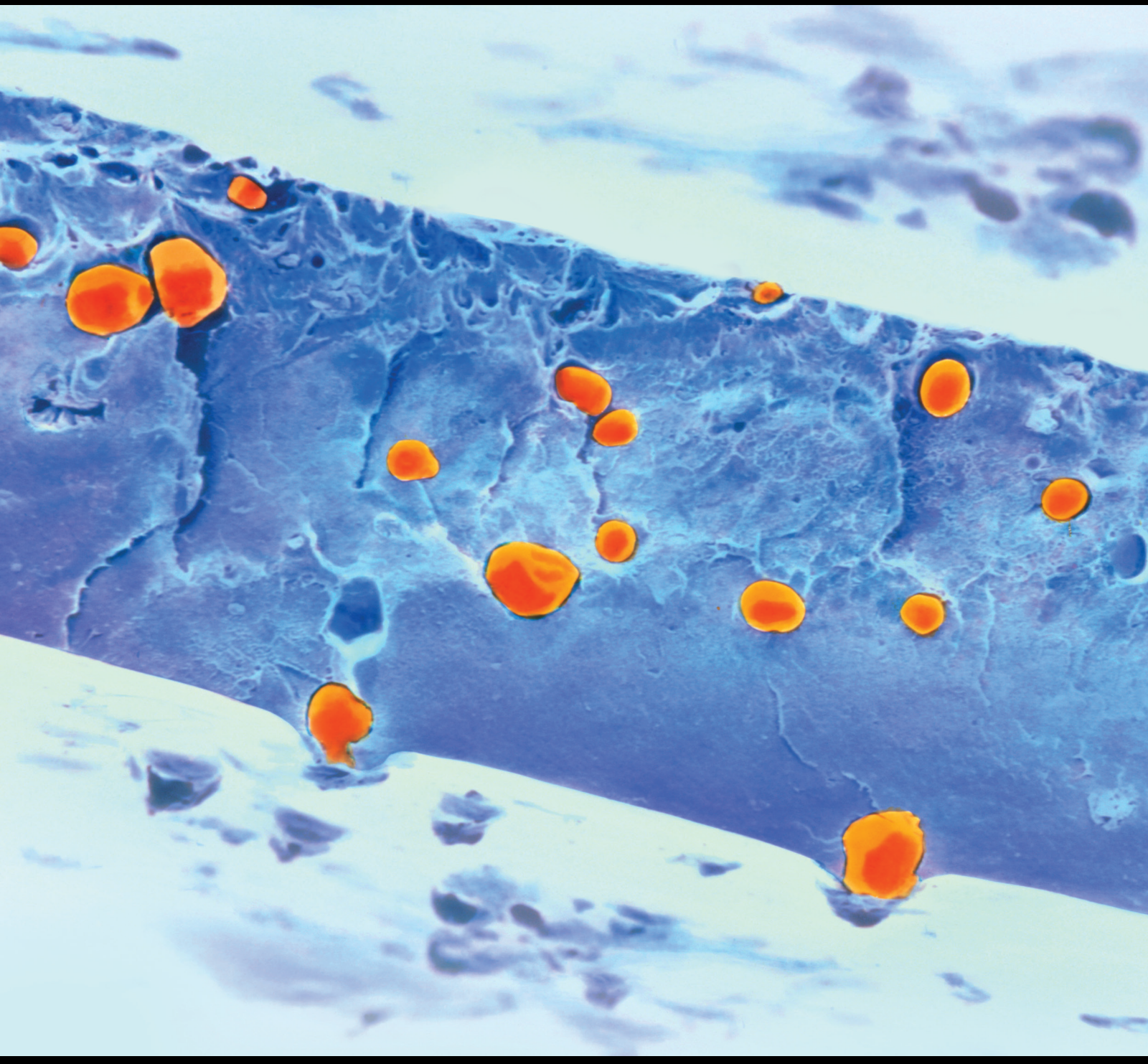

Self-healing Nanocomposites

International Journal of Polymer Science

Self-healing Nanocomposites

Lead Guest Editor: Sabu Thomas
Guest Editors: Yves Grohens, Poornima Vijayan P, and Hanna J. Maria

Contents

Shape Memory Corrosion-Resistant Polymeric Materials
Nathan D. Jacobson and Jude Iroh
Review Article (18 pages), Article ID 5558457, Volume 2021 (2021)

Sugarcane Bagasse-Derived Activated Carbon- (AC-) Epoxy Vitrimer Biocomposite: Thermomechanical and Self-Healing Performance
Balaji Krishnakumar, Debajyoti Bose, Manjeet Singh, R. V. Siva Prasanna Sanka, Velidi V. S. S. Gurunadh, Shailey Singhal, Vijay Parthasarthy, Liberata Guadagno, Poornima Vijayan P, Sabu Thomas, and Sravendra Rana
Research Article (7 pages), Article ID 5561755, Volume 2021 (2021)

Corrosion Resistance Evaluation of Self-Healing Epoxy Coating Based on Dual-Component Capsules Containing Resin and Curing Agent
Alireza Safdari, Saied Nouri Khorasani, Rasoul Esmaeely Neisiany, and Mohammad Sadegh Koochaki
Research Article (13 pages), Article ID 6617138, Volume 2021 (2021)

Evaluation of Corrosion Protection of Self-Healing Coatings Containing Tung and Copaiba Oil Microcapsules
Nicolas Augusto Paolini, Alexandre Gonçalves Cordeiro Neto, Alana Cristine Pellanda, Agne Roani de Carvalho Jorge, Bryan de Barros Soares, João Batista Floriano, Marcos Antonio Coelho Berton, Poornima Vijayan P, and Sabu Thomas
Research Article (13 pages), Article ID 6650499, Volume 2021 (2021)

Performance Evaluation of Layered Double Hydroxides Containing Benzotriazole and Nitrogen Oxides as Autonomic Protection Particles against Corrosion
Alana Cristine Pellanda, Alexandre Gonçalves Cordeiro Neto, Agne Roani de Carvalho Jorge, Marcos Antonio Coelho Berton, João Batista Floriano, Sabu Thomas, and Poornima Vijayan P
Research Article (16 pages), Article ID 6630194, Volume 2021 (2021)

Hindawi
International Journal of Polymer Science
Volume 2021, Article ID 5558457, 18 pages
https://doi.org/10.1155/2021/5558457

Review Article

Shape Memory Corrosion-Resistant Polymeric Materials

Nathan D. Jacobson and Jude Iroh

Department of Materials Engineering, University of Cincinnati, Cincinnati 45221, USA

Correspondence should be addressed to Jude Iroh; irohj@ucmail.uc.edu

Received 12 February 2021; Revised 20 May 2021; Accepted 1 June 2021; Published 30 June 2021

Academic Editor: Poornima Vijayan P

Shape memory alloys, materials capable of being deformed and maintaining the deformation and additionally capable of returning to the initial position, are valued for a range of applications from actuators to flexible microdevices. Maintaining the properties that make them useful, their ability to deform and reform, requires that shape memory alloys must be protected against corrosion, in which the integration of shape memory polymers can act as a means of protection. Thus, this review is to highlight the utility of self-healing shape memory polymers as a means of corrosion inhibition. Therefore, this review discusses the benefits of utilizing self-healing shape memory polymers for the protection of shape memory, several types of self-healing polymers that could be used, means of improving or tailoring the polymers towards specific usages, and future prospects in designing a shape memory polymer for use in corrosion inhibition.

1. Introduction

Composites, or materials that contain two or more chemically distinct parts that are combined macroscopically to form a new material with compositional properties superior to that of their constituent materials, are a key component of modern everyday life, from the buildings people live in to the vehicles that are used. As such, improving and creating new composites is critical to further advancement into stronger, better, and more environmentally friendly materials. Thus, the development of smart composites or advanced composites that have the capability of "sensing" and responding to some external influence is of express interest in tackling the ever-growing list of demands the materials we use need to undertake [1]. One particularly interesting area of composite development includes composites capable of displaying something called the shape memory effect, in which the material is capable of shifting into and maintaining a temporary position, from a permanent base shape as a result of some external stimuli acting upon it, and then returning to the base shape under its own abilities [2], which can be seen in Figure 1.

As shown by the graph above, stress induced by some stimulus, which, depending upon the material, could be electromagnetic radiation, water, pH, temperature, or even a magnetic field, causes a physical change of the material into a certain position and can also trigger it to move back into the original position [2, 4]. This application of stress on the material results in the deformation of the material to the point that the material holds a position under constant strain. If the strain continues to increase, it can reach a point in which reversion occurs and the shape memory material moves to its initial permanent form [3]. This ability makes them desirable for machinery and equipment such as actuators, microdevices, and biomedical equipment or in the aerospace industry for lightweight, deployable structures [5] or for other uses in which shape and position control, the control of vibrations and acoustics, or impact resistance may be desirable from the composite [6]. A key concern in the development of shape memory alloys is the effects of corrosion upon the materials as it can lead to the loss of properties and effectiveness in the material.

2. Shape Memory Composites: Alloys

Shape memory alloys are a combination of metals designed to display shape memory effects through a stress-induced martensite transformation where the parent fcc phase

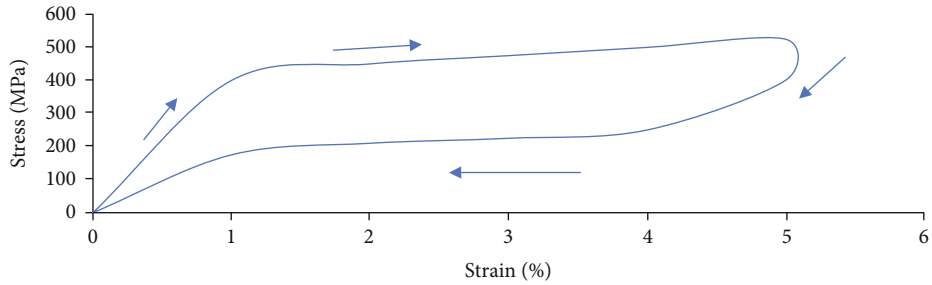

Figure 1: A stress-strain curve demonstrating the shape memory effect of a titanium-nickel shape memory alloy [3].

transforms into an hpc phase [7]. Elaborating further, shape memory alloys will exhibit shape memory effects via induced phase transformations, where they move from a high-temperature austenite phase, in which the alloy is more malleable to deformation, but cooling or the application of stress reverts it to a lower-temperature phase, known as the martensite phase [8]. Material property concerns for shape memory alloys focus particularly upon the alloy's abilities to recover from deformations. When determining the rate of recovery for a shape memory alloy, microscopically speaking, it is considered to be a function of grain size in relation to the dimension of the alloy; this implies that grain size is important for a shape memory alloy; if it decreases, strain hardening occurs because of the free space of dislocations that slide prior to interaction with the grain boundaries decreasing and causes plastic deformation and inhibits martensite transformation and strain recovery. Typically, the more impurities there are within a system, the smaller the grain size is, due to dispersed particles causing a grain boundary pinning effect [9]. However, shape recovery for alloys can be more easily tested for and determined via bending tests where the alloy is bent to a certain angle under a certain maximum strain and then recovery may then be induced by heating to a temperature specific to the alloy and subsequently letting cool to room temperature, which allows for the shape memory ratio to be calculated based on the returning angle of the sample [7]. Nickel-titanium, copper, and iron form the basis for some of the more common shape memory alloys [10, 11]; a brief overview can be found in Table 1.

Additionally, the performance of shape memory alloys may be enhanced through the addition of tertiary or quaternary elements [9, 11]. Typically, these shape memory alloys are reinforced with chromium, aluminum, nickel, manganese, copper, silicon, nitrogen, or rhenium, but the addition and quantity of these elements in the alloy may risk sacrificing the superelasticity of the alloy, especially at room temperature conditions [9]. To counter the negative effects that adding these additives may have on the shape memory effect, some manufacturers use certain techniques; aging is a technique used to improve the shape memory ratio of a shape memory alloy, where the metal alloy is treated at a high temperature for an extended period of time; for example, an iron-based shape memory alloy was tested by Yongren et al. to have a base shape memory ratio of 0.2, but after 4 hours of aging, the shape recovery ratio shot up to around 0.6. Unfortunately, the aging process reduces the ability of the alloy to form a passivating layer, so an aged alloy shows poorer corrosion resistance in comparison to an unaged alloy; there are other developments which would yield good results in terms of corrosion resistance and shape recovery, but these methods tend to be high cost, difficult in terms of "training" the alloy to achieve the desired shapes, result in low recovery stress, and require a high annealing temperature to trigger recovery [7]. Another effect in the addition of other elements to a shape memory alloy is that phase transition temperatures may be increased or decreased, which may also serve to further improve or alter the mechanical properties of the alloy. For instance, the addition of copper can enable nickel-titanium alloys to improve the stability in regard to pseudoelastic behavior, which is good for cyclic mechanical loading. However, the adverse effect of this addition results in the alloy becoming more susceptible to corrosion, as the oxide layer that forms upon the surface is less stable and forms a weaker passivating layer, which enables corrosion attack on the alloy [12], as copper itself provides no additional resistance to the corrosion of the alloy [13]. This brings forth the crux of the issue, in that shape memory alloys have a vulnerability towards corrosion. Corrosion attack on a shape memory alloy focuses on the grain boundaries, in which it may occur on an intergranular level with pitting developing nearby within grains of the shape memory alloy; it is at the grain boundary that precipitates of elements in the alloy, like nickel, form. This intergranular corrosion that occurs at the grain boundary forms zones that reduce corrosion resistance and lead to further degradation of properties [9]. It is possible to help mitigate the corrosion by adding corrosion-preventing elements such as chromium, cobalt, titanium, or even tin in very small amounts to form a quaternary or tertiary shape memory alloy as a means of improving the corrosion resistance [14–16]. However, the addition of these elements may have other, potentially undesirable, effects; for instance, chromium improves the corrosion resistance of the shape memory alloy in exchange for making the alloy more brittle and lowers the transformation temperatures [15], and as Table 2 demonstrates, it is possible to achieve comparable if not greater corrosion resistance without the addition of corrosion-inhibiting elements.

In general, the lower the current density, or I_{corr} value, the better the protection against corrosion; the table above lists several I_{corr} values, three shape memory alloys with corrosion-inhibiting elements, and two polymers. The alloys display good corrosion resistance, whereas the polymers

Table 1: Types of common shape memory alloys.

Alloy	Overview
Copper-based	Low cost and highly practical for most applications. Brittle as a result of large grain size, structure, and abnormal anisotropy [10]
Iron-based	Low-cost, good mechanical properties, usable in high-temperature applications, very workable [9]. Low recoverable strains, poor corrosion resistance, requires additions to the alloy matrix [7]
Nickel-titanium	Outperform iron and copper alloys, most commonly used [11]

Table 2: Current densities of various alloys and polymers.

Material	$I_{\text{corr}}\left(\left(\text{A} * \text{cm}^{-2}\right) * 10^{6}\right)$
Cu-Al-Ni [15]	2.56
Ni-Ti-(1.5%)Co [16]	0.62
Graphene/epoxy ester-siloxane-urea [17]	$4.1 * 10^{-3}$
Ti-Ta-0.37Sn [18]	2.615
Blended polycaprolactone with a crosslinked network [19]	2
Polyaniline-epoxy-poly (methylhydrosiloxane)-divinylbenzene blend [20]	$5.1 * 10^{-4}$

perform better, if not superior, to the shape memory alloys in corrosion inhibition. Therefore, applying a polymer coating capable of displaying the shape memory effect to form a shape memory composite would be highly recommended to preserve the mechanical properties of the shape memory alloy.

3. Shape Memory Composites: Property Considerations

When determining the properties or the overall effectiveness of a shape memory composite, there are many factors to consider; for instance, the shape recovery speed is the ability of the shape memory composite to respond to an external force that has resulted in a deformation of the composite's shape [21], or the plasticity index of the composite, a ratio of the hardness to the elastic modulus, is useful for determining the wear resistance in friction and thereby is useful, along with the functional properties of the memory layer, to help determine the structural state of the shape memory composite under frictional conditions [22]. But when determining the effectiveness of a composite coating in preventing the corrosion of the material underneath, a key factor for consideration would be the hydrophobicity of the surface. The hydrophobicity of a surface is linked to the decreased corrosion rate of a metal through the limitation of interactions with corrosive elements, like water, and with organic coatings; this means limiting the diffusion process of water to the metal underneath [22, 23]. Hydrophobicity is dependent on the coating's chemical properties and the microstructure of the coating's surface, where the surface roughness can enhance the hydrophobicity of the coating [24] and may be measured by determining the wettability of the surface. Wettability is how spreadable water is across a solid surface, the effectiveness of which is determined by the water contact angle, determined by Young's modulus [23], which can be seen in Figure 2.

Shape memory alloys and polymers have been used extensively, and the individual application of either depends upon the demands of the situation, where polymers are used versus alloys because of their low density, being cheap to afford, being able to control what triggers them to recover, the large degree of recoverable strain in which they have the ability to undergo, and the wide range in which one could tailor their response temperatures to (via manipulation of the glass transition temperature); but they are beaten out by shape memory alloys by orders of magnitude greater when the situation calls for higher recovery stress, shorter recovery time, and a vastly larger amount of cycles they can undergo before failure [1] and have better thermal stability and higher elastic modulus [8]. It is worth noting that circumstances in play may mean that what would normally be negative in whether it should be used or not, like the long recovery times of shape memory polymers, can instead confer an advantage in their use [1].

There are many different models to predict the thermomechanical properties of a shape memory material. For example, shape memory polymers act partly springlike, and as per Pan et al., a model for determining the thermomechanical behavior for a particle-reinforced shape memory polymer in 1D may be shown as

$$\sigma(t) + \frac{\eta'(T)}{E(T)}\sigma^{*}(t) = \frac{\eta'(T)E(T)}{E_1(T)}\varepsilon(t) + \eta'(T)\varepsilon'(t), \quad (1)$$

where

$$\varepsilon(t) = \varepsilon^{\text{Total}}(t) - \alpha\Delta T, \quad (2)$$

$$E(T) = E_1(T) + E_2(T), \quad (3)$$

$$\tau(T) = \frac{\eta'(T)}{E_2(T)}. \quad (4)$$

σ is the total stress, $\varepsilon^{\text{Total}}$ is the total strain, ε is the mechanical strain, α is the thermal expansion, η is the viscosity, t is the time, and T is the temperature [26].

For a shape memory alloy, the model is much different as the formula for a 1D constitutive model is

$$\sigma = D(\xi)(\varepsilon - \varepsilon_l\xi_S) + \Theta(T - T_0), \quad (5)$$

where

$$\xi = \xi_S + \xi_T, \quad (6)$$

and ξ is the total martensite volume fraction, ξ_S is the stress-induced martensite volume fraction, ξ_T is the temperature-induced martensite volume fraction, σ is the stress, D is Young's modulus of the shape memory alloy that is

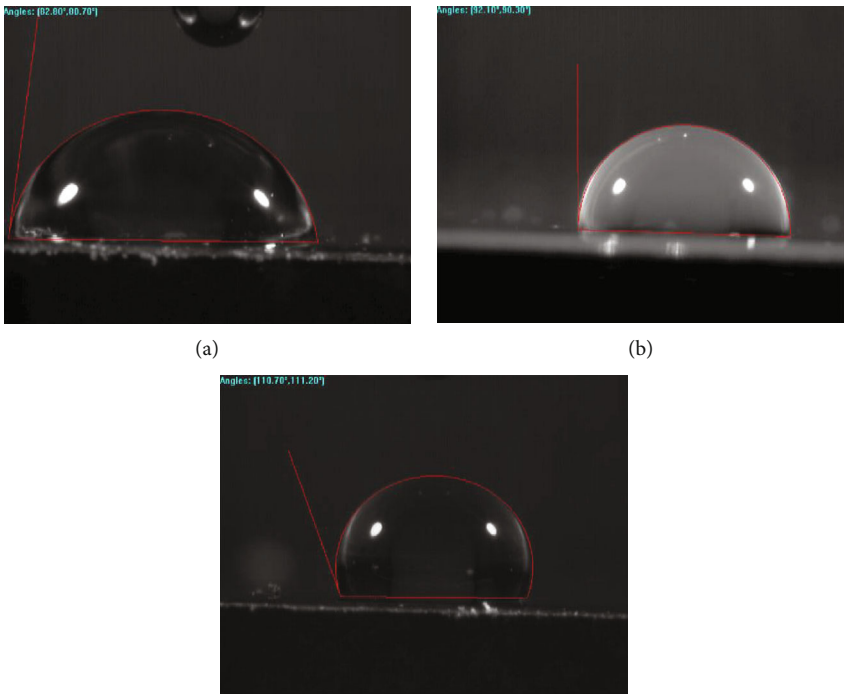

Figure 2: Images of water contact angles: (a) neat polyimide, (b) neat polyurea, and (c) poly(urea-imide) (50% polyurea). Courtesy of Feng and Iroh [25].

dependent on ξ, ε is the strain, ε_l is the maximum recoverable strain, Θ is the thermal coefficient of expansion, T is the current temperature, and T_0 is the reference temperature [27]. These models try to simulate results similar to those shown in Figures 3 and 4.

Polymers function through the potential interactions of thermosets and thermoplastics, where thermosets are defined by their chemical crosslinks that form a three-dimensional network that can extend to an infinite length and thermoplastics lack the interconnected chemical crosslinks and only have a finite length. Processing thermoplastics involves rapid cooling and solidifying viscous polymer melts. Thermoset processing requires the reaction of low-viscosity precursors, and the rate of processing is limited by the rate of the reaction kinetics. Between the two, thermosets tend to have higher dimensional stability and creep resistance, making them preferred for structural composite applications over thermoplastics [28]. By blending these polymers together, one may customize, to a certain extent, the properties of the shape memory polymer, with the base polymer producing the shape memory effect and other polymers for overall cohesion and deformability (for example, after elongation, the crystallinity provided by the other polymers prevents the elastomer from relaxing back into its initial state) [29]. Other advantages for polymers in their usage as materials are their low density, their ease of processability, the ability to withstand strain rates of up to 800%, resistance to corrosion or electricity, how lightweight they are, and the broad range of properties that the building blocks they are composed of [2, 30]. Polymer-based shape memory composites and coatings must also be concerned with the glass transition temperature, or T_g, given that the polymer will be in a glassy state prior to this point and thereby will affect the shape memory characteristics of said composite; countering this would require that the filler material be capable of inhibiting the thermomechanical effects that the polymer exhibits; these thermomechanical effects are typically demonstrated by friction interactions that resist external loading [21]. For shape memory polymers, this is typically more dependent on the glass transition temperature, also known as the T_g, where phase changes occur above the T_g, where it becomes rubbery, and the position sets once the polymer moves below the T_g as it turns into a glassy state [2]. Given that shape memory composites require the application of external energy to return to their primary form, the composite's thermal absorption and conductivity are necessary factors to consider, as, generally, the greater the ability for a composite to absorb or conduct energy results in better shape recovery times and less energy consumed to exhibit said response times [21]. However, there are demerits in using shape memory polymers, as functionality may be lost over time; thus, a means of countering such loss in effectiveness is important in extending a shape memory polymer's lifespan and its ability to withstand environmental conditions.

4. Shape Memory Composites: Polymers and Polymer Blends

Traditional polymers are fairly inert to the environment, which means a gradual loss of functionality over time [30], especially in the form of microcracks, the most serious challenge that polymers face in long-term applications, as they decrease the lifetime of the material and are much more

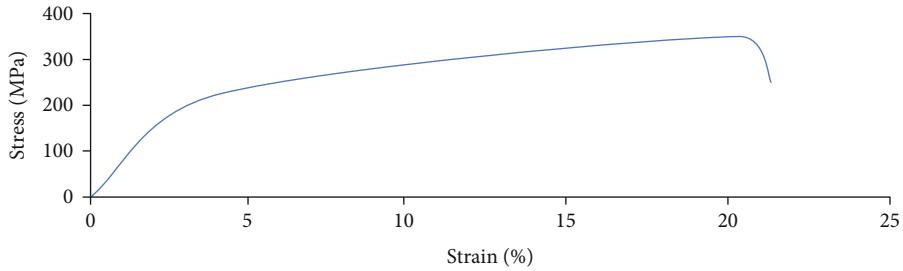

Figure 3: Ni-Ti shape memory alloy stress-strain curve (transitions start at 89.11°C and end at 86.33°C for the martensite phase, and the austenite phase begins at -22.73°C and ends at around 91.96°C) [18].

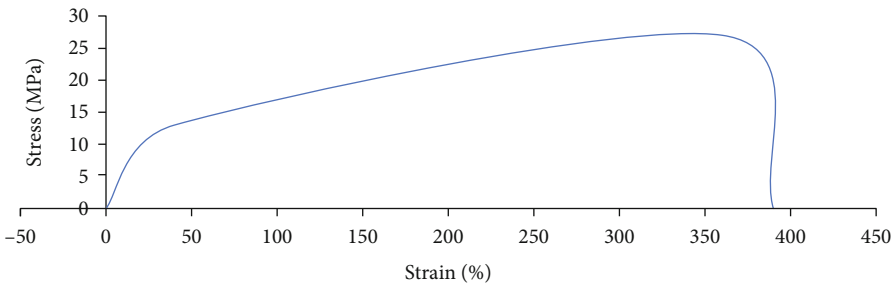

Figure 4: Polycaprolactone polymer (T_m of 51.7°C) stress-strain curve [19].

difficult to detect or repair [31]. Hence, polymers require some means of maintaining and repairing their functionality, either by means of some external application or, more optimally, by a trait inherent to the polymer or polymer blend; in other words, the polymer must have the inherent capability to heal itself. As the polymer is a shape memory material, stress resulting from a variety of triggers, such as chemical, mechanical, or thermal, can result in mechanical deformation in the material and additionally may activate a healing response towards physical damage that has been generated [32]. Commonly, crack healing occurs because of thermal effects and is initiated at or above T_g. As such, developments have typically focused on adjusting the effective T_g to the desired temperature, which is typically lower than a polymer's normal T_g [31]. Accomplishing self-healing for polymers includes two different approaches that rely upon different chemical interactions to achieve the objective: one is through supramolecular forces, and the other is by dynamic covalent bonds formed within the polymer blend. First, though, is the primary means by which the polymer adheres to the surface. Interfacial adhesion between the polymer matrix and the 2D filler is an important part of property enhancement and being able to reproduce the desired results. Strong interfacial bonding between the polymer matrix and the 2D filler gives the polymer coating a high modulus and tensile strength, improves hardness, and increases coating resistance to tear, fatigue, and corrosion [17]. Thusly, the formation of a shape memory composite between a polymer and an alloy necessitates the use of coupling agents, like trimethoxysilylpropyl methacrylate, to form the connection between the organic and inorganic phases of the coating, as the lack of such connection compromises the overall mechanical properties because organic materials do not adhere well to inorganic materials [33]. One of the most effective choices for corrosion inhibition and recommended options for coupling agents includes polysiloxanes. Polysiloxanes are hydrophobic polymers capable of improving the corrosion resistance of a polymer blend by limiting water's ability to access the metal/hybrid polymer coating interface [17]. Characterized by a Si-O-Si group, which has a bond angle between 104 and 180 degrees attached to the polymer chain, the degree range of the bond angle affects the flexibility chain and improves the bond energy, forming the basis for the notable durability and resistance to heat that polysiloxanes have [34].

4.1. Polydimethylsiloxane. One of the most commonly used polysiloxanes is polydimethylsiloxane, abbreviated to PDMS. PDMS elastomers are typically formed from crosslinking linear polymers that have been entangled and are stiffer than the threshold value for the dense entanglements that act effectively as crosslinks [35]; the structure may be found in Figure 5. One method in which PDMS could be improved for usage is reducing the stiffness of PDMS elastomers that would reduce the energy necessary for deformation. This is critical for improved adherence to an object that would otherwise be difficult to apply a coating to, and accomplishing this would mean an overall reduction in the density of the crosslinks. Applying a solvent can accomplish the reduction in the density, but the solvent can leach out and potentially harm the surrounding environment. PDMS cannot have a shear modulus lower than 200 kPa. By forming a crosslinking bottlebrush matrix as opposed to a linear polymer, it is possible to inhibit entanglement formation and form a

controllable elastic modulus that can range from 1 to 100kPa, where the modulus corresponds linearly to the density of the crosslinking chains. Additionally, there can be independent control over the loss modulus; it reduces adhesiveness, can be relatively simple to produce, and may be furthered tuned via the backbone/side chain/crosslinking chain ratio to further tailor the mechanical properties [35].

4.2. Polymethylhydrosiloxane. Of the polysiloxanes available, polymethylhydrosiloxane, or PMHS for short, is a particular siloxane of choice as it is nontoxic, is stable in air, is resistant to high temperatures, and can be used as a reducing agent for the conversion of carbonyls to alcohols [17, 33]; the structure may be found in Figure 6. PMHS has low surface energy and good innate hydrophobicity and, thanks to its inorganic and organic molecular parts, acts as a good coupling agent between polymers and metal surfaces. PMHS is useful as no organic solvent is necessary to prepare the coating, which is important given the restrictions in volatile organic compounds that can be considered hazardous to the environment. Despite this, the application of PMHS as an anticorrosion measure is relatively rare. The effectiveness in the addition of PMHS may be demonstrated by an experiment performed by Sun et al. where PMHS was added to a polyaniline-epoxy coating. This successfully reduced the overall surface energy of the coating, improving the wettability, and formed small protuberances on the surface, which allowed for a layer of air to form and inhibit contact by a corrosive solution and the adsorption of the solution's corrosive ions, resulting in an increase in the effectiveness of the coating to 70 days, whereas the coating without PMHS had only lasted 34 days [20].

4.3. Supramolecular Polymers. Supramolecular bond-based self-healing material has polymer bonds that are connected by sticker-like behavior, in that they can connect and reconnect, and it is this stickiness that gives the material strength; it is important to note that this does not come from covalent bonds or chain entanglements. These bonds affect the polymer blend's strength, viscosity, flow, and ordering of its polymer chains within and therefore have a relationship with the dynamic behavior the polymer exhibits. Once the damage has occurred to the structure, the interface of the damaged surfaces will then have unbound supramolecular bonds that remain "sticky" and are capable of being recombined and reformed to close the damage and revert to the previous undamaged state of being. In using supramolecular bonds, the central concerns are the time it takes for recovery to occur, the strength of the material, and the material's ability to recover properties after damage [32]. Some examples of polymers to use in a blend that relies upon supramolecular forces to accomplish self-healing are as follows.

4.3.1. Epoxy Ester. Epoxy ester resins are known to have good corrosion-inhibiting properties and adhesion to surfaces but are restricted in use because of their poor chemical resistance and weak mechanical properties; as such, it is recommended to improve them through the use of blending or copolymerization with other polymers that are capable of resisting high

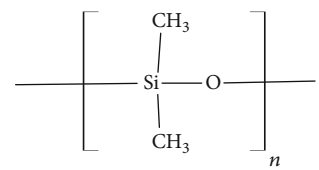

Figure 5: Polydimethylsiloxane.

temperatures like polyurea or polysiloxane [17, 33]; the representation of the structure may be found in Figure 7. Polyurea is typically used for laminates in buildings and the automotive industry, where it can improve the impact and blast resistance of the epoxy ester [17]. Epoxy esters are also limited by their highly reactive rings, which inhibits processability for polymer blends and thereby makes them more expensive to produce. Generally, when reacting epoxy esters to produce certain polymers, the epoxy functional groups are opened through the esterification of unsaturated fatty acids to then form alkyd-modified epoxy esters, with properties controlled by means like the level of unsaturation or the chain length. The produced epoxy ester emulsion is then dehydrated through the evaporation of water to coalesce and form a film, which is cured through autoxidation, or oxygen reaction to cause a free radical chain mechanism. The outcome of the properties depends upon the oil chain length. For instance, long oil chains in epoxy esters mean lower chemical resistance, longer drying times, and enhanced ability to penetrate and seal poorly cleaned surfaces, whereas short oil chains are hard and brittle and have good chemical and moisture resistance [36].

4.3.2. Polyimide. In general, polyimides are favored in engineering applications as they possess outstanding mechanical properties, great thermal stability, a high glass transition temperature, and a low dielectric constant [36]; a representation of the structure may be found in Figure 8. Most studies that focus on self-healing polymers are ones that operate under low or medium T_g, whereas high T_g polymers, which would be suited for self-deployable aerospace or jet propulsion applications, are not as well studied. A shape memory variant of polyimide would be one such polymer, as it is capable of high T_g, with temperatures around 218°C, and self-healing (which occurs at 243°C) at the cost of lowered mechanical properties and a lower T_g (235°C) for the non-self-healing variant than the non-self-healing variant, but that may well be due to the polystyrene, and another material may be better suited [37]. Polyimides are defined by a rigid heterocyclic imide functional group and are noted for the interaction of their electron-rich nitrogen atom and their electron-deficient carbonyl group located in the backbone of the polyimide [38]. However, polyimides tend to be limited for their use due to poor moisture absorption and adhesion, which can lead to interfacial failure and limits them to a more moderate coating lifespan as compared to other coatings, as well as their high surface energy and dielectric constant [36, 38]. Overcoming these limitations typically means inserting hydrophobic polymer blocks into the backbone of the

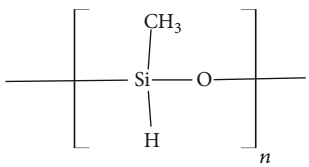

Figure 6: Polymethylhydrosiloxane.

polyimide or incorporating nanoparticles into the matrix as a means of reducing diffusivity and relative permittivity of the polyimide coating [38]. Including nanoparticles has the drawback of increasing the surface energy for the polyimide, which in turn reduces its adhesion, whereas the inclusion of polymer blocks into the backbone can reduce the decomposition temperature and thereby the service temperature and mechanical properties [38]. Durability relates to the retention of the barrier properties held by the polymer coating and is, for polymers, controlled by the crystallinity within the coating. A decrease in the surface energy of the coating is related to an increase in coating resistance [25]. Polysiloxanes can be utilized for improved energy dissipation, flexibility, and surface adhesion, but as a trade-off, they reduce the ultimate strength and Young's modulus; therefore, mitigating these detractions primarily requires manipulation of the molecular weight percent of polysiloxane. For Young's modulus to remain close to that of plain polyimide, the polysiloxane weight percent must be between 10 and 20%; it is worth noting that ductility significantly improves for the copolymer if polysiloxane is within 10 to 40 wt%. Overall, attaching a polysiloxane to the backbone of the polyimide chain improves the overall processability of the polymer, inhibits the absorption of water, makes the polymer more capable of adhering to a wide range of surfaces, improves the thermal stability, and decreases the decomposition temperature in relation to an increase in the wt% of polysiloxane in the polymer (this appears to be more related to the reduction in polyimide). The drawbacks of the polyimide-polysiloxane chains could be overcome through the addition of other copolymers, like polyphenylsilsesquioxane, which is a suggested polymer that could also further improve the decomposition temperature of the polymer blend. Introducing an ester group to the imide backbone produces the effect of increased flexibility of the polymer but reduces the glass transition temperature, where the combined poly(ester-imide) molecule has a glass transition temperature of 185°C and further analysis has shown that it loses 10 wt% of its mass in air at 300°C [33]. Because the T_g of a polymer blend is not the actual average of the T_g of the polymers that make up the blend, in fact, it appears to act more like a range that varies depending upon the composition of the bulk, the architecture of the blend, the molecular weight of the polymers, and other factors. At the lower end of this range, thermal activation occurs but is hindered by steric constraints, the severity of which may be determined by the relative rate of component dynamics [36].

4.3.3. Polyurea. Polyurea is a semicrystalline polymer prized for its piezoelectric abilities, often used as an insulator, and can exhibit high-temperature stability with a piezoelectric e constant of 15 mC/m^2 that remains so until it reaches temperatures of 200°C [38]; a representation of the structure may be found in Figure 9. If blended with polyimide, the hydrogen bond donors and acceptors within the blend enable self-assembly in addition to an ultralow dielectric constant, a value between 1.56 and 1.94 with any decrease corresponding to an increase in the concentration of polyurea, which would be immensely beneficial in the inhibition of corrosion [25, 38]; a representation of the polyimide-polyurea blend may be seen in Figure 10.

Additionally, for the created poly(urea-imide) blend, two rubbery plateau regions occur exponentially as a result of two T_g regions caused by the mole fraction content of polyurea in the polyimide block chain, which in turn increases the storage modulus of the polymer. The T_g of copolymers increases with an increase of concentration of a high-T_g component, where a sharper effect occurs with the addition of a slightly higher amount of polyurea to the polyimide (it is worth noting that the degree of imidization has little bearing on this behavior as it decreases as the polyurea mole fraction increases) as a result of the self-supporting, complementary hydrogen bonding [38]. As a result, polyimide-b-polyurea forms a coating with an expected lifetime of 8 years, higher than that of polyimide, providing superior corrosion resistance [25], which can be seen in Figures 11(a) and 11(b).

4.4. Dynamic Covalent Bonds. Briefly stated, dynamic covalent bonds are the classic covalent bonds that form up traditional polymers but have the additional capability of being reversible under equilibrium conditions, like noncovalent bonds, where the reformation of bonds occurs within seconds or minutes [30]. Networks formed by these dynamic covalent bonds have the benefits of thermoset polymers and act as thermosets under certain conditions but have the reprocessability that thermoplastics are known for. The main drawback that can occur is that dynamic covalent bonds may sacrifice the creep resistance of the material as they may be activated when not needed and therefore cause creep within the material; this may be controlled using thermal phase transition temperatures to lock in the polymer until sufficient energy can unlock and trigger shape memory or self-healing effects [28].

4.4.1. Siloxane-Poly(methyl methacrylate). Siloxane-poly(-methyl methacrylate), also known as siloxane-PMMA, has excellent corrosion-resistant and adhesive properties for less environmental impact than coatings such as chromate-based coatings. These silica-PMMA films are noted not only in their low preparation temperature, cheap processing cost, and ability to remain homogeneous as applied across large-area substrates but also in their vulnerability to brittleness from chemicals like water, methanol, and ethanol, especially after thermal treatment [33]; a representation of the structure may be found in Figure 12. Preparation typically can involve the usage of water acidified with chemicals such as nitric or hydrochloric acids as a means of enhancing corrosion resistance, but this treatment process risks the formation of Cl^- ions that may form corrosive agents, and the high acidity of the hybrid may instead act to compromise the substrate

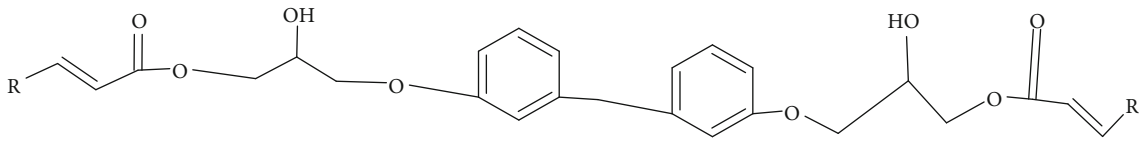

Figure 7: Epoxy ester.

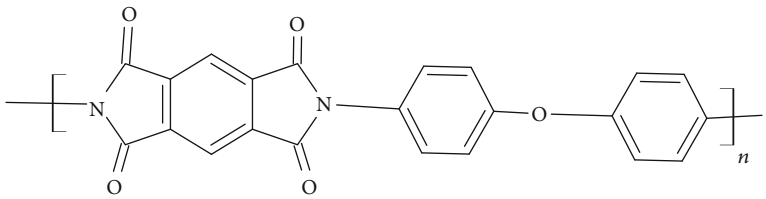

Figure 8: Polyimide polymer.

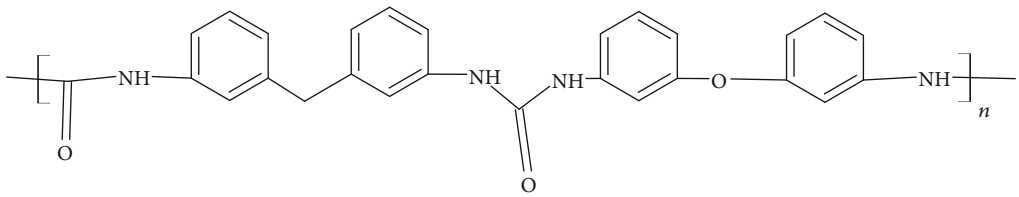

Figure 9: Polyurea.

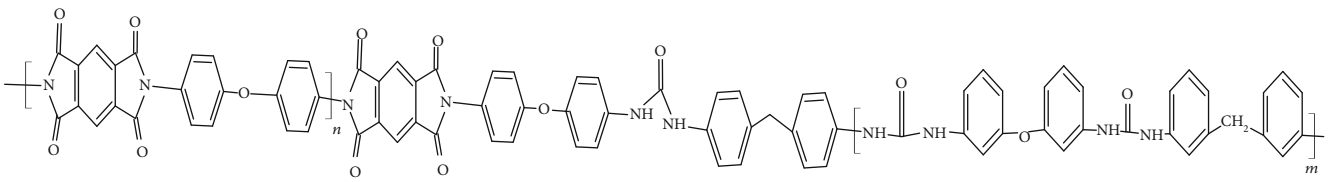

Figure 10: Polyimide-b-polyurea supramacromolecule.

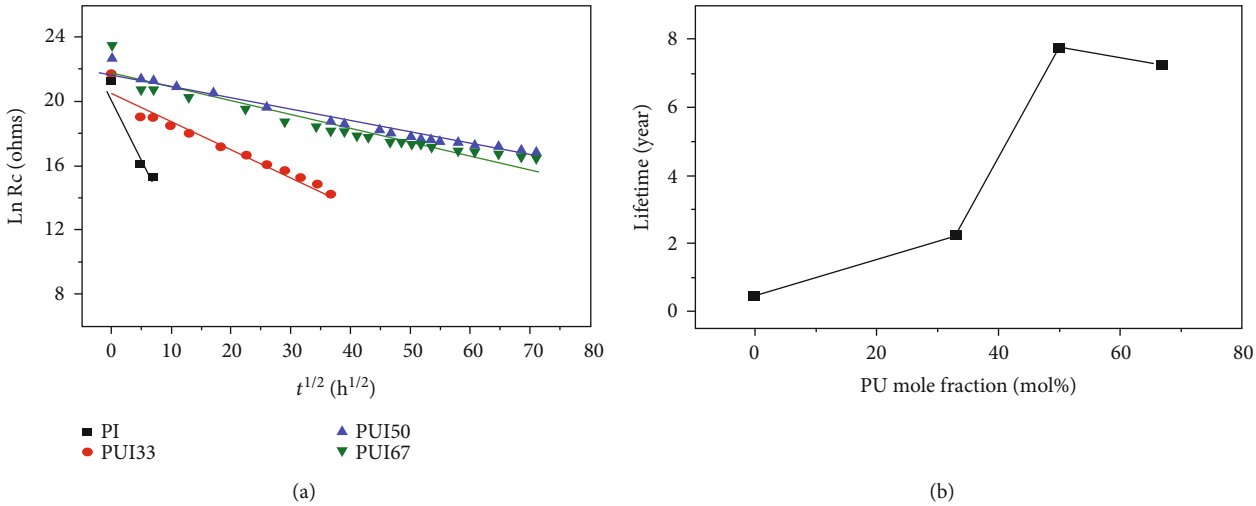

Figure 11: (a) The projected lifetimes of poly(urea-imide) coatings with varying concentrations of polyurea applied to aluminum. (b) The coating lifetime compared to the % mole fraction of polyurea. Courtesy of Feng and Iroh [25].

rather than protect it. A change in the formulation of the coating will result in a change of the film's formation characteristics, and thus, an environmentally friendly coating must be prepared through an environmentally friendly precursor solution. Porous films promote crack and discontinuity formations that cause the barrier to fail and reduce the overall corrosion resistance to decrease. Silane films that are more hydrophobic are better at protecting metals as barrier and adhesion properties are dependent on the time of exposure to either air or water as Si-O-Si bonds are vulnerable to hydrolysis reactions provided by exposure [34].

4.4.2. Hydrazones: Self-Healing and Shape Memory Materials. Acylhydrazones are formed from the condensation of hydrazine and carbonyl compounds and may be catalyzed in the presence of acid to make their C=N bonds more pH-responsive [30]; the structure may be found in Figure 13. Acylhydrazones are more resistant to water than amines and, under mild conditions, may be considered a dynamic molecule capable of reshuffling with other hydrazones or in the presence of differing hydrazines. Most importantly, however, they are responsive to the pH of the surrounding environment, where their formation is catalyzed in the presence of acids and the formation is reduced in more basic environments. Alternating copolymers can, with hydrazones, access different polymer compositions and functions through the exchange of monomers, allowing for tunable mechanical properties. Siloxanes can be used as a spacer to form a stretchy, soft hydrazone film, and if reacted in acid with a harder, more rigid hydrazone, monomers are exchanged between the two to form a new copolymer whose properties are determined by the monomer exchange rate and how the monomers are exchanged. Additionally, a polyacylhydrazone may achieve self-healing through the addition of a polysiloxane unit and allows for deformation recovery to occur over the course of several hours without the need for heating [30].

4.4.3. Diels-Alder Reactions. A Diels-Alder reaction occurs through a cycloaddition reaction in which a conjugated diene and a double-bond dienophile form a six-membered cyclohexane ring; most applications make a reactant electron-rich, otherwise known as the diene, and another reactant electron-poor, which is known as the dienophile. The result is an exothermic reaction; therefore, the inverse reaction, or retro-Diels-Alder reaction, is an endothermic process and thusly requires heat to proceed. Diels-Alder reactions are self-contained and do not require a catalyst nor the addition of any other materials; as such, most Diels-Alder-based dynamic covalent polymers are network polymers [30]; a representation of the general reaction may be found in Figure 14. Diels-Alder cycloadducts or other molecules that form dynamic covalent bonds or have supramolecular interactions have been used to achieve intrinsic self-healing in thermoset polymers through reversible/dynamic interactions. These chemistries enable for fabrication of crosslinked networks capable of healing and improve mechanical properties and thermal and chemical stabilities of the polymer being enhanced. DA adducts form at low temperatures (90°C) and

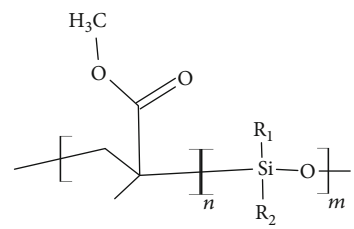

Figure 12: Siloxane-poly(methyl methacrylate) copolymer.

can store shape memory in the polymer structure by way of crystallization and vitrification, which are capable of triggering physical phase transitions through thermal means, which has the added bonus of closing cracks and thereby assists in the coating's healing process. Dense crosslinking promotes mechanical properties of a polymer but risks reducing polymer flexibility and healing ability. Thus, healing a polymer with DA reaction means undergoing a retreatment process at a retro-DA temperature of 120 to 150°C, as it causes partial debonding that enhances molecular mobility; unfortunately, this process may result in the loss of the polymer's reversibility and continued healing in addition to the inefficient curing of DA. It has been suggested that the copolymerization of a siloxane, such as polydimethylsiloxane (PDMS) with polyurethane to assist in the closure of cracks, the flexibility of the polymer, and the reconstruction of DA bonds improve mechanical properties, as PDMS can hinder the crystallization of the urethane to preserve mobility [39]. Improving the properties of a polysiloxane polymer may be achieved through the incorporation of inorganic nanoparticles and may utilize the nanoparticles as crosslinkers to further improve self-healing. The molecular structure of the coupling agent, the spacer length, helps to determine the healing properties for Diels-Alder self-healing polymers, as long spacer groups appear to promote the transition state of the Diels-Alder reaction better [40]. As far as shape memory goes, DA bonds are preserved below the T_g but can be activated above the T_g to initiate the healing and reconstruction of broken bonds. The healing efficiency of a DA-PDMS-PU copolymer was improved over the DA polymer as the flexible PDMS segments enhanced the overall flexibility of reversible units and the reaction kinetics of the healing process at a mild temperature [39].

5. Shape Memory Composites: Coating Additives

Another factor of consideration is that the grain size of the surface layer of composite materials can affect the properties of the composite, ranging from elasticity to strain resistance; as such, choosing the correct material for the composite application is a key component in designing a new shape memory composite [22]. Thus, the addition of fillers may serve as a means to further enhance the polymer composite; some types of fillers may be seen in Table 3.

Conductive fillers are especially important to shape memory polymers, as polymers suffer from a very low

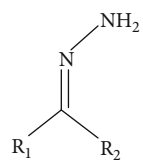

Figure 13: Hydrazone.

thermal conductivity on the order of somewhere between 0.15 and 0.3 W/m ∗ K, which make for better insulators; thus, conductive fillers are added with greater conductive effect proportional to their weight percent within the polymer composite. There is a drawback to such fillers though, as they can inhibit shape deformation and recovery versus that of a purer shape memory polymer; this effect is more pronounced with larger particles [21]. For example, the addition of silicon-carbon and silicon-oxide fillers to around 40 wt% inhibits the shape memory composite's ability to recover completely from deformation [5]. Carbon fillers form a number of possible nanoparticles capable of being used as fillers within the matrix, with several notable carbon fillers being carbon black, nanotubes, or graphene [2, 4, 5]; a figure of a graphene-polymer composite is shown in Figure 15.

Graphene is a useful polymer coating filler thanks in part to its low mass density, high modulus, and high strength and can also work to improve the corrosion resistance of the coating as it is impermeable to gases or liquids that might act to corrode the metal beneath the coating; ultrathin nanosheets have even been tested successfully as a protective film. Graphene is very transparent, so coatings preserve the optical properties of the metal; they also have a high surface area and promote great adhesion between the nanofiller and the matrix [17]. Graphene is capable of improving the rubbery plateau modulus by up to 400,000 vol% when added to form a polyimide composite and can improve Young's modulus, ultimate strength, and glass transition temperature when used to form other polymer composites. If there is an area of concern, it is that the surface properties need to be tailored to suit the desired application, as surface charge, hydrophilicity, and wettability that are changed by the inclusion of graphene will affect cell attachment and polymer performance regarding the applied surface [41]. Carbon nanotubes, on the other hand, can reinforce and enhance shape memory effects, can improve electric-based shape memory recovery, and can be used for the creation of complex composite systems capable of being tuned for specific purposes and the enhancement of the shape memory polymer's ability to respond [4]. Metals and their oxide forms are often chosen in the fabrication of electronic devices [5], and because of their conductivity, some, like ferrite, can even be affected by magnets. This enables shape memory transformation as the metallic particles can generate heat when exposed to a very strong magnetic field. If there is a major drawback, it is that polymers and metals have differing interfacial properties that make them somewhat incompatible to use as a filler. Additionally, it is worth noting that the alignment of the filler can affect the polymer as well. As an example, with the addition of carbon nanotubes to a thermoplastic shape memory polymer, the carbon nanotubes aligned with the direction of the force applied to the polymer. This resulted in a change to the overall shape stability, affected how the polymer recovered to a permanent shape, and changed the crystalline distribution within the polymer matrix [42].

Shape memory effects on self-healing are insufficient enough when applied to deep cuts and as such require the utilization of other methods of corrosion prevention [43]. One of the more common approaches of enhancing corrosion prevention is to embed corrosion inhibitors into the matrix; these can act as healing agents and thereby leach into any defects, allowing for the suppression of corrosion. For coatings that include inhibitors, healing is determined by inhibition of corrosion versus the coating's ability to repair the matrix barrier properties and is therefore irreversible in terms of reaction, and the amount of inhibitors located in the matrix is limited, as large quantities will lead to loss of desired matrix properties. Coating matrix mobility provides for the restoration of corrosion protection of the coating and is usually initiated through the usage of heat or light. Heating above T_g allows for physical closure as the coating would soften and trigger shape memory effects and thereby partly restore barrier properties; this process may be further enhanced by a corrosion sensing component capable of locating damage and healing it or at least preventing further possible damage [44]. Some corrosion inhibitors include benzotriazole, 8-hydroxyquinoline, or inhibitors that are cerium-based. Corrosion inhibitors leach out after damage has occurred to form a barrier film onto the exposed surface. High concentrations of corrosion inhibitors promote greater corrosion resistance but may cause a reduction in mechanical properties. Corrosion inhibitors appear to not affect the rate at which water penetrates the matrix; as such, damage that has been healed may still allow for corrosion to occur, especially in areas where damage once took place [24]. Inhibitors are typically designed to last around 6 to 8 years, in other words, at least until the next maintenance period. Organic coatings typically absorb water via defects into pores within the coating whereby inhibitor pigments may then dissociate and dissolve [45]. Triazole and thiazole are generally used as corrosion inhibitors for aluminum, especially in lieu of toxic chromium-based anticorrosive agents. 2-Mercaptobenzothiazole (MBT) is favored as it adsorbs to aluminum alloy surfaces to form a thin, protective film; however, MBT and other corrosion inhibitors do not work well with a polymer coating as they can deactivate and do not provide the desired corrosion protection [46]. Chromate coatings are the baseline corrosion inhibitor, and high levels can slow the crack growth rate but can be considered environmentally harmful [45]. Adding micro- or nanocapsules has the possibility of reducing the barrier properties depending upon the size of the container or if the container is incompatible with the matrix. The desired trigger mechanism plays a strong role in determining how to encapsulate the inhibitor, alongside the type of matrix and inhibitor that will be used. Common methods of activation are local changes in pH, mechanical rupture, and ion exchange. Ion exchange occurs by containers containing corrosion-inhibiting anions that are released, which allow for more aggressive anions, like chloride, to replace them [46]. If the inhibitor is mixed with the coating,

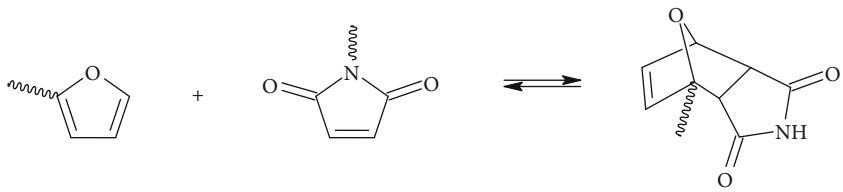

Figure 14: Representation of a general Diels-Alder reaction.

Table 3: Types of fillers and their roles within the polymer matrix.

Filler type	Filler role
Fiber or fiber particulates	Increase mechanical properties but at the expense of shape memory abilities [21]
Silicon-carbon or silicon-oxide	Improve mechanical responsiveness, properties, and recovery times. Are most typically used due to their prevalence [5]
Carbon-based fillers	Enhances mechanical properties and converts energy, such as heat or electricity, to trigger shape memory effect [2, 4, 5]
Metals/metal oxides	Good mechanical properties, more conductive than carbon fillers, can achieve good biocompatibility in the nanoparticle form [5]
Cellulose	Biodegradable, can easily generate and break hydrogen bonds, allows for water-triggered shape memory responses [5]

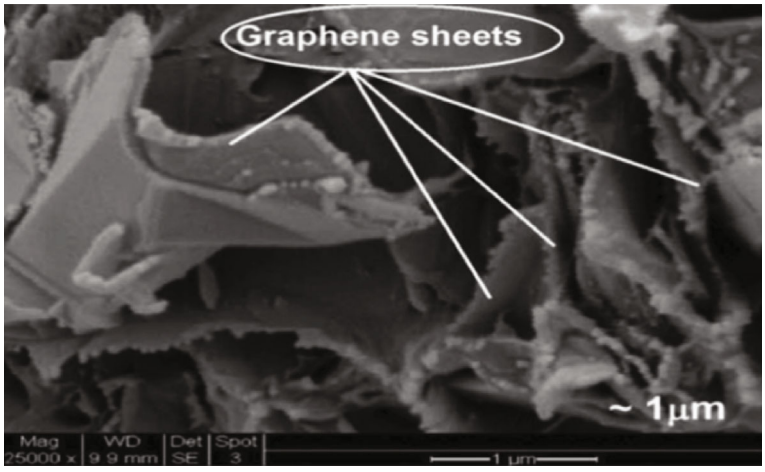

Figure 15: SEM micrograph that shows the cross-sectional morphology of a nanographene sheet-clay composite, coated with polyimide. Courtesy of Longun et al. [41].

the inhibitor gets dissolved in the solution and creates micropores when the solution is applied as a coating. Metal-organic frameworks are a type of encapsulating method where metal ions are connected by organic linkers; they operate by releasing the inhibitor to form an adsorption layer on the exposed surface, and then the metal-organic framework itself impedes any penetration by electrolytes or further corrosion around the afflicted area. A key desired ability of any capsule is the controlled release of inhibitors, to not prematurely expend the limited agent within, thereby giving the coating more longevity in application [47]. Proper storage of corrosion inhibitors reduces leaks, prevents the inhibitors from interacting with the matrix, and can improve the amount of inhibitors stored within. Generally, the preferred containers for corrosion inhibitors are nanoparticles that have large nanocavities, have large surface areas, are very stable, and have low density. Hollow containers are far more capable of storing great amounts of inhibitors than other carriers. Typical container materials are calcium carbonate, titanium oxide, halloysite nanotubes, mesoporous silica, and cerium oxide. Most release methods are typically triggered because of chemical damage or pH changes, as they are common causes of damage to the metal. Inorganic containers have the benefit of being able to be more easily dispersed throughout the polymer matrix and may have additional anticorrosion properties themselves [48].

Capsules that contain a healing agent could be dispersed throughout a polymer matrix, whereupon damage to the matrix may act to trigger the self-healing by causing polymerization to occur from the agents within the capsule. Desirable properties for such a capsule are long shelf life,

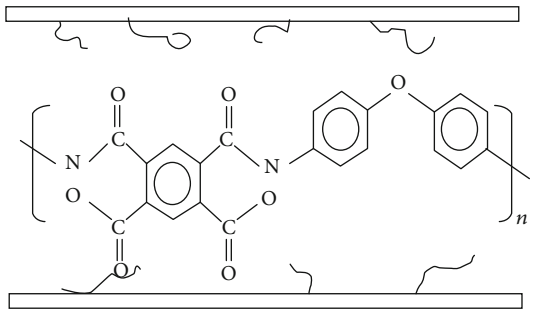

Figure 16: Representation of intercalation of the montmorillonite clay stack. Courtesy of Wang et al. [53].

the strength to maintain structural stability until self-healing needs to occur, and being able to demonstrate excellent bonding to the host matrix. The development of submicrons and nanocapsules could allow for smaller interstitial spacing. Particulate fillers significantly influence the mechanical properties of a material, and depending on the filler, they may sometimes affect the polymer beneficially, like increasing the fracture toughness; at other times, they may act negatively like decreasing the elastic modulus or ultimate tensile strength (these negative effects have been noted to occur with increasing capsule concentration of large capsules) [49]. Key advantages to the inclusion of microcapsules or tubes that contain healing agents are the ability to close a cut with minimal material; the fibers can perform at the same level even after repeated usage thanks to the constrained recovery resulting in renewed tension programming. By using stress recovery, it is possible to force the closure of a crack or cut within the matrix [50]. Microcapsules are preferred for short-term corrosion protection. When damage occurs, the microcapsule breaks down, which allows for the healing agent to react with the metal substrate to form a passivating conversion layer; this provides time for healing to take place and prevents further corrosion. This basically means that healing is a two-step process in which the microcapsules disperse to form a passivating layer that improves the adhesion strength and corrosion resistance of the substrate, and from there, the matrix may then be heated to initiate the shape memory effect to close the damaged area [51]. Encapsulating a catalyst, where there exists an initiator pellet and a resin pellet, can act to induce self-healing in a polymer composite; this has been tested in polydimethylsiloxane successfully. Hollow glass fibers made up of borosilicate can act as capsules for the containment of liquid healing agents, are capable of restoring up to 97% of the original flexural strength, are more capable per volume of storing healing agents, and could be used as a means of visual detection for damage, but such fibers are limited in that they must first be broken in order to distribute the agents, and the fibers could possibly expand under heat which may lead to damage of the matrix [52].

Another suggested anticorrosion coating material would be high-aspect ratio fillers, like clay additives. One specific clay of interest would be montmorillonite clay, a sodium clay that has been organically modified resulting in better compatibility and higher reinforcement to polymer matrices; it has a 2D crystal structure hydrated with an alumina octahedral sheet in between two silica tetrahedral sheets; these stacking layers result in van der Waals gaps [53].

Montmorillonite clay (shown in Figure 16) is positively charged, which, when added to a polymer coating, compensates for the excess negative charge by adsorbing alkali metal ions onto the clay platelets which creates a hydrophilic form of clay that has stable suspensions in water. At a certain point of concentration, these clay suspensions form a highly viscous gel in water where the volume filling is jammed or has a percolated network of clay particles that can be observed by the pseudosolid behavior the gel exhibits; it is worth noting that polymer-clay nanocomposites are also capable of exhibiting gelation after a critical concentration of clay has been achieved. When added to the polymer coating, montmorillonite clay must be made more organophilic through the replacement of alkali metals with cationic surfactants typically of primary, secondary, tertiary, and quaternary alkylammonium ions as reinforcing nonpolar polymers necessitates the addition of compatibilizers. Mechanical, physical, and thermal properties of polymer-clay nanocomposites are capable of being improved through the dispersion and exfoliation of the clay platelets throughout the matrix [54]. Specifically, the fillers allow for the polymer to achieve a higher modulus, an increase in thermal stability and conductivity, better solvent resistance and ionic conductivity, and improved self-passivation and barrier properties [53]. Inclusion of clay into the polymer matrix appears to have a bell curve in effectiveness, as the corrosion current density for a polymer of 1 wt% of clay is an order of magnitude lower than that for a polymer without clay, but it reaches the same value as the wt% of clay reaches 10%. Coatings with low values (between 0 and 2 wt% clay) demonstrate an increase in impedance in comparison to the plain polymer coating, but it drops significantly as the weight percent of clay reaches 2 wt% or greater, due to clay aggregating and agglomerating within the matrix [54]. Additionally, the inclusion of clay in the polymer improves the rate of polymerization as well as the degree of polymerization, while also improving the processability as the condensation polymerization reduces the reaction solution viscosity [53]. Polymer chain movement gets impeded by the clay within the matrix, and the clay also imbues lower porosity and greater stiffness as the polymer chains are physically entangled [54]. The performance of polymer composites depends upon the filler dispersed throughout the matrix; as such, one of the main focuses when it comes to adding fillers is the dispersion of the material in a manner that prevents agglomeration [53].

6. Designs

Shape memory effects may help self-healing via pulling crack surfaces closer together; this may be achieved by embedding or combining a shape memory system into the polymer. An example would be wires encased in a polymer, where if a crack forms in the polymer, the shape memory effect produced by the wire forces the crack to close, and capsules located throughout the polymer may

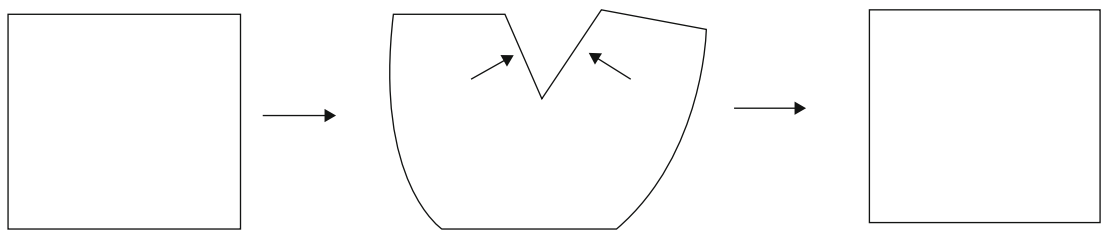

Figure 17: When a crack or similar damage occurs to a shape memory polymer capable of self-healing through physical means, if the polymer can be made to physically close the crack by means of a wire or the surface bending the polymer shut, and heat is applied, the polymer can then self-heal and repair the damage, resuming its former shape with minimal loss of properties.

then release the polymeric self-healing chemicals to seal the crack, so long as the crack is in an area where the wire can exert the shape memory effect [55]; an example is shown in Figure 17.

Self-healing is generally induced by heat, meaning that a frictional process that can generate sufficient heat to bring the polymer to a viscoelastic melt state would enable the polymer to rebond and repair. Heating-induced healing of thermosets relies upon the crosslinking of unreacted polymer groups, where heating is applied until the molecules within can interdiffuse with each other and thereby allow for any residual groups to react. Requirements for thermoset healing agents are that they should be reversibly bonded to the crosslinked network while below the healing temperature (to minimize the effects they may have upon the mechanical properties), but once above the healing temperature, they become mobile to enable diffusion across the crack, and the addition of linear chain molecules will not interfere with the mechanical properties of the matrix. If cracks and loss of strength are the result of broken molecules or other changes at the atomic level, then repair must occur through the reaction to recombine said molecules, or in other words, an inverse reaction must occur. Deterioration of the polymer is minimized if the recovery rate occurs at the same pace as deterioration, but high temperatures are required for self-healing to occur by reversible chemical interactions. In applying self-healing by external means, it is not the matrix that acts to heal itself but the encapsulated healing agents, which are stored in the form of either a "pipeline" or a microcapsule that is destroyed, and said agents are released to heal the crack [31]. It should be noted that if temperatures exceed what the polymer is capable of healing, it will cause the polymer to deteriorate and no longer function properly. Additionally, a defect in a polymer coating that would allow corrosion to occur at the metal underneath can result in loss of coating adhesion and a reduction in the integrity of the metal. Self-healing by the chemical reaction process is susceptible to side reactions that may reduce healing or shape memory properties. Physiochemical mechanisms in shape memory polymers can reverse mechanical deformation that was induced by stress or strain by several methods, the most popular and easiest being heating the material, without the need for a chemical reaction to take place. This process takes advantage of the multiple glass transition temperatures (T_g) or melting temperatures (T_m) found within the polymer, as the polymer partially melts and can solidify later, but a different part of the block keeps a solid form, enabling both strain recovery and shape retention [19].

As mentioned previously, transformations are induced in a shape memory alloy through heating; this is a cause for concern for the application of shape memory polymers as a means of corrosion protection as they may have differing temperatures to induce transformation. This concern may be alleviated by the limitation that most current shape memory alloys have transition temperatures below 100°C; thus, it is possible for polymers to act as a means of corrosion inhibition [11]. For instance, most DA adducts form at temperatures of around or below 90°C and dissociate at temperatures ranging from 110 to 130°C. The healing process of DA copolymers that contain furan/maleimide occurs at a temperature range of 120 to 150°C as this triggers partial debonding and therefore enhances molecular mobility [39]. Therefore, it is possible for polymers to match the range of temperatures of shape memory alloys and induce healing within that range; the problem then is fine-tuning to match the temperatures that the shape memory effect takes place for both the polymer and the alloy. There are several methods by which to induce this process, one of the easiest being blending polymers as, generally, increasing the T_g of a polymer blend follows the increase in the concentration of the higher-T_g copolymer [38]. Alternatively, the inclusion of spacers into a polymer can affect the T_g as, for example, a polycaprolactone-based polymer material has a melting temperature or T_m of 51.7°C, but the addition of spacers reduces it to 49.6°C. Additionally, the spacer units can act to delay the recrystallization of the polymer or enhance crystallization if in the presence of polymers capable of forming hydrogen-bonded crystalline segments, such as polyurea [19]. Other materials, like carbon nanotubes or graphene nanofillers, can also influence the T_g of a polymer blend as, for example, the addition of 1 wt% graphene to an epoxy ester-siloxane-urea polymer blend can increase the T_g from 95 to 115°C, as shown in the graph in Figures 18(a)–18(c) [17].

When the maxima of the loss tangent, tan δ, occur for the α transition across a range of temperatures, it can be considered the T_g of the polymeric material, as it relates to the thermal energy needed for changes to occur with the molecules at the microscopic level [56]. Therefore, the addition of graphene may increase the T_g of the material, but it is not entirely straightforward as it appears that the wt% added can affect polymers differently, as may be shown in the

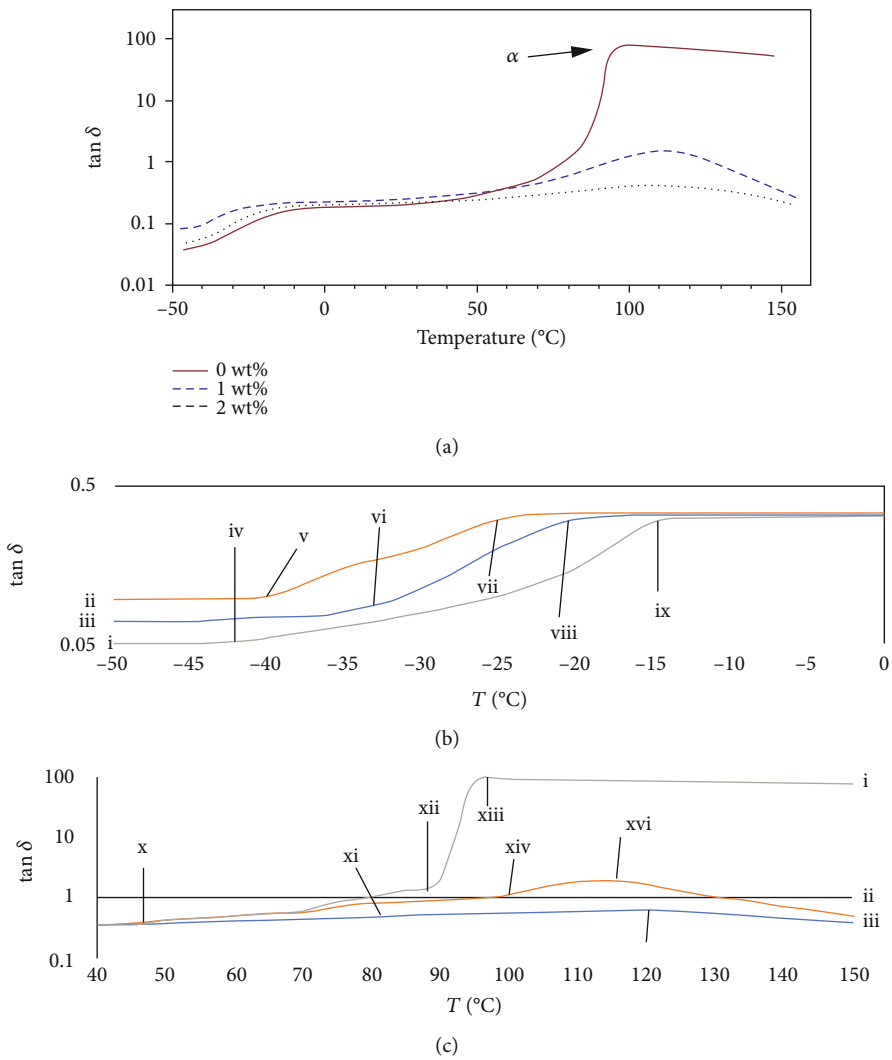

Figure 18: (a) The effect the introduction of graphene has upon an epoxy ester-siloxane-urea polymer system. (b) A closer view of the first T_g curve. (c) A closer view of the second T_g curve. For (b) and (c), (i) is 0 wt% graphene added to the polymer system, (ii) is the effect when 1 wt% graphene is added to the polymer system, and (iii) is the effect of 2 wt% graphene being added to the polymer system. (iv), (x), and (xii) are possible T_g points for the polymer system with no graphene added. (x), (v), and (xiv) are possible T_g points for the polymer system with 1 wt% graphene added. (x) and (vi) are possible T_g points for the polymer system with 2 wt% graphene added. (ix) and (xii) are local tan δ maxima for the polymer system with no graphene added. (vi) and (xvi) are local tan δ maxima for the polymer system with 1 wt% graphene added. (viii) and (xv) are local tan δ maxima for the polymer system with 2 wt% graphene added [17].

graphs above. There are major tan δ maxima shown; graph (c) shows the secondary tan δ maxima and is the one of primary consideration and is relatively straightforward in that an increase in wt% graphene from 0 to 2 wt% results in an increase of T_g from 95 to around 120°C. In contrast, graph (b) shows the first tan δ maxima, where it appears that the addition of graphene overall works to also lower the T_g, demonstrated by both 1 and 2 wt% having a lower T_g value; it is also worth noting that increasing the wt% brings the T_g closer to that of the neat polymer [17]; this can be more easily shown in Table 4.

Markets are pushing towards developing high-temperature shape memory alloys capable of transformation temperatures much higher than 100°C. However, any attempts at forming stable materials higher than 100°C are frustrated by the issue that exposure to large amounts of thermal energy affects the rate-dependent processes that occur within the material and therefore affects the microstructural stability, its resistance to deformation, the recovery, and the environmental resistance [11]. Matching the developments has been the development of high-temperature shape memory polymers; one such example would be that of a self-healing high-temperature polyimide which has an operational temperature of 243°C if polystyrene is incorporated into the polymer [37].

Naturally, there are more novel approaches being developed that could further improve the possible applications for shape memory polymers. It is worth noting that in environments where the material may experience low-temperature conditions, self-healing may not occur or be inadequate

Table 4: tan δ peak temperature [17].

wt%	0 wt%	1 wt%	2 wt%
Temperature where tan δ initiates change for graph (b) in ˚C	-45	-40	-35
Temperature where tan δ reaches the peak for graph (b) in ˚C	-15	-25	-20
Temperature where tan δ initiates change for graph (c) in ˚C	45	45	45
Temperature where tan δ initiates second change for graph (c) in ˚C	90	100	80
Temperature where tan δ reaches the peak for graph (c) in ˚C	95	115	120

towards the damage received; thus, in such environments where it may be applied, it would necessitate the use of agents capable of self-heating the material to achieve the desired effects. Therefore, another means of initiating self-healing must be devised; an easy method to accomplish this is with infrared radiation, microwave radiation, or other forms of radiation, depending upon the material chosen, though this may even occur at room temperature [52]. Beneficially, using microwave or infrared radiation to activate the self-healing mechanism can be done remotely and over only a specific area without affecting the surrounding surface, acting almost instantaneously, from the second the light is turned on to the moment it is turned off [57]. Though not quite related to shape memory alloys, microwave or infrared radiation can also serve as a trigger mechanism for shape memory polymer recovery behavior, and because they are energy-efficient, low cost, and quick to trigger recovery behavior, they have immense appeal for other shape memory applications [58]. Shape memory polymers that use infrared or microwave radiation as a means of activation generally include photosensitive fillers, like metal nanoparticles or conjugated polymers, and conductive fillers like graphene or carbon nanotubes into thermally activated shape memory polymers to induce the desired recovery behaviors from the material [2, 52, 57, 58]. For example, multiwalled carbon nanotubes were distributed in a polyurethane matrix which resulted in improving the maximum stretch stress by 120%, the recovery force by 100%, the tensile strength by 24%, and the loss modulus by a third in comparison to plain polyurethane; additionally, it enabled microwaves to activate the shape memory effect in polyurethane [2]. These polymers that activate their self-healing mechanisms via microwave or infrared radiation have uses such as surface coatings, electronic devices, or other biological uses and are particularly noteworthy for potential uses in aerospace applications [2, 52]. Another factor of consideration would be the toughness of typical self-healing polymers, which are worse than covalent polymer networks because they can reversibly form bonds or, in other words, break and reform their polymer networks to achieve their healing ability. If a permanent, covalent network could be introduced to a reversible network, then the mechanical properties could be improved. Typically, doing so forms a hydrogel, but they contain an immense amount of water within that makes them unsuitable as a coating material as they can leach or corrode the material and affect its overall properties. Reversible crosslinking between the covalent and reversible polymer networks is difficult, as the crosslinked materials are immiscible and would normally require cosolvents to mix; attempting to form a "dry" polymer network often results in viscoelastic phase separation. One notable attempt at forming a "dry" network is a fabrication of randomly branched crosslinked polymers capable of supporting reversible hydrogen bonding in addition to permanent covalent crosslinks, which forces mixing at the molecular level without viscoelastic phase separation or the need for cosolvents. This was formed from a combination of diamines and acrylic acid that form a supramolecular network with either amide-amide connections or amide-carboxyl connections. Small deformations of the hybrid elastomer material only result in the breakage and reformation of hydrogen bonds, and larger deformations result in macrocrazing on a scale of 1 to 1000 μm that preserves the material's integrity and has a fracture energy of 13,500 J/m^2, which is comparable to natural rubber. Self-healing can occur at room temperature and, post-recovery, can have a tensile strength comparable to most other elastomers at 4 MPa. Unfortunately, applications that may consider corrosion inhibition for shape memory materials would be limited as the polymer network has a T_g of 4-14°C and acts as a rubbery elastomer at room temperature and thus would require the modification and the sacrifice of some of its properties to act as a coating [59].

Another development for shape memory composites would be triple-shape memory composites. These polymer composites can change into two other temporary shapes prior to recovering into the primary, permanent shape when their recovery behavior is triggered, thus performing complex recovery motions much better than more traditional shape memory composites. These transition stages can be accomplished through either a series of temperatures in which it will switch forms or a singular temperature value in which the changes shall occur [60]. The step transition behavior within the polymer is what affects the number of temporary positions that the polymer may assume within its shape memory cycle, meaning that the number of transition temperatures within a polymer blend affects the number of shapes it can assume and therefore implies that quadruple-shape or greater shape memory composites could be feasible. The basic approach to accomplishing this is through a polymer with a singular, broad phase of polymer chain transition as the increase of monomer diversity requires even more precise synthesis of the desired polymer material [42]. By combining the shape memory alloys and shape memory polymers to form a shape memory composite, one can form a shape memory composite with three-way motions by 3D printing a shape memory polymer around a shape memory alloy [3]. Notably though, studies about the material indicate that deformation is generally restricted to a range around the linear elastic region and that the stiffness above the transition temperatures is low enough to promote creep under external

loading; also, for certain triple-shape memory polymers, thermal expansion of the composite leads into far higher values of deformation than normal at high temperatures. Developments in correcting the issues of triple-shape memory polymer composites focus on the polymers used in producing the materials, as most triple-shape memory composites are created via polymer blending. Polymer blending is the most critical step as the goal is to create a composite from polymers that are thermally miscible with each other; otherwise, weak or separated interfaces form at the boundaries, thereby weakening the overall properties of the potential composite, and given that, unfortunately, most resins and plastics are incapable of blending with each other thermally, a necessary factor in the development of better triple-shape memory polymer composites will be determining the materials capable of blending with each other effectively [60].

7. Conclusion

Polymers present a potential opportunity in corrosion inhibition, as they are capable of matching or surpassing the more traditional method of including elements such as the hazardous chromium to inhibit corrosion. But as polymers are inherently inert to the environment, they risk a gradual loss of functionality due to microcracking, and therefore, it is desirable to use polymers capable of self-healing such as a polyimide-b-polyurea blend. Additionally, self-healing polymers may be enhanced further by means of nanomaterials or other filler materials, as they can improve the conductivity of the polymer blend or work to improve the response times of shape memory polymers. Future developments regarding shape memory polymers will likely focus on tailoring the polymer blend towards a preferred goal through the addition of certain fillers, such as microcapsules, or selectively initiating the self-healing process or shape memory effect, such as the application of infrared or microwave radiation across a specific area through the inclusion of, for example, carbon nanotubes. These developments should allow for a coating tailored to possible aerospace, particularly deployable structures, or robotics and other applications, such as actuators. In general, areas where a shape memory polymer alone would have insufficient strength or other material properties that a shape memory alloy has while maintaining a cheaper and less toxic corrosion-preventative coating would make the most effective use for a shape memory polymer coating.

Data Availability

The data supporting this Literature Review are available from their corresponding author cited from the journals fond in the references section of the review. They are cited at relevant places within the text as references [1–60]. For the figures and tables, the references may be found within the table or below the figure in the text describing the figure. Figures 2, 11, 15, 16, and 18 are used with the permission of the Author.

Conflicts of Interest

The authors declare no conflict of interest that would influence the paper.

References

[1] F. F. Li, Y. J. Liu, and J. S. Leng, "Progress of shape memory polymers and their composites in aerospace applications," *Smart Materials and Structures*, vol. 28, no. 10, article 103003, 2019.

[2] K. K. Patel and R. Purohit, "Improved shape memory and mechanical properties of microwave-induced shape memory polymer/MWCNTs composites," *Materials today communications*, vol. 20, article 100579, 2019.

[3] R. Matsui, K. Takeda, H. Tobushi, and E. A. Pieczyska, "Mechanical properties and advanced subjects in shape memory alloys and polymers," *Journal of theoretical and applied mechanics (Poland)*, vol. 56, no. 2, pp. 447–456, 2018.

[4] H. Luo, Z. Li, G. Yi et al., "Multi-stimuli responsive carbon nanotube-shape memory polymeric composites," *Materials Letters*, vol. 137, pp. 385–388, 2014.

[5] M. Lei, Z. Chen, H. Lu, and K. Yu, "Recent progress in shape memory polymer composites: methods, properties, applications and prospects," *Nanotechnology reviews*, vol. 8, no. 1, pp. 327–351, 2019.

[6] Z. G. Wei, R. Sandstrom, and S. Miyazaki, "Shape memory materials and hybrid composites for smart systems: part II shape-memory hybrid composites," *Journal of Materials Science*, vol. 33, no. 15, article 230586, pp. 3763–3783, 1998.

[7] Y. Liu, Z. Dong, L. Yu, Y. Liu, and H. Li, "Influence of aging on shape memory effect and corrosion resistance of a new Fe–Mn–Si-based alloy," *Journal of materials research*, vol. 30, no. 2, pp. 179–185, 2015.

[8] G. A. López, M. Barrado, E. H. Bocanegra, J. M. San Juan, and M. L. Nó, "Influence of the matrix and of the thermal treatment on the martensitic transformation in metal matrix composites," *Materials science & engineering A*, vol. 481-482, no. 1-2 C, pp. 546–550, 2008.

[9] H. Farhat, R. Griffin, I. N. A. Oguocha, and R. Evitts, "An investigation of the corrosion behaviour of a FeNiCoAlTa shape memory alloy in 3.5 wt-% NaCl solution," *Corrosion engineering, science and technology*, vol. 53, no. 8, pp. 611–616, 2018.

[10] A. O. Moghaddam, M. Ketabchi, and R. Bahrami, "Kinetic grain growth, shape memory and corrosion behavior of two Cu-based shape memory alloys after thermomechanical treatment," *Transactions of nonferrous metals society of China*, vol. 23, no. 10, pp. 2896–2904, 2013.

[11] P. Nnamchi, A. Younes, and S. González, "A review on shape memory metallic alloys and their critical stress for twinning," *Intermetallics*, vol. 105, pp. 61–78, 2019.

[12] E. Kassab, L. Neelakantan, M. Frotscher et al., "Effect of ternary element addition on the corrosion behaviour of NiTi shape memory alloys," *Materials and Corrosion*, vol. 65, no. 1, pp. 18–22, 2014.

[13] G. Rondelli and B. Vicentini, "Effect of copper on the localized corrosion resistance of Ni-Ti shape memory alloy," *Biomaterials*, vol. 23, no. 3, pp. 639–644, 2002.

[14] S. N. Saud, E. Hamzah, T. Abubakar, and H. R. Bakhsheshi-Rad, "Correlation of microstructural and corrosion characteristics of quaternary shape memory alloys Cu-Al-Ni-X (X=Mn

or Ti)," *Transactions of Nonferrous Metals Society of China*, vol. 25, no. 4, pp. 1158–1170, 2015.

[15] M. Zare and M. Ketabchi, "Effect of chromium element on transformation, mechanical and corrosion behavior of thermomechanically induced Cu–Al–Ni shape-memory alloys," *Journal of Thermal Analysis and Calorimetry*, vol. 127, no. 3, pp. 2113–2123, 2016.

[16] N. D. Alqarni, J. Wysocka, N. El-Bagoury, J. Ryl, M. A. Amin, and R. Boukherroub, "Effect of cobalt addition on the corrosion behavior of near equiatomic NiTi shape memory alloy in normal saline solution: electrochemical and XPS studies," *RSC Advances*, vol. 8, no. 34, pp. 19289–19300, 2018.

[17] P. A. Okafor, J. Singh-Beemat, and J. O. Iroh, "Thermomechanical and corrosion inhibition properties of graphene/epoxy ester- siloxane-urea hybrid polymer nanocomposites," *Progress in Organic Coatings*, vol. 88, pp. 237–244, 2015.

[18] M. K. Ibrahim, E. Hamzah, S. N. Saud, E. M. Nazim, N. Iqbal, and A. Bahador, "Effect of Sn additions on the microstructure, mechanical properties, corrosion and bioactivity behaviour of biomedical Ti–Ta shape memory alloys," *Journal of Thermal Analysis and Calorimetry*, vol. 131, no. 2, article 6636, pp. 1165–1175, 2017.

[19] A. Lutz, O. van den Berg, J. van Damme et al., "A shape-recovery polymer coating for the corrosion protection of metallic surfaces," *ACS applied materials & interfaces*, vol. 7, no. 1, pp. 175–183, 2015.

[20] M. Sun, Z. Ma, A. Li, G. Zhu, and Y. Zhang, "Anticorrosive performance of polyaniline/waterborne epoxy/poly(methylhydrosiloxane) composite coatings," *Progress in Organic Coatings*, vol. 139, article 105462, 2020.

[21] H. Lu, K. Yu, S. Sun, Y. Liu, and J. Leng, "Mechanical and shape-memory behavior of shape-memory polymer composites with hybrid fillers," *Polymer International*, vol. 59, no. 6, pp. 766–771, 2010.

[22] Z. M. Blednova, N. A. Makhutov, P. O. Rusinov, and M. A. Stepanenko, "Mechanical and tribological properties of "substrate–material" multifunctional composite with shape memory effect," *Inorganic materials*, vol. 52, no. 15, pp. 1489–1497, 2016.

[23] D. Zhang, L. Wang, H. Qian, and X. Li, "Superhydrophobic surfaces for corrosion protection: a review of recent progresses and future directions," *Journal of Coatings Technology and Research*, vol. 13, no. 1, article 9744, pp. 11–29, 2016.

[24] H. Qian, D. Xu, C. du et al., "Dual-action smart coatings with a self-healing superhydrophobic surface and anticorrosion properties," *Journal of materials chemistry. A, Materials for energy and sustainability*, vol. 5, no. 5, pp. 2355–2364, 2017.

[25] L. Feng and J. O. Iroh, "Corrosion resistance and lifetime of polyimide-*b*-polyurea novel copolymer coatings," *Progress in Organic Coatings*, vol. 77, no. 3, pp. 590–599, 2014.

[26] Z. Pan, R. Huang, and Z. Liu, "Prediction of the thermomechanical behavior of particle reinforced shape memory polymers," *Polymer Composites*, vol. 40, no. 1, pp. 353–363, 2017.

[27] A. Alipour, M. Kadkhodaei, and A. Ghaei, "Finite element simulation of shape memory alloy wires using a user material subroutine: parametric study on heating rate, conductivity, and heat convection," *Journal of Intelligent Material Systems and Structures*, vol. 26, no. 5, pp. 554–572, 2014.

[28] N. Zheng, Y. Xu, Q. Zhao, and T. Xie, "Dynamic covalent polymer networks: a molecular platform for designing functions beyond chemical recycling and self-healing," *Chemical Reviews*, vol. 121, no. 3, pp. 1716–1745, 2021.

[29] K. Neuking, A. Abu-Zarifa, S. Youcheu-Kemtchou, and G. Eggeler, "Polymer/NiTi-composites: fundamental aspects, processing and properties," *Advanced Engineering Materials*, vol. 7, no. 11, pp. 1014–1023, 2005.

[30] F. García and M. M. J. Smulders, "Dynamic covalent polymers," *Journal of polymer science. Part A, Polymer chemistry*, vol. 54, no. 22, pp. 3551–3577, 2016.

[31] Y. C. Yuan, T. Yin, M. Z. Rong, and M. Q. Zhang, "Self healing in polymers and polymer composites. Concepts, realization and outlook: a review," *Express polymer letters*, vol. 2, no. 4, pp. 238–250, 2008.

[32] F. Herbst, D. Döhler, P. Michael, and W. H. Binder, "Self-healing polymers via supramolecular forces," *Macromolecular Rapid Communications*, vol. 34, no. 3, pp. 203–220, 2013.

[33] S. R. Kunst, H. R. P. Cardoso, C. T. Oliveira et al., "Corrosion resistance of siloxane-poly(methyl methacrylate) hybrid films modified with acetic acid on tin plate substrates: influence of tetraethoxysilane addition," *Applied Surface Science*, vol. 298, pp. 1–11, 2014.

[34] L. Feng and J. O. Iroh, "Polyimide-b-polysiloxane copolymers: synthesis and properties," *Journal of Inorganic and Organometallic Polymers and Materials*, vol. 23, no. 3, article 9795, pp. 477–488, 2013.

[35] L. Cai, T. E. Kodger, R. E. Guerra, A. F. Pegoraro, M. Rubinstein, and D. A. Weitz, "Soft poly(dimethylsiloxane) elastomers from architecture-driven entanglement free design," *Advanced materials (Weinheim)*, vol. 27, no. 35, pp. 5132–5140, 2015.

[36] J. Singh-Beemat and J. O. Iroh, "The effect of morphology on the corrosion inhibition and mechanical properties of hybrid polymer coatings," *Journal of applied polymer science*, vol. 128, no. 3, pp. 1616–1624, 2013.

[37] D. Kong, J. Li, A. Guo, X. Zhang, and X. Xiao, "Self-healing high temperature shape memory polymer," *European Polymer Journal*, vol. 120, article 109279, 2019.

[38] L. Feng and J. O. Iroh, "Novel polyimide- *b* -polyurea supramacromolecule with remarkable thermomechanical and dielectric properties," *European Polymer Journal*, vol. 49, no. 7, pp. 1811–1822, 2013.

[39] L. T. Nguyen, H. Q. Pham, D. T. Thi Phung et al., "Macromolecular design of a reversibly crosslinked shape-memory material with thermo-healability," *Polymer*, vol. 188, article 122144, 2020.

[40] S. Schäfer and G. Kickelbick, "Self-healing polymer nanocomposites based on Diels-Alder-reactions with silica nanoparticles: the role of the polymer matrix," *Polymer*, vol. 69, pp. 357–368, 2015.

[41] J. Longun, G. Walker, and J. O. Iroh, "Surface and mechanical properties of graphene-clay/polyimide composites and thin films," *Carbon (New York)*, vol. 63, pp. 9–22, 2013.

[42] Y. Xia, Y. He, F. Zhang, Y. Liu, and J. Leng, "A review of shape memory polymers and composites: mechanisms, materials, and applications," *Advanced materials (Weinheim)*, vol. 33, no. 6, article 2000713, 2021.

[43] A. Lazauskas, D. Jucius, V. Baltrušaitis et al., "Shape-memory assisted scratch-healing of transparent thiolene coatings," *Materials*, vol. 12, no. 3, p. 482, 2019.

[44] Y. Huang, L. Deng, P. Ju et al., "Triple-action self-healing protective coatings based on shape memory polymers containing

dual-function microspheres," *ACS Applied Materials & Interfaces*, vol. 10, no. 27, pp. 23369–23379, 2018.

[45] S. E. Galyon Dorman, T. A. Reid, B. K. Hoff, D. H. Henning, and S. E. Collins, "The effect of corrosion inhibitors on environmental fatigue crack growth in Al-Zn-Mg-Cu," *Engineering Fracture Mechanics*, vol. 137, pp. 56–63, 2015.

[46] M. Kopeć, K. Szczepanowicz, G. Mordarski et al., "Self-healing epoxy coatings loaded with inhibitor-containing polyelectrolyte nanocapsules," *Progress in Organic Coatings*, vol. 84, pp. 97–106, 2015.

[47] K. Cao, Z. Yu, and D. Yin, "Preparation of Ce-MOF@TEOS to enhance the anti-corrosion properties of epoxy coatings," *Progress in Organic Coatings*, vol. 135, pp. 613–621, 2019.

[48] F. Ubaid, A. B. Radwan, N. Naeem et al., "Multifunctional self-healing polymeric nanocomposite coatings for corrosion inhibition of steel," *Surface & Coatings Technology*, vol. 372, pp. 121–133, 2019.

[49] B. J. Blaiszik, N. R. Sottos, and S. R. White, "Nanocapsules for self-healing materials," *Composites Science and Technology*, vol. 68, no. 3-4, pp. 978–986, 2008.

[50] A. Shojaei, G. Li, and G. Z. Voyiadjis, "Cyclic viscoplastic-viscodamage analysis of shape memory polymers fibers with application to self-healing smart materials," *Journal of applied mechanics, transactions ASME*, vol. 80, no. 1, pp. 11014-11015, 2013.

[51] W. Fan, W. Li, Y. Zhang et al., "Cooperative self-healing performance of shape memory polyurethane and alodine-containing microcapsules," *RSC Advances*, vol. 7, no. 74, pp. 46778–46787, 2017.

[52] N. J. Kanu, E. Gupta, U. K. Vates, and G. K. Singh, "Self-healing composites: a state-of-the-art review," *Composites Part A Applied Science and Manufacturing*, vol. 121, pp. 474–486, 2019.

[53] J. Wang, J. O. Iroh, and A. Long, "Controlling the structure and rheology of polyimide/nanoclay composites by condensation polymerization," *Journal of Applied Polymer Science*, vol. 125, no. S1, pp. E486–E494, 2012.

[54] J. Singh-Beemat, J. O. Iroh, and L. Feng, "Mechanism of corrosion protection of aluminum alloy substrate by hybrid polymer nanocomposite coatings," *Progress in Organic Coatings*, vol. 76, no. 11, pp. 1576–1580, 2013.

[55] M. D. Hager, S. Bode, C. Weber, and U. S. Schubert, "Shape memory polymers: past, present and future developments," *Progress in Polymer Science*, vol. 49-50, pp. 3–33, 2015.

[56] W. F. Marashdeh, J. Longun, and J. O. Iroh, "Relaxation behavior and activation energy of relaxation for polyimide and polyimide–graphene nanocomposite," *Journal of applied polymer science*, vol. 133, no. 28, article 43684, 2016.

[57] H. du, X. Liu, Y. Yu, Y. Xu, Y. Wang, and Z. Liang, "Microwave-induced poly(ionic liquid)/poly(vinyl alcohol) shape memory composites," *Macromolecular chemistry and physics*, vol. 217, no. 23, pp. 2626–2634, 2016.

[58] Y. Bai, J. Zhang, D. Wen et al., "A reconfigurable, self-healing and near infrared light responsive thermoset shape memory polymer," *Composites Science and Technology*, vol. 187, article 107940, 2020.

[59] J. Wu, L. Cai, and D. A. Weitz, "Tough self-healing elastomers by molecular enforced integration of covalent and reversible networks," *Advanced materials (Weinheim)*, vol. 29, no. 38, article 1702616, 2017.

[60] X. Wu, C. fu, Z. Tan et al., "Tunable triple-shape memory composite fabricated by selective crosslinking of polycaprolactone/poly(butylene adipate-co-terephthalate)/bentonite," *Journal of applied polymer science*, vol. 137, no. 16, p. 48577, 2020.

Hindawi
International Journal of Polymer Science
Volume 2021, Article ID 5561755, 7 pages
https://doi.org/10.1155/2021/5561755

Research Article

Sugarcane Bagasse-Derived Activated Carbon- (AC-) Epoxy Vitrimer Biocomposite: Thermomechanical and Self-Healing Performance

Balaji Krishnakumar,[1] Debajyoti Bose,[2] Manjeet Singh,[1,3] R. V. Siva Prasanna Sanka,[4] Velidi V. S. S. Gurunadh,[1] Shailey Singhal,[1] Vijay Parthasarthy,[1] Liberata Guadagno,[5] Poornima Vijayan P,[6] Sabu Thomas,[7,8,9] and Sravendra Rana[1]

[1]*University of Petroleum & Energy Studies (UPES), School of Engineering, Energy Acres, Bidholi, Dehradun 248007, India*
[2]*Faculty of Applied Sciences & Biotechnology, Shoolini University of Biotechnology & Management Sciences, Solan 173229, Himachal Pradesh, India*
[3]*Department of Chemistry, School of Physical Sciences, Mizoram University, Aizawl, 796004, Mizoram, India*
[4]*Department of Mechanical Engineering, University Institute of Engineering, Chandigarh University, Gharuan, Punjab 140413, India*
[5]*Department of Industrial Engineering, University of Salerno, Via Giovanni Paolo II, 132, 84084 Fisciano, Italy*
[6]*Sree Narayana College for Women (Affiliated to University of Kerala), 691001, Kollam, Kerala, India*
[7]*International and Inter University Centre for Nanoscience and Nanotechnology, Mahatma Gandhi University, Kottayam, Kerala, India*
[8]*School of Chemical Sciences, Mahatma Gandhi University, Kottayam, Kerala, India*
[9]*School of Energy Materials, Mahatma Gandhi University, Kottayam, Kerala, India*

Correspondence should be addressed to Liberata Guadagno; lguadagno@unisa.it and Sravendra Rana; srana@ddn.upes.ac.in

Received 21 January 2021; Revised 25 March 2021; Accepted 2 June 2021; Published 15 June 2021

Academic Editor: Peng He

Vitrimeric materials have emerged as fascinating and sustainable materials owing to their malleability, reprocessability, and recyclability. Sustainable vitrimeric materials can be prepared by reinforcing polymeric matrix with bioderived fillers. In the current work, a sustainable vitrimer is prepared by incorporating biomass-derived activated carbon (AC) filler into the epoxy matrix to achieve enhanced thermal and mechanical properties. Thus, prepared biocomposite vitrimers demonstrate a lower-temperature self-healing (70°C for 5 min) via disulfide exchanges, compared to the pristine epoxy vitrimers (80°C for 5 min). Significantly, the self-healing performances have been studied extensively with the flexural studies; and changes in material healing efficiency have been demonstrated based on the observed changes in modulus.

1. Introduction

Conventional thermosetting polymers have been applied in various fields like automobile, construction, aviation, wind turbines, and coatings [1]. The last decade has witnessed exciting progress concerning the design and development of structural polymeric materials, necessary to keep up with the challenging tasks that scientists all over the world have to face for the future. Although many thermosetting composites have been effectively designed to ensure good mechanical performance and self-responsive ability [2–5], the usage of thermoset material is restricted due to their poor reusability and reprocessability. This is due to their extremely high crosslink density, which restricts chain exchanges and therefore decreases malleable nature. On account of this, adequate research on malleable thermoset materials has been carried

out in the last few years [6]. Previously reported reprocessable thermosets *via* Diels-Alder chemistry have demonstrated (dissociative covalent adaptive network) their exchanges in a disruptive way, wherein network crosslink density has changed abruptly [7]. In 2011, Montarnal and coworkers [8] introduced reprocessable thermoset "vitrimer," which extended the existing classification, as well as entailed fixed crosslink density via exchangeable covalent adaptive network formations. Owing to fixed network integrity, vitrimer materials behave like a silica glass former. Depending on the temperature range, they can also manifest the behavior of a viscoelastic fluid. They are characterized by a special viscoelasticity regime, which denotes a topology freezing-point temperature (T_v), which can be situated below or above the glass transition temperature (T_g). Also, the established T_v has been extrapolated through Arrhenius and Maxwell equations; hence, it was measured after viscosity reaches 10^{12} Pa·s [8].

Moreover, many thermoset vitrimers have been introduced with different chemistries like transesterification [9], transcarbomylation [10], transamination [11], disulfide linkages [12], and imine exchanges [6]. Transesterification-based vitrimer system has been majorly discussed (with or without catalyst), due to their simple preparation and effective covalent exchange mechanism [13–15]. The reported malleable thermoset vitrimers are all recyclable/reprocessable, and some of them have exhibited self-healing performances. Vitrimers having intrinsic self-healing are more attractive than those based on extrinsic self-healing mechanisms in which the healing can be activated via covalent network exchanges [16]. In particular, low-temperature self-healing demonstrated disulfide exchange-assisted vitrimer materials which have been reported adequately, to acquire the processable vitrimer system with intrinsic self-healing properties [17, 18]. Further, the different chemistry involvement encourages the vitrimer material with prevailed properties for a real-time application (such as soft electronics, 3D printing, and adhesives) [19, 20].

Since the development of vitrimer studies, various kinds of fillers have been incorporated in epoxy/vitrimeric matrices, where better thermal and mechanical properties were achieved with effect of nanofiller addition. In particular, the addition of carbon allotrope-based fillers in a vitrimeric system resulted in prominent mechanical and self-healing properties [21]. In recent times, bioderived monomers have been included in vitrimer studies to prepare sustainable vitrimer materials [15, 22–24], where like sustainable bio-based polymers have gained huge interest to aspire the green environment [25]. Bio-based vitrimers have been developed from different derivatives like lignin, fructose, and soybean oil [26]. However, their thermal and mechanical performances were found to be comparatively lower than the synthetically prepared vitrimeric materials. To overcome these weaknesses, the addition of fillers into the matrix has been realized and exhibited notable sustainability and improved thermal/-mechanical properties. Recently, bio-based epoxy/cashew nutshell liquid vitrimer was demonstrated with CNTs, where the inclusion of CNT in the vitrimer was helpful to acclaim NIR light/low-temperature shape recovery and transesterification exchanges. Significantly, an addition of 0.3 wt% CNT resulted in a prominent shape memory via thermal (at 60°C) and near-infrared (NIR) light [27]. Furthermore, transcarbonation exchange-promoted vitrimers were studied with cellulose paper, where the paper has introduced hydrogen bonds with polycarbonate covalent bonds. Also, the performed vitrimer composite described the prudent self-healing and shape memory properties [28].

In addition to achieve more sustainable composites, sugarcane bagasse-derived activated carbon/bio-based fillers have been unified in an epoxy vitrimer system to achieve a low-temperature self-healing material (via the reduction of T_g). Inquisitively, sugarcane bagasse-derived activated carbon-(AC-) epoxy vitrimer biocomposites including their thermo-mechanical and self-healing properties have not been explored yet. In the effort to prepare sustainable bio-based vitrimers, biofiller involvement in vitrimers has been of great demand and required much attention by the researchers; thus, herein, we present an epoxy vitrimer biocomposite sugarcane bagasse-derived chemically activated carbon (AC) as biofiller. Owing to this, the biocomposite vitrimer is designed with aromatic disulfide crosslink-assisted self-healing; also, different concentrations of AC are used to optimize chemical and mechanical properties of epoxy vitrimer biocomposites. The influence of AC on the glass transition temperature (T_g) of the matrix has also been studied. The self-healing efficiency (based on a covalently adaptive network) through flexural studies and active carbon dependent changes on healing and thermo-mechanical performances have been eloquently addressed.

2. Experimental Section

2.1. Material and Methods. Bisphenol A diglycidyl ether (BADGE) (340.41 g/mol) resin, 40 wt% phosphoric acid (BDH grade), and 2-aminophenyl disulfide (AFD) (248.37 g/mol) hardener were used as received from Sigma-Aldrich.

2.2. Preparation of Epoxy Vitrimer Biocomposites. Activated carbon was prepared from sugarcane refuses, based on the literature (supporting information (SI) (available here)) [29]. The prepared AC was dispersed in ethanol (150 mg in 10 mL) via ultrasonication for 30 min. Subsequently, finely dispersed activated carbon in different loadings (EP-x%; x-0 (p-pristine), 0.1, 0.2, 0.5, 1, and 2) was added in BADGE resin and heated at 80°C under vacuum condition till ethanol evaporation. Thereafter, a stoichiometric ratio of hardener 2-aminophenyl disulfide (AFD) was added and stirred at the same temperature for 15 min. Finally, the degassed mixture was kept in a silicon mold and cured at 150°C for 5 h.

2.3. Preparation of Conventional Thermoset Epoxy Biocomposite. To evaluate the effect of AFD incorporation onto self-healing properties, AFD free activated carbon-based conventional thermoset epoxy biocomposites were also prepared. Activated carbon-dispersed ethanol solution was added in BADGE (500 mg, 1.47 mmol) resin at 80°C temperature with stirring. After evaporation of ethanol, weighed DETA (60 mg, 0.5 mmol) was added and stirred at 40°C for 15 min. Then, the mixture was poured in a silicon mold

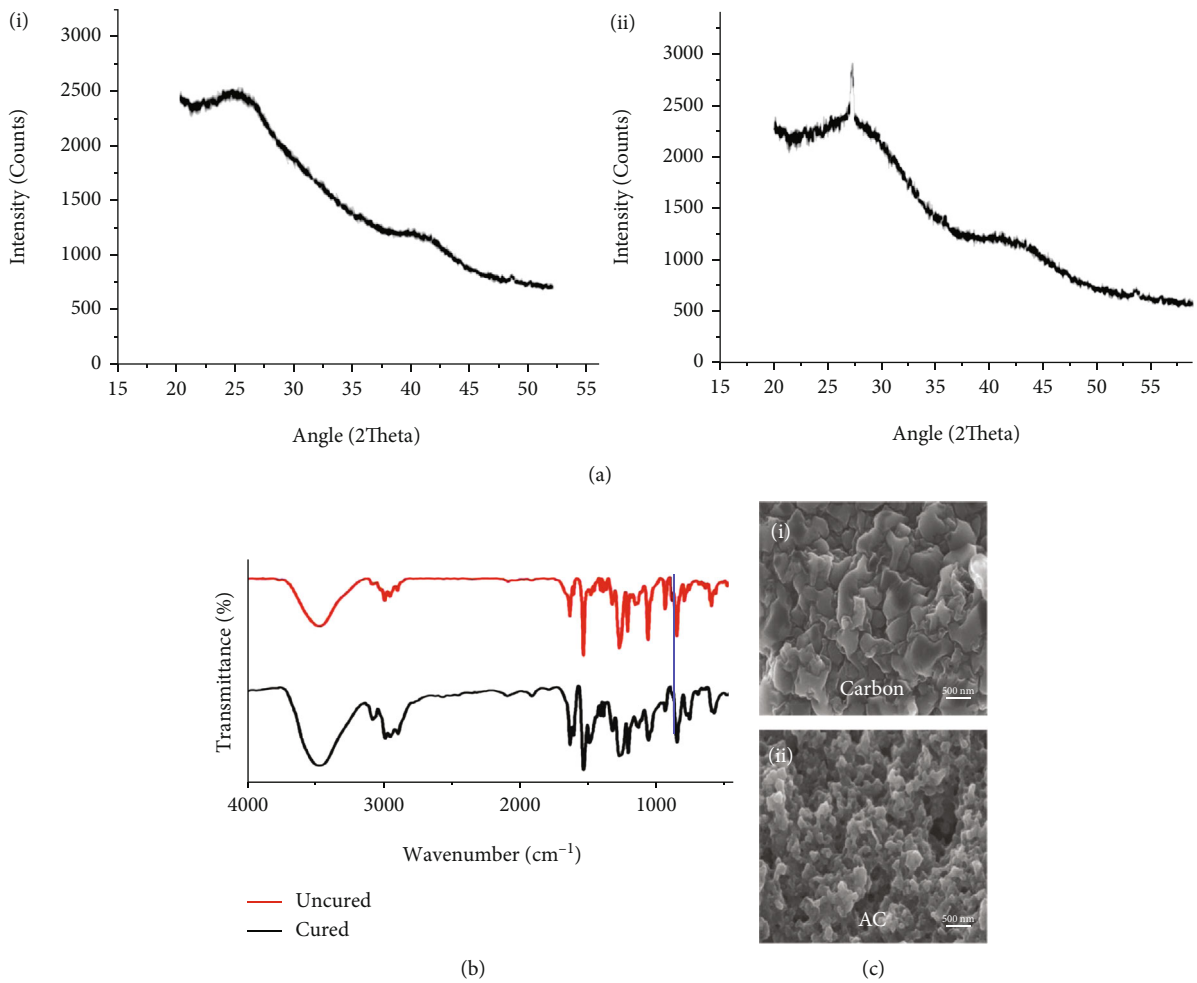

Figure 1: (a) XRD pattern of activated carbon (AC). (b) FT-IR spectra for uncured and cured epoxy. (c) SEM images for biomass-derived (i) carbon and (ii) activated carbon.

and kept at room temperature for 24 h. The obtained specimens were involved in different studies.

2.4. Characterization Techniques. X-ray diffraction spectroscopy was analyzed through D8 ADVANCE ECO–Bruker to identify the activated carbon. Scanning electron microscopy (SEM; Quanta FEG 200) analysis was used to observe the surface of activated carbon. The epoxy curing was observed through FT-IR (Frontier FT-IR/FIR, PerkinElmer) spectra analysis. T_g was characterized using thermomechanical analyzer (TA-Q400 EM) dimensional change experiments. In TA-Q400 EM, a three-point bending test was performed to address the storage modulus, loss modulus, stress relaxation, and stress-strain behavior of the rectangular specimens ($15 \times 5 \times 0.5$ mm). All dimensional change, storage modulus, and loss modulus experiments were performed through temperature ranges from 40°C to 120°C using heating rates of 10°C/min with 50 mL/min nitrogen purge gas flow and 0.02 N force. In the stress relaxation study, 1×10^{-3} N preloaded force was applied to straighten the specimen. During the test, the required temperature and 1% strain were applied, and then, relaxation modulus was evaluated with respect to time. Stress-strain experiments were performed in strain ramp mode with 0.02 N force and evaluated strain at 40°C isothermal temperature.

3. Results and Discussions

3.1. Material Characterization. Biomass-derived carbon and AC were investigated by XRD analysis to identify their formation from biomass (Figure 1(a), (i) and (ii)). The performed XRD for biomass-derived carbon has resulted in a broad peak around 26°, where the absence of sharp peaks denoted the amorphous structure. Subsequently, the performed AC exhibited that narrow peaks have indicated the regularity of crystalline structure and layer integral formation with adequate surface volume [30, 31]. Altogether, the observed peak at 26.27° is a characteristic of graphite flake-like hexagonal structure, and therefore, AC can also be termed as assemblies of defective graphene [21]. Thus, the chemically activated carbon (comprised of graphite and π electron-connected graphene layer) exhibits an intense porosity, which has an increase in surface area, despite that it deforms the graphene layer structure [32, 33]. SEM analysis shows the sugarcane bagasse-derived carbon and activated carbon surface, in which chemically (phosphoric acid) activated carbon highlights pores on its

Table 1: Glass transition temperature of epoxy nanocomposites.

Samples	Epoxy-AC (EP-x)					
	EP-p	EP-0.1	EP-0.2	EP-0.5	EP-1	EP-2
Glass transition temperature (T_g)	64	63	60	59.2	59	59.8

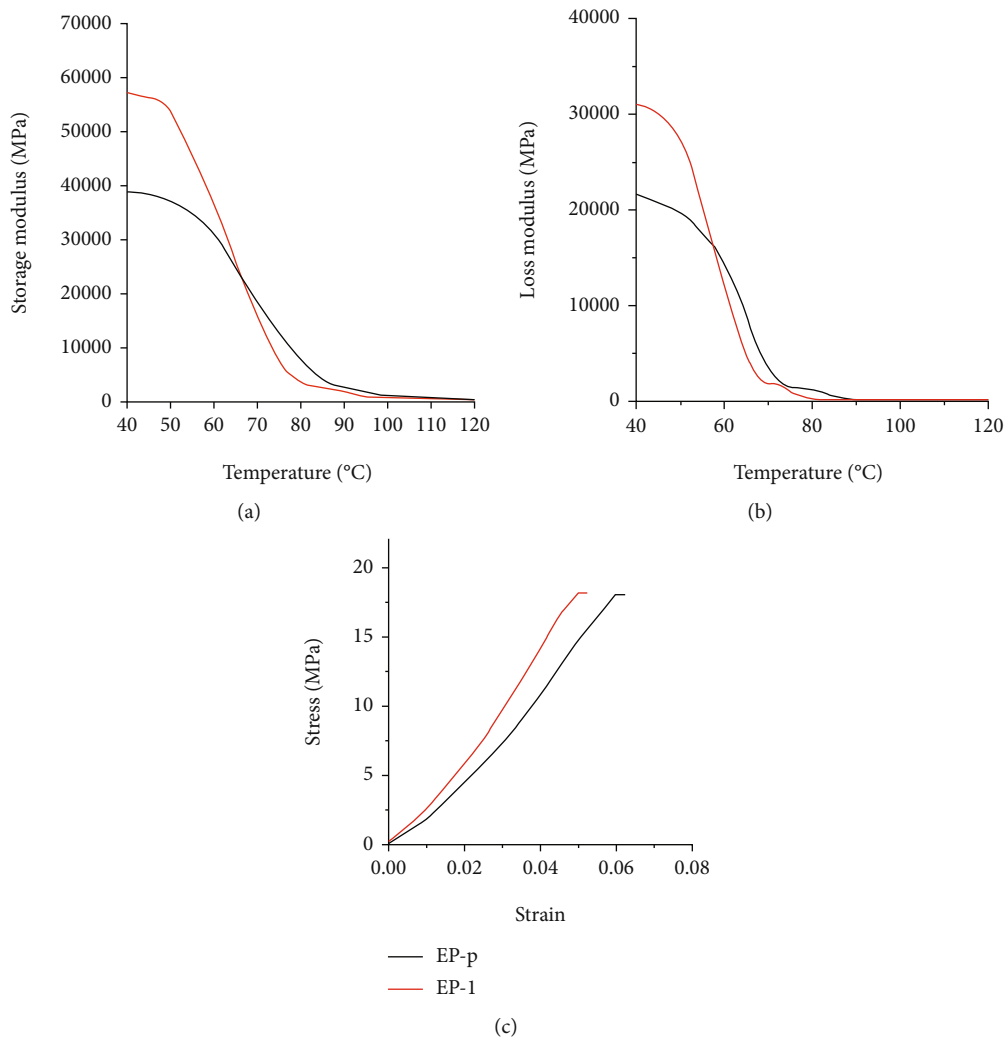

Figure 2: (a) Storage modulus, (b) loss modulus, and (c) flexural stress-strain curve for epoxy and biocomposite vitrimers.

surface (Figure 1(c), (i) and (ii)). These low-volume pores confer to AC the capability to extend the surface area for chemical reactions and are helpful to attain progressive chain exchanges. FT-IR analysis was performed to analyze the curing of epoxy vitrimer biocomposites, where the diminution of oxirane ring (915 cm^{-1}) was observed and denoted a complete curing of epoxy (Figure 1(b)) [34]. The epoxy curing was noted at the interval of every one hour using FT-IR analysis, and it was found that the curing was complete after 5 h (see Figure S1).

3.2. Thermomechanical Properties. Thermomechanical properties of AC-epoxy vitrimer biocomposites were investigated through a thermomechanical analyzer, which allows the determination of their T_g and dynamic mechanical performance. The determined T_g for the pristine epoxy vitrimer and the AC-epoxy vitrimer biocomposites loaded with different percentages of AC filler are tabulated in Table 1 (see Figure S2). From the observed results, material EP-1 denotes the lowest T_g among the investigated epoxy samples. A reduction in T_g was observed for all biocomposites, which could be due to the free volume space between matrix and nanofillers [35], and thus enhances the chain mobility helpful to achieve low-temperature self-healing properties. However, further addition of filler leads to slight increase in T_g, which could be due to agglomeration of nanofillers in epoxy matrix [36, 37].

Storage modulus and loss modulus of the pristine epoxy vitrimer and AC-epoxy vitrimer biocomposites were observed to understand the temperature-dependent viscoelasticity

Table 2: Dynamic properties of epoxy for epoxy and biocomposite vitrimers.

Samples	Storage modulus (GPa)	Flexural strength (MPa)	Flexural strain at break (mm/mm)	Flexural modulus (GPa)	Activation energy (E_a) (kJ/mol)	Topology transition temperature (T_v) (°C)	Before healing (GPa)	After healing (GPa)	
								1st	2nd
EP-p	39.7	18.0	0.06	32.1	59	19	32.1	23.4	19.5
EP-1	57.5	18.1	0.05	43.3	79	43	43.3	36.9	33.7

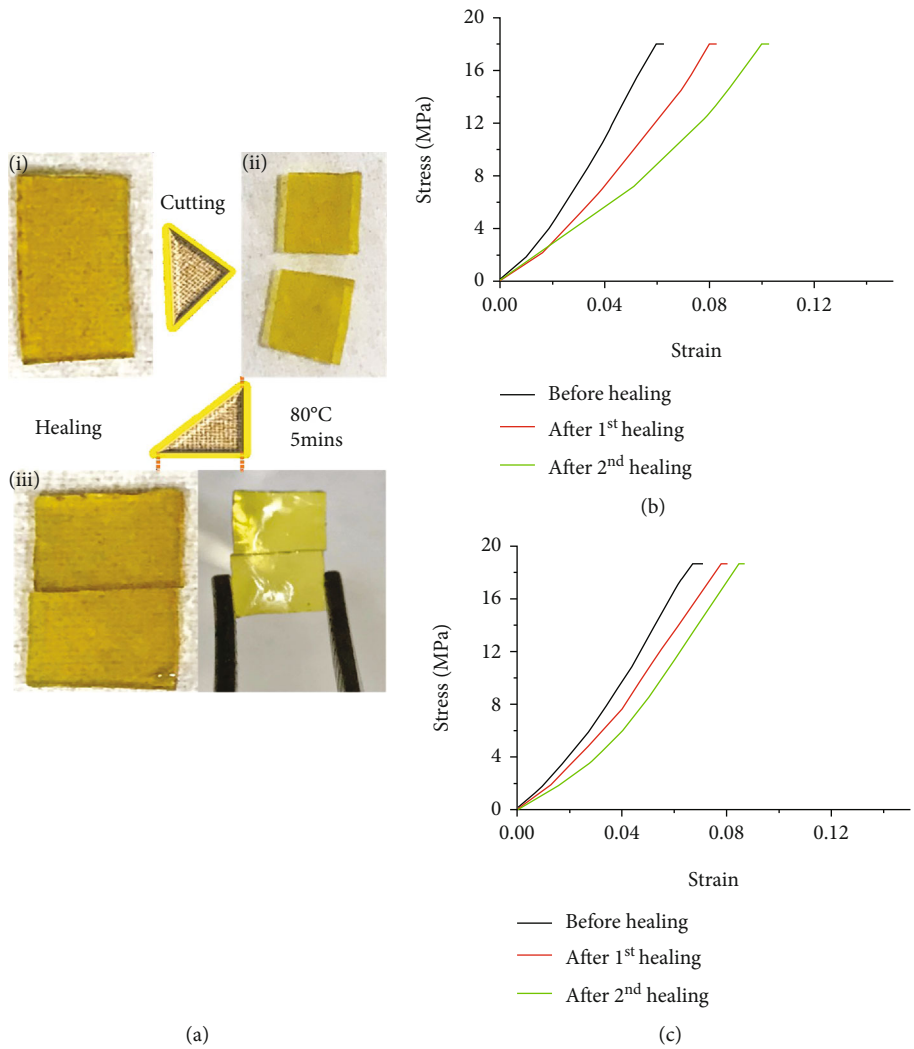

Figure 3: (a) Self-healing of epoxy vitrimer: (i) pristine EP-p, (ii) cut into two pieces, and (iii) rejoined. Healing efficiency of vitrimer was calculated via the stress-strain relationship for (b) EP-p and (c) EP-1.

(Figures 2(a) and 2(b)). It was found that biocomposites with 1 wt% of AC exhibit a higher storage modulus than pristine epoxy vitrimer. EP-1 demonstrates a higher storage modulus (Table 2) due to the presence of activated carbon, where matrix-interlocked fillers have restricted the chain exchanges at lower temperature. However, EP-1 has availed a faster reduction in viscoelasticity (above T_g), where the addition of AC has reduced the glass transition temperature (T_g) of the epoxy vitrimer (due to filler and matrix free volume space). During the period of temperature change, the performed material EP-1 has exhibited a faster decline in storage and loss modulus than the pristine sample; thus, performed material viscoelasticity (storage and loss modulus) was entirely dependent with the solid to rubbery phase change temperature (i.e., glass transition temperature) [4].

A three-point bending test using the force ramp mode at 40°C was performed for calculating the stress-strain behavior of the prepared samples. The pristine and biocomposite vitrimers demonstrate a similar stress-strain behavior (Figure 2(c)). However, a lower strain at break and a higher flexural modulus of AC-epoxy vitrimer biocomposite compared to pristine epoxy vitrimer denote

the stiffness increment as well as high bending resistance upon the incorporation of AC. A 35% increment in flexural modulus was obtained with the addition of AC nanofillers (Table 2).

3.3. Stress Relaxation. Stress relaxation experiments were performed for the EP-p and EP-1 at different temperatures (60°C, 70°C, and 80°C); hence, resulted relaxation times (EP-p = 112.8 s, 40.8 s, and 34 s; EP-1 = 234 s, 129.6 s, and 46.2 s, respectively) were plotted in the Arrhenius equation (Figures S3 and S4) to identify the activation energy of the pristine epoxy vitrimer and its biocomposites (SI) [38].

The investigated relaxation time for EP-p was comparatively lower than that for EP-1. This could be due to the presence of activated carbon, which has restricted the chain mobility and increased the viscosity of epoxy vitrimer. However, free volume formation between filler and matrix was found to be the key component for reduction in glass transition temperature [35].

3.4. Self-Healing Mechanical Properties. The performed first healing of pristine epoxy vitrimer and AC-epoxy vitrimer biocomposite demonstrates efficient self-healing via disulfide exchanges (Figure 3(a); video 1). The specimen was cut into two pieces with the help of a razor blade, both the pieces were immediately kept together at 70°C for 5 min, and the healing efficiency was evaluated from the stress-strain relationship. The activated carbon involving EP-1 demonstrates self-healing at 70°C, owing to their low glass transition temperature, as low T_g is helpful to achieve the S-S bond rearrangement. Disulfide-mediated radical exchange is the key factor for achieving the self-healing behavior for vitrimeric materials [39], as conventional epoxy specimen devoid of 2-aminophenyl disulfide does not show the healing properties. The healing efficiency was evaluated through flexural studies (Figures 3(b) and 3(c)), where healed pristine epoxy vitrimer and AC-epoxy vitrimer biocomposites demonstrate healing efficiency 73% and 85%, respectively, after the first cycle. Then, the performed second healing demonstrates a 60% and 78% healing; a reduction in healing efficiency after each cycle was observed. However, material flexural strength was quite similar after every healing cycle, whereas a change in flexural modulus and strain at break was observed.

4. Conclusion

It is concluded that activated carbon from sugarcane bagasse could be an effective filler to achieve sustainable epoxy vitrimer biocomposite. The high surface area of activated carbon in AC-epoxy vitrimer biocomposite makes them capable to achieve progressive chain exchanges. The disulfide exchanges promoted temperature-dependent self-healing observed at 80°C for 5 min in pristine epoxy vitrimer, and the material had demonstrated a lower temperature self-healing at 70°C for 5 min upon the addition of activated carbon. Healing efficiency evaluated via flexural studies highlighted a prominent recovery in vitrimer biocomposites with 1 wt % of AC (EP-1), where 85% and 70% efficiency was exhibited after two consecutive healings. In the future, biocomposite vitrimer study would be helpful to envisage efficient vitrimer composite materials for real-time applications with sustainable properties.

Data Availability

The data used to support the findings of this study are available from the corresponding author upon request.

Conflicts of Interest

The authors declare no conflict of interest.

Acknowledgments

We gratefully acknowledge the financial support from the Science and Engineering Research Board (SERB-DST), Government of India (Grant No. ECR/2016/001355).

Supplementary Materials

Table 1: different nanocomposite percentage prepared with an addition of dispersed solutions (AC). Figure S1: FT-IR results for EP-pristine curing with respect to time. Figure S2: glass transition temperatures for different percentages of activated carbon involved epoxy vitrimer (1-5). Figure S3: Arrhenius equation plotted graph (ln $(\tau *)$ vs. $1/T$) for EP-p. Figure S4: Arrhenius equation plotted graph (ln $(\tau *)$ vs. $1/T$) for EP-1. *(Supplementary Materials)*

References

[1] K. Varaprasad, M. Pariguana, G. M. Raghavendra, T. Jayaramudu, and E. R. Sadiku, "Development of biodegradable metaloxide/polymer nanocomposite films based on poly-ε-caprolactone and terephthalic acid," *Materials Science and Engineering: C*, vol. 70, Part 1, pp. 85–93, 2017.

[2] L. Guadagno, M. Raimondo, C. Naddeo, P. Longo, and A. Mariconda, "Self-healing materials for structural applications," *Polymer Engineering and Science*, vol. 54, no. 4, pp. 777–784, 2014.

[3] M. Raimondo and L. Guadagno, "Healing efficiency of epoxy-based materials for structural applications," *Polymer Composites*, vol. 34, no. 9, pp. 1525–1532, 2013.

[4] L. Guadagno, L. Vertuccio, C. Naddeo et al., "Self-healing epoxy nanocomposites via reversible hydrogen bonding," *Composites. Part B, Engineering*, vol. 157, pp. 1–13, 2019.

[5] L. Guadagno, L. Vertuccio, C. Naddeo et al., "Reversible self-healing carbon-based nanocomposites for structural applications," *Polymers (Basel)*, vol. 11, no. 5, p. 903, 2019.

[6] B. Krishnakumar, R. V. S. P. Sanka, W. H. Binder, V. Parthasarthy, S. Rana, and N. Karak, "Vitrimers: associative dynamic covalent adaptive networks in thermoset polymers," *Chemical Engineering Journal*, vol. 385, p. 123820, 2019.

[7] A. M. Peterson, R. E. Jensen, and G. R. Palmese, "Thermoreversible and remendable glass–polymer interface for fiber-reinforced composites," *Composites Science and Technology*, vol. 71, no. 5, pp. 586–592, 2011.

[8] D. Montarnal, M. Capelot, F. Tournilhac, and L. Leibler, "Silica-like malleable materials from permanent organic networks," *Science*, vol. 334, no. 6058, pp. 965–968, 2011.

[9] H. Zhang and X. Xu, "Improving the transesterification and electrical conductivity of vitrimers by doping with conductive polymer wrapped carbon nanotubes," *Composites. Part A, Applied Science and Manufacturing*, vol. 99, pp. 15–22, 2017.

[10] D. J. Fortman, J. P. Brutman, C. J. Cramer, M. A. Hillmyer, and W. R. Dichtel, "Mechanically activated, catalyst-free polyhydroxyurethane vitrimers," *Journal of the American Chemical Society*, vol. 137, no. 44, pp. 14019–14022, 2015.

[11] W. Denissen, G. Rivero, R. Nicolaÿ, L. Leibler, J. M. Winne, and F. E. Du Prez, "Vinylogous urethane vitrimers," *Advanced Functional Materials*, vol. 25, no. 16, pp. 2451–2457, 2015.

[12] Y. Xu and D. Chen, "A novel self-healing polyurethane based on disulfide bonds," *Macromolecular Chemistry and Physics*, vol. 217, no. 10, pp. 1191–1196, 2016.

[13] J. Han, T. Liu, C. Hao, S. Zhang, B. Guo, and J. Zhang, "A catalyst-free epoxy vitrimer system based on multifunctional hyperbranched polymer," *Macromolecules*, vol. 51, no. 17, pp. 6789–6799, 2018.

[14] Z. Yang, Q. Wang, and T. Wang, "Dual-triggered and thermally reconfigurable shape memory graphene-vitrimer composites," *ACS Applied Materials & Interfaces*, vol. 8, no. 33, pp. 21691–21699, 2016.

[15] Y. Zhu, F. Gao, J. Zhong, L. Shen, and Y. Lin, "Renewable castor oil and DL-limonene derived fully bio-based vinylogous urethane vitrimers," *European Polymer Journal*, vol. 135, p. 109865, 2020.

[16] H. Zheng, Q. Liu, X. Lei, Y. Chen, B. Zhang, and Q. Zhang, "A conjugation polyimine vitrimer: fabrication and performance," *Journal of Polymer Science Part A: Polymer Chemistry*, vol. 56, no. 22, pp. 2531–2538, 2018.

[17] A. Ruiz de Luzuriaga, R. Martin, N. Markaide et al., "Epoxy resin with exchangeable disulfide crosslinks to obtain reprocessable, repairable and recyclable fiber-reinforced thermoset composites," *Materials Horizons*, vol. 3, no. 3, pp. 241–247, 2016.

[18] B. Krishnakumar, M. Singh, V. Parthasarthy et al., "Disulfide exchange assisted self-healing epoxy/PDMS/graphene oxide nanocomposites," *Nanoscale Advances*, vol. 2, no. 7, pp. 2726–2730, 2020.

[19] J. Tang, L. Wan, Y. Zhou, H. Pan, and F. Huang, "Strong and efficient self-healing adhesives based on dynamic quaternization cross-links," *Journal of Materials Chemistry A*, vol. 5, no. 40, pp. 21169–21177, 2017.

[20] Q. Chen, Y. Li, Y. Yang et al., "Durable liquid-crystalline vitrimer actuators," *Chemical Science*, vol. 10, no. 10, pp. 3025–3030, 2019.

[21] X. Hu, M. Fan, B. F. Towler, M. Radosz, D. A. Bell, and O. A. Plumb, "Hydrogen adsorption and storage," in *Coal Gasification and Its Applications*, pp. 157–245, Elsevier Inc., 2011.

[22] S. Dhers, G. Vantomme, and L. Avérous, "A fully bio-based polyimine vitrimer derived from fructose," *Green Chemistry*, vol. 21, no. 7, pp. 1596–1601, 2019.

[23] Z. Ma, Y. Wang, J. Zhu, J. Yu, and Z. Hu, "Bio-based epoxy vitrimers: reprocessibility, controllable shape memory, and degradability," *Journal of Polymer Science Part A: Polymer Chemistry*, vol. 55, no. 10, pp. 1790–1799, 2017.

[24] Z. Guo, B. Liu, L. Zhou et al., "Preparation of environmentally friendly bio-based vitrimers from vanillin derivatives by introducing two types of dynamic covalent C N and S-S bonds," *Polymer*, vol. 197, p. 122483, 2020.

[25] R. P. Babu, K. O'Connor, and R. Seeram, "Current progress on bio-based polymers and their future trends," *Progress in Biomaterials*, vol. 2, no. 1, p. 8, 2013.

[26] X. Yang, L. Guo, X. Xu, S. Shang, and H. Liu, "A fully bio-based epoxy vitrimer: self-healing, triple-shape memory and reprocessing triggered by dynamic covalent bond exchange," *Materials and Design*, vol. 186, p. 108248, 2020.

[27] P. Kasemsiri, N. Lorwanishpaisarn, U. Pongsa, and S. Ando, "Reconfigurable shape memory and self-welding properties of epoxy phenolic novolac/cashew nut shell liquid composites reinforced with carbon nanotubes," *Polymers*, vol. 10, no. 5, p. 482, 2018.

[28] W. Zhao, Z. Feng, Z. Liang et al., "Vitrimer-cellulose paper composites: a new class of strong, smart, green, and sustainable materials," *ACS Applied Materials & Interfaces*, vol. 11, no. 39, pp. 36090–36099, 2019.

[29] D. Bose, S. Sridharan, H. Dhawan, P. Vijay, and M. Gopinath, "Biomass derived activated carbon cathode performance for sustainable power generation from microbial fuel cells," *Fuel*, vol. 236, pp. 325–337, 2019.

[30] M. Pawlyta, J. N. Rouzaud, and S. Duber, "Raman microspectroscopy characterization of carbon blacks: spectral analysis and structural information," *Carbon*, vol. 84, pp. 479–490, 2015.

[31] A. Omri and M. Benzina, "Characterization of activated carbon prepared from a new raw lignocellulosic material : Ziziphus spina-christi seeds," *Journal de la Société Chimique de Tunisie*, vol. 14, pp. 175–183, 2012.

[32] Y. Soo, N. Chada, M. Beckner, J. Romanos, J. Burress, and P. Pfeifer, "Adsorbed methane film properties in nanoporous carbon monoliths," *Proceedings of the APS March Meeting Abstracts*, vol. 2013, article M38.001, 2013.

[33] M. K. Nazal, "An overview of carbon-based materials for the removal of pharmaceutical active compounds," in *Carbon-Based Material for Environmental Protection and Remediation*, M. Bartoli, M. Frediani, and L. Rosi, Eds., IntechOpen, Rijeka, 2020.

[34] L. Guadagno, L. Vertuccio, A. Sorrentino et al., "Mechanical and barrier properties of epoxy resin filled with multi-walled carbon nanotubes," *Carbon*, vol. 47, no. 10, pp. 2419–2430, 2009.

[35] C. Park, J. Jung, and G. J. Yun, "Thermomechanical properties of mineralized nitrogen-doped carbon nanotube/polymer nanocomposites by molecular dynamics simulations," *Composites. Part B, Engineering*, vol. 161, pp. 639–650, 2019.

[36] G. B. Olowojoba, S. Kopsidas, S. Eslava et al., "A facile way to produce epoxy nanocomposites having excellent thermal conductivity with low contents of reduced graphene oxide," *Journal of Materials Science*, vol. 52, no. 12, pp. 7323–7344, 2017.

[37] N. G. Sahoo, S. Rana, J. W. Cho, L. Li, and S. H. Chan, "Polymer nanocomposites based on functionalized carbon nanotubes," *Progress in Polymer Science*, vol. 35, no. 7, pp. 837–867, 2010.

[38] B. Krishnakumar, R. V. S. P. Sanka, W. Binder, Y. C. Jung, V. Michaud, and N. Sahoo, *Submission Files Included in This PDF Submission Files Not Included in This PDF Research Data Related to This Submission Composites Part B : Engineering Dear*, S. Rana, Ed., PhD University of Petroleum & Energy Studies (UPES), 2020.

[39] B. Krishnakumar, R. V. S. Prasanna Sanka, W. H. Binder et al., "Catalyst free self-healable vitrimer/graphene oxide nanocomposites," *Composites. Part B, Engineering*, vol. 184, p. 107647, 2020.

Hindawi
International Journal of Polymer Science
Volume 2021, Article ID 6617138, 13 pages
https://doi.org/10.1155/2021/6617138

Research Article

Corrosion Resistance Evaluation of Self-Healing Epoxy Coating Based on Dual-Component Capsules Containing Resin and Curing Agent

Alireza Safdari,[1] Saied Nouri Khorasani,[1] Rasoul Esmaeely Neisiany,[2] and Mohammad Sadegh Koochaki[1,3]

[1]*Department of Chemical Engineering, Isfahan University of Technology, Isfahan 84156-83111, Iran*
[2]*Department of Materials and Polymer Engineering, Faculty of Engineering, Hakim Sabzevari University, Sabzevar 9617976487, Iran*
[3]*Research and Development Department, Alvan Paint & Resin Production Co., Tehran 13991-53611, Iran*

Correspondence should be addressed to Saied Nouri Khorasani; saied@cc.iut.ac.ir
and Rasoul Esmaeely Neisiany; r.esmaeely@hsu.ac.ir

Received 29 October 2020; Revised 28 February 2021; Accepted 5 March 2021; Published 18 March 2021

Academic Editor: Poornima Vijayan P

In this study, a self-healing epoxy coating was prepared by incorporating a dual capsule healing system including epoxy resin and its amine-based curing agent. The emulsion electrospray technique was used for encapsulating the healing agents in poly(styrene co-acrylonitrile) (SAN) as shell material. Characterizing the prepared microcapsules (MCs) by Scanning Electron Microscopy (SEM) revealed their spherical morphology with the particle size of 827 nm and 749 nm for epoxy and amine cores, respectively. Fourier Transform Infrared Spectroscopy (FT-IR) and thermogravimetric analysis (TGA) results confirmed successful encapsulation with no side chemical reaction between the encapsulated core and shell materials. The effects of embedding MCs on the physical and mechanical properties of the epoxy coating matrix were studied by pull-off adhesion, conical mandrel bending, and gloss tests. In addition, the prepared coatings' self-healing performance was evaluated by Electrochemical Impedance Spectroscopy (EIS) and potentiodynamic polarization (Tafel) experiments. The results revealed that the coating sample containing 1 wt% of core-shell MCs (a mixture of epoxy and amine-containing MCs with a 50 : 50 weight ratio) showed the best corrosion performance with 99% self-healing efficiency.

1. Introduction

Corrosion of metals is regarded as an important and challenging issue in many industries. According to recent studies, the global corrosion cost is estimated to be 3.1% of the countries' gross domestic product (GPD). Using polymeric barrier coatings is a well-known approach for metal corrosion prevention or deceleration. However, the most important limitation in polymers is the occurrence of microcracks in the matrix which leads to fracture if not controlled [1–4]. These faults cannot be repaired by conventional methods as they are not visible at the beginning. Therefore, in the 1980s, self-healing polymers were introduced as an effective solution for healing the microcracks and fracture prevention in order to achieve a better life span and safety of polymeric devices [5–9]. Self-healing materials are classified into two main classes including extrinsic [10–14] and intrinsic [15–17] systems based on the healing mechanism. Extrinsic systems based on the healing agent release have shown great efficiency among other methods [18].

Since the fracture in polymers begins at nanometer scales by crack formation and growth, reducing the size of capsules to submicron is crucial to enable the healing at the nanoscale as soon as the crack is formed and consequently prevent its growth [19–22]. Capsule based self-healing polymeric coatings utilize controlled release of active agents upon crack formation. These active healing agents are surrounded by shell capsules and added to the polymeric matrix. Crack formation in the coating matrix leads to the capsule rapture and subsequently healing agent release which will automatically repair

the crack. White et al. reported the application of MCs based self-healing systems for repairing microcracks and increasing the life span of polymer composites [23]. Subsequently, several methods including in situ polymerization, solvent evaporation, and multistage emulsion polymerization have been employed to encapsulate healing agents within the micro/nanocapsules, while these methods are costly, time-consuming, and need for purification. Recently, electrospinning and electrospray have been used for the encapsulation healing agents within nanofibers or MCs to address the abovementioned shortcomings [24, 25]. Park et al. encapsulated bicomponent dimethylsiloxane in a polyvinylpyrrolidone shell in two distinct steps using the coaxial electrospinning method. The resulted core-shell nanofibers were placed on a steel surface prior to the application of an acrylic-urethane coating on them. The self-healing ability of the system was tested [26]. Lee et al. reported the preparation of a self-healing silicone-based coating by encapsulating bicomponent dimethylsiloxane in a polyacrylonitrile shell through emulsion electrospinning and adding them to a polydimethylsiloxane based coating [27]. Hia et al. encapsulated epoxy resin within alginate shell material through the emulsion electrospray method [28]. The average size of the prepared MCs was reported at $575 \pm 25\,\mu$m, and the MCs were employed to develop a self-healing composite with a healing efficiency of 50%. Koochaki et al. developed a dual capsule healing system using polyetheramine and methylene diphenyl diisocyanate as a core within the SAN shell. The mentioned system showed high healing efficiency of 85% in an epoxy-based coating [29]. The coaxial electrospray method was employed by Malekkhouyan et al. [24] to encapsulate Coconut-Oil-Based Alkyd Resin within SAN capsules with a mean capsule diameter of 708 ± 252 nm. The incorporation of the prepared capsules within epoxy resin provided a self-healing epoxy-based coating with a healing efficiency of 95%. Recently, Ataei et al. [30] employed electrospray method for the preparation of core-shell capsules containing epoxy resin and its thiol-based curing agent as a dual component healing system for the development of a self-healing epoxy-based coating.

In this research, the electrospray was the method to develop a dual capsule self-healing system based on epoxy resin and amine-based curing agents. For this purpose, epoxy resin and amine-based curing agents were separately encapsulated by SAN shell and subsequently incorporated in an epoxy matrix to prepare a dual-component self-healing anticorrosion coating. Considering the fast reaction between the epoxy resin and the amine group in curing agents at room temperature without any more required additional catalyst, the prepared system offers high healing efficiency at room temperature.

2. Experimental Section

2.1. Materials. SAN with an average molecular weight of 185000 g/mol and 30% acrylonitrile content was purchased from Sigma-Aldrich to be used as capsule shell material. SAN was used as shell material due to its high capability for encapsulation of materials during electrospray and electrospinning methods [24, 31] and excellent interaction with epoxy coating [32]. Dimethylformamide (DMF) was provided by DaeJung Co. and used as a solvent for preparing the polymer solution. Bisphenol F epoxy resin (Indox E210-Inchem ltd) and cycloaliphatic polyamine (EPIKURE F205-Hexion) were used as the core materials for preparing the dual capsule healing system. Bisphenol A epoxy resin (EPON 828-Hexion) and polyamidoamine curing agent (Merginamide A280-HOBUM Oleochemicals) were employed to prepare the coatings' matrix. 1,6-Hexanediol diglycdil ether (Indox ED180-Inchem ltd) was utilized as a reactive diluent for reducing the viscosity of the coating matrix.

2.2. Sample Preparation

2.2.1. Preparation of Core-Shell Capsules. At first, the SAN copolymer powder was placed in a vacuum oven at 50°C for 12 hours to remove any humidity and then dissolved in DMF at lab conditions by magnetic stirring for 24 hours to obtain a homogeneous shell solution (4% w/v). Afterwards, the core materials (Bisphenol F epoxy resin and cycloaliphatic polyamine) were separately added to the prepared shell solutions (1 : 1 core/shell weight ratio) and mixed by magnetic stirring for 2 hours followed by 20 minutes of sonication in an ultrasonic bath. The resulted mixtures were fed to 1 ml syringes with a bundle 23 gauge needle. The electrospray process (Figure 1) was carried out at the broad ranges of applied voltage, feed rate, and the needle to collector distance to find the right conditions for preparing particles. The optimum values of electrospray parameters were obtained at an applied voltage of 24 kV and a flow rate of 0.3 ml h^{-1}. The distance between the needle tip and the collector was set at 15 cm to allow complete solvent evaporation during the spray process. Neat SAN particles were prepared by applying the same procedure for further characterizations.

2.2.2. The Preparation of Coatings for Corrosion and Mechanical Tests. To prepare the self-healing coatings, bisphenol A epoxy resin and the reactive diluent (1,6-hexanediol diglycidyl ether) were mixed with a 3 : 1 weight ratio. Then, the prepared capsules were added to the epoxy resin mixture and dispersed by mechanical stirring at 200 rpm for 5 min. Three different capsule contents (1, 5, and 10 wt%) were added to the matrix to study their effects on the self-healing performance and coating characteristics. The weight ratio of epoxy-containing capsules to amine-containing ones was kept 1 : 1 for all samples. The polyamidoamine curing agent was then added to the mixtures at a 100 : 58 of epoxy : amine weight ratio to cure the epoxy resin. The resulted mixtures were immediately coated on cleaned and sanded ST-37 steel plates with a thickness of 150 μm by a thin-film applicator. The substrate composition was assessed according to ASTM E415 using an ARUN 2500 quantometer, and the results are presented in Table 1 [33]. Moreover, a neat coating including no MCs was applied with the same conditions as the control sample (CTRL) to study the effects of MC addition on the coating's characteristics. All the coatings were kept in the laboratory for 7 days to ensure complete curing.

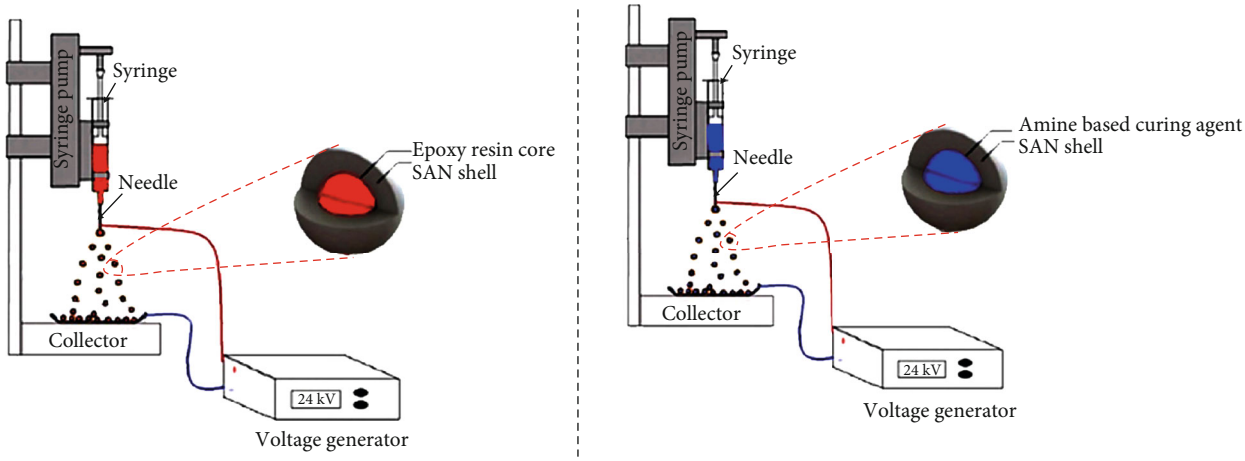

Figure 1: The schematic figure of employed electrospray set up to separately encapsulate epoxy and amine-based curing agent within SAN capsules.

Table 1: The St-37 substrate chemical composition.

Elements	Mn	C	Cr	Si	S	P	Fe
Weight percent (%)	0.512	0.112	0.045	0.028	0.008	0.007	Bal

2.3. Characterizations

2.3.1. Characterization of the Prepared Capsules. FTIR (WQF-510A, RAYLEIGH, China) was used to characterize the chemical structure of the prepared capsules and their corresponding core and shell materials. The analysis was conducted using KBr pellets in a wavelength range of 4000-400 cm^{-1}.

SEM (Philips-XII30, Netherlands) was employed to study the morphology and particle size of the prepared capsules. All the samples were firstly gold-sputtered for 120 seconds at 10 mAh before testing. The ImageJ software was used to determine the particle size and size distribution according to the SEM images. Moreover, transmission electron microscopy (2100F, JEOL, Japan) operating a 200 kV Schottky field emitter was utilized to study the core-shell structure of the capsules which were sprayed on Lacey Formvar/carbon-coated copper grids prior to testing.

To study the thermal stability and composition of the prepared capsules, thermogravimetric analysis (STA 6000 TGA system, Perkin Elmer, USA) was performed under a nitrogen atmosphere with a heating rate of 10°C/min from 25 to 800°C. To investigate the plausible reactions between the released healing agents, differential scanning differential analysis (DSC302, KBAHR–Germany) was used.

The encapsulation yield was measured for both epoxy and amine contained MCs by extraction method [31]. To perform the core extraction, each kind of MCs was crushed separately in a mortar to break their shell. Then, the core was washed from the crushed mixture with ethanol for several times, and the shell was filtered prior to being dried at 40°C for 24 h in an oven. The core content was then measured, and the core content was determined according to Eq. (1) as follows:

$$\%\text{Core content}(W_{ex}) = \frac{(W_{ca} - W_{sh})}{W_{ca}} \times 100, \quad (1)$$

where W_{ca} and W_{sh} are associated with the weight of MCs and shell, respectively. Consequently, the encapsulation yield was determined for both core materials using Eq. (2):

$$\%\text{Encapsulation yield} = \left(\frac{W_{ex}}{W_{th}}\right) \times 100. \quad (2)$$

The W_{th} was calculated theoretically according to the weight ratio of core and shell materials in the syringe feed solution.

2.3.2. Characterization of Coatings. The pull-off adhesion test (PosiTest AT-M, Defelsko, USA) was carried out to evaluate the effect of capsules incorporation on the adhesion strength of the coatings to the steel substrate according to ASTM D4541. In addition, the conical mandrel bending test (Sheen Instruments, UK) was performed on the coatings in accordance with the ASTM D522-Test Method A, to study the effect of adding capsules on the coatings elongation properties. The gloss test was also conducted on the coated metal plates according to ISO 2813 by a multiangle gloss meter (SH260C, Sheen Instruments, UK) to study the effect of capsules addition on the coatings' surface roughness.

2.3.3. Evaluation of Corrosion Properties and Healing Efficiency. Different types of corrosion evaluation techniques

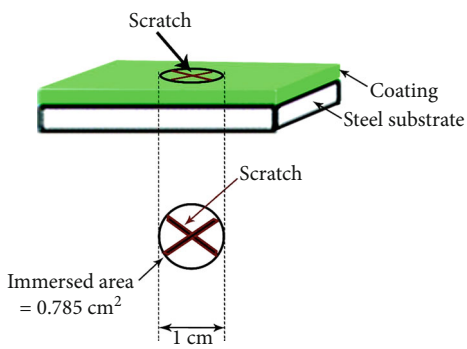

Figure 2: Scheme of the scratch dimensions in the coating to provoke the self-healing reaction.

were conducted to study the corrosion properties and assessing the self-healing performance of the prepared coatings. Potentiodynamic polarization (Tafel) and EIS tests were performed on the prepared coatings by an AMETEK Potentiostat/Galvanostat (PARSTAT 2273) to investigate their corrosion behavior and measuring the healing efficiency. An area of 0.785 cm^2 (circle with 1 cm diameter) from the coating's surface was isolated by insulating the remaining surface with beeswax and then scratched in X shape deep to the substrate metal (Figure 2) using a scalpel blade to trigger the healing process. Then, the scratched coatings were kept in the lab conditions for 7 days to allow for the release of healing agents and their plausible healing reactions. Then, the scratched coatings were immersed in a 3.5% NaCl solution for 14 days to stimulate seawater conditions.

A tri-electrode system (0.785 cm^2 circular contact area) including an aqueous saturated calomel electrode (SCE) as the reference electrode and a platinum rod as the counter electrode was used to do the experiments. Measurements were conducted at the open circuit potential (OCP). The frequency range was varied from 10^5 to 10^{-2} Hz at 10 points per decade sweeping frequency (logarithmic distribution) by a 10 mV sinusoidal potential difference. Tafel experiments were also carried out at a 1 mV s^{-1} scan rate from −1 V to +1 V versus OCP.

Salt spray accelerated corrosion test was also carried out to assess the protection ability of the healing system. All of the coated steel plates were scratched by a scalpel blade and left in the lab for 7 days for plausible healing reaction prior to testing. The salt spray test was conducted for 72 hours according to ASTM B117.

3. Results and Discussion

3.1. Chemical Structure of the Core-Shell Capsules. FT-IR analysis was used to characterize the chemical structure of prepared capsules and making sure that there is no reaction between the shell and core during the encapsulation process. Figure 3 shows the FT-IR spectra of SAN (neat shell polymer), neat epoxy resin (core), and prepared core-shell capsules derived through the emulsion electrospray method. As shown in this image, for neat shell material, the absorbance peak at 2235 cm^{-1} is related to C≡N in SAN, and the peaks at 3040 cm^{-1} and 2930 cm^{-1} are attributed to the stretching

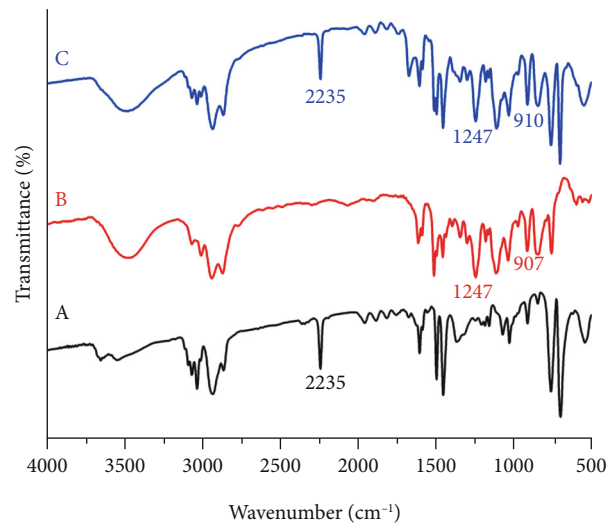

Figure 3: FT-IR spectra of (a) neat shell polymer (SAN), (b) neat epoxy resin, and (c) their corresponding core-shell capsules.

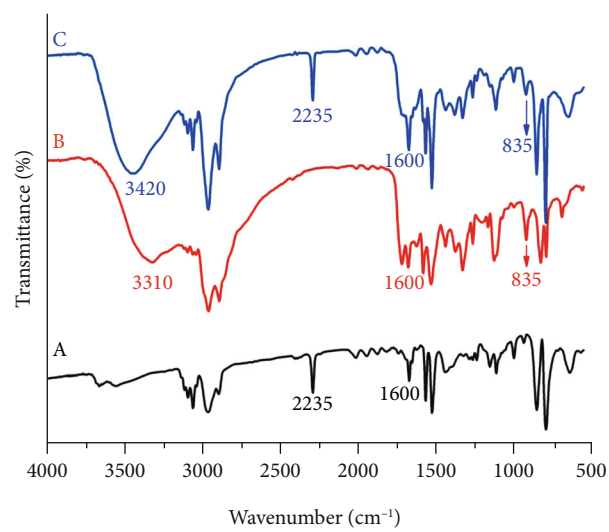

Figure 4: FT-IR spectra of (a) neat shell polymer (SAN), (b) neat curing agent (amine), and (c) their corresponding core-shell capsules.

vibrations of CH sp^2 and CH sp^3 [24]. In the neat epoxy spectrum, the absorbance peaks at 1247 cm^{-1} and 910 cm^{-1} correspond to C-O-C bond and epoxide groups, respectively [34]. The prepared core-shell capsules showed a broad absorption band at 3515 cm^{-1} associated with the O-H group [35]. The presence of all aforementioned peaks attributed to neat SAN copolymer and neat epoxy resin in the spectrum of prepared core-shell capsules confirmed that these two components did not react during the encapsulation process.

Figure 4 shows the FT-IR spectra of SAN (neat shell polymer), neat amine curing agent (core), and prepared core-shell capsules derived through the emulsion electrospray method. As shown in Figure 4, absorption bands at 3310, 1600, and 835 cm^{-1} correspond to stretching and bending vibrations of the amine group in the curing agent [34].

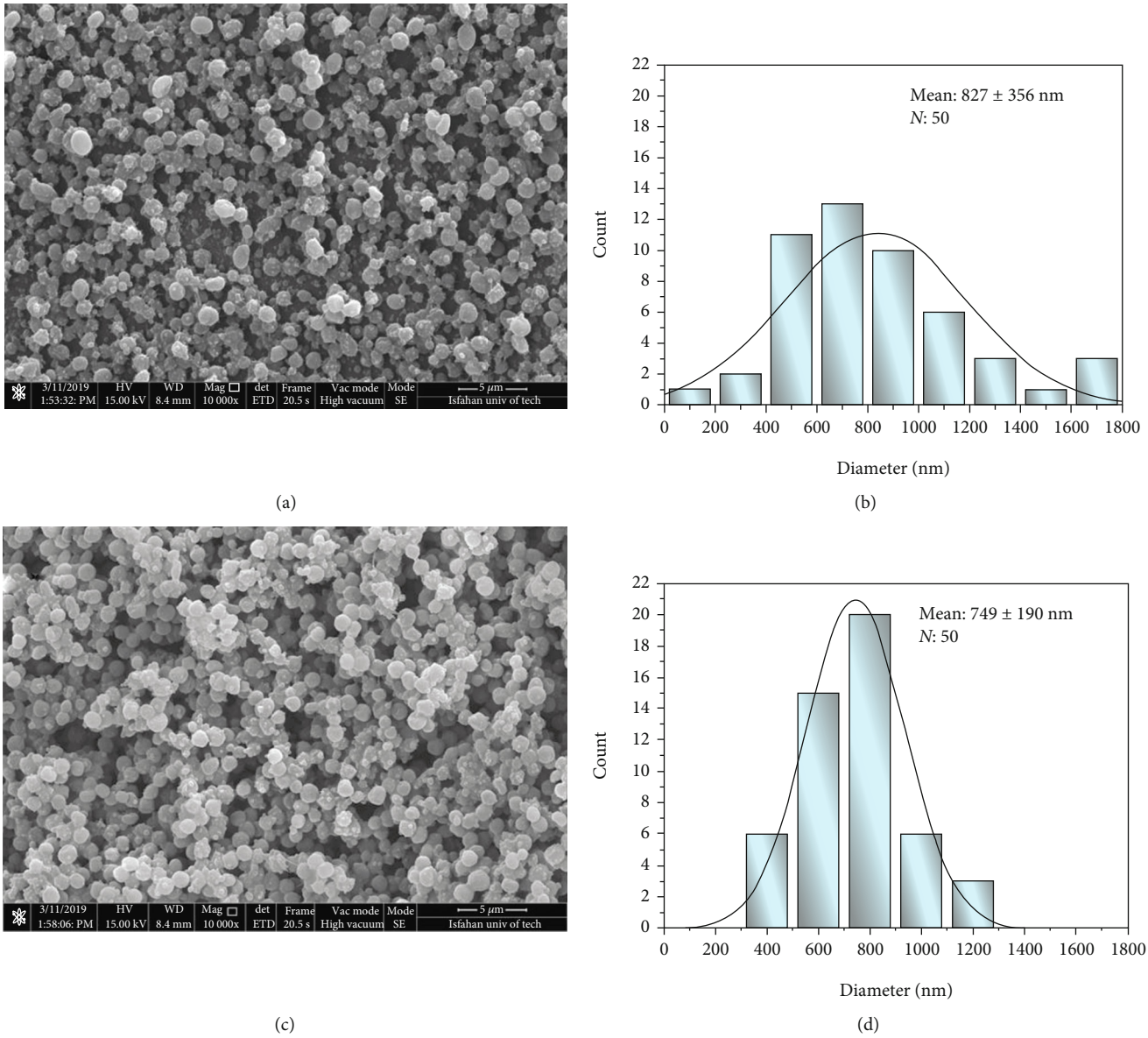

Figure 5: SEM images of the prepared MCs and their corresponding size distribution diagram for epoxy (a, b) and amine-based curing agent (c, d) cores.

Similarly, the spectrum of prepared core-shell capsules reveals that all absorbance peaks of neat SAN and neat curing agent are presented simultaneously. It can be discerned, the C≡N stretching vibration, at 2235 cm^{-1}, of SAN shell and the amine stretching vibration of the core, 3300-3450 cm^{-1}, are also present in the MCs, confirming that the core (amine) was successfully encapsulated in the shell polymer (polystyrene co-acrylonitrile) without any chemical reaction through the emulsion electrospray process [36].

3.2. Morphology and Size Distribution of the Prepared Capsules. Figure 5 shows the SEM images and size distribution of the prepared core-shell capsules. The mean particle size of the prepared capsules was calculated by 50 measurements using the Image J software. The mean particle size of the prepared capsules including epoxy resin and the amine core was calculated to be 827 ± 356 nm and 749 ± 190 nm, respectively. According to the images, spherical MCs with rough outer surfaces were prepared for both amine and epoxy healing agents in the electrospray process at the aforementioned optimum conditions.

3.3. Thermal Stability. TGA tests were performed to determine the thermal stability of prepared MCs [37]. Figure 6(a) shows TGA curves of neat shell polymer (SAN), neat epoxy resin, and epoxy-containing MCs. As shown in Figure 6(a), thermal degradation of pure SAN occurred at 400-450°C, which is related to the degradation of styrene groups. Also, the thermal degradation of the epoxy resin occurred in the temperature range of 200-500°C. The epoxy resin containing core-shell MCs showed a two-step degradation at 200-500°C. The first step is related to the degradation

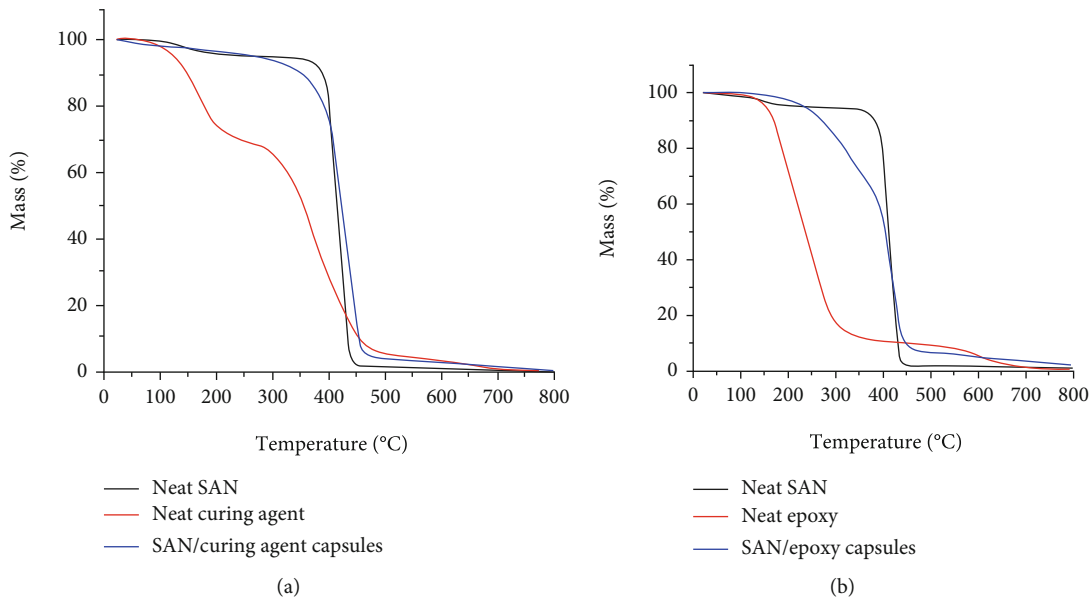

Figure 6: TGA thermograms of (a) neat SAN, neat epoxy resin, and epoxy-containing MCs (b) neat SAN, neat amine, and amine-containing MCs.

of epoxy resin, and the second step is related to the decomposition of SAN.

Similarly, Figure 6(b) shows the TGA curves of neat shell polymer (SAN), neat amine, and amine-containing MCs. Neat amine showed a two-stage degradation of around 100 to 200°C and 350 to 500°C. Amine-containing core-shell MCs showed the degradation of both amine core and SAN shell from 200 to 700°C which could be noted as a sign of successful core-encapsulation according to previous studies [38].

DSC tests were employed to study the possible curing reaction between the released healing agents from crushed prepared MCs. To provoke the MCs rapture and subsequent release of healing agents, amine and epoxy-containing MCs were mixed at 1 : 1 wt. ratio and then crushed by mortar and pestle. Then, the resulted mixture was immediately tested by DSC to monitor any plausible reactions. As reported in previous studies, the reaction between amine and epoxy is exothermic [34]; therefore, the exothermic peak in the DSC curve of crushed capsules can be evidence of a healing reaction. Figure 7 shows the DSC curve of the (a) neat shell MCs, (b) mixture of neat core materials (epoxy and amine), and (c) mixture of crushed epoxy and amine contained MCs. The endothermic peak in the range of 120-125°C for neat shell can be attributed to the glass transition temperature of SAN. The reaction between the epoxy resin and amine in the nonencapsulated form is shown inline chart (b) by an exothermic peak at 100°C. Moreover, the DSC curve for the mixture of epoxy resin and amine contained MCs (Figure 7(c)) which are artificially crushed prior to testing shows an exothermic peak at 104°C, which confirms the reaction between the relapsed healing agents after MC rapture.

Moreover, according to the extraction test results, the practical encapsulation yield was measured to be 73% and 67.8% for the epoxy and amine contained MCs, respectively. The results are summarized in Table 2.

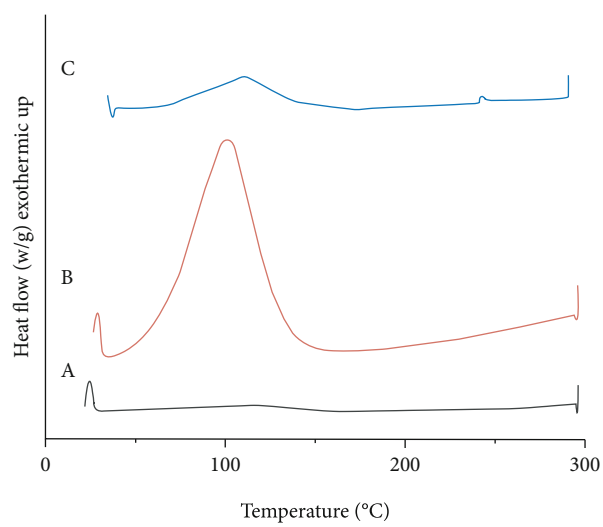

Figure 7: DSC curves of (a) neat SAN, (b) mixture of epoxy resin and amine in the nonencapsulated form, and (c) mixture of crushed epoxy resin and amine contained MCs.

Table 2: The determined results of core content and encapsulation yield.

MCs	W_{ex} (%)	W_{th} (%)	Encapsulation yield (%)
Epoxy-contained MCs	24.1	33.3	73
Amine-contained MCs	22.4	33.3	67.8

3.4. Pull-off Adhesion Test. A pull-off adhesion test was used to study the effect of incorporating MCs on the coatings' adhesion strength to the steel substrate. The obtained results are summarized in Table 3. According to the results, MC

Table 3: Adhesion strength results of the prepared coatings.

Sample	Adhesion strength (MPa)
CTRL	2.57 ± 0.03
Coating containing 1 wt% MCs	2.13 ± 0.06
Coating containing 5 wt% MCs	1.7 ± 0.06
Coating containing 10 wt% MCs	1.27 ± 0.06

Table 4: Elongation at break (%) of the prepared coatings.

Sample	Elongation at break (%)
CTRL	24.8
Coating containing 1 wt% MCs	19.4
Coating containing 5 wt% MCs	16.25
Coating containing 10 wt% MCs	15.1

incorporation into the coating decreased the adhesion strength. This loss was the lowest for the sample containing 1%w of MCs in comparison with the samples containing 5 and 10%w. The higher adhesion reduction in the samples with higher loading of MCs may be attributed to the agglomeration of MCs as well as their high surface area which will lead to more resin adsorption [39, 40].

3.5. Flexural Strength and Gloss Test of the Prepared Coatings. Conical mandrel bending tests were performed to study the effects of MCs addition on the flexibility and elongation of the prepared coatings. The results are presented as the coatings elongation at break (%) in Table 4. According to the results, the addition of MCs reduced the elongation of the prepared coatings, which can be attributed to the reduced adhesion of the coating to the substrate, as well as the defects presented by incorporating the MCs into the matrix and their agglomeration [39].

The gloss (%) measurement results of the coatings are summarized in Table 5. According to the results, the amount of gloss decreased by increasing the amount of MCs in the epoxy coatings. This loss is possibly attributed to the increased surface roughness caused by the addition and further agglomeration of MCs at higher concentrations [29].

3.6. Evaluation of Healing Reaction via Electrochemical Tests. A Potentiodynamic polarization test was employed to study the self-healing behavior of the scratched coatings after 14 days of immersion in a 3.5 wt% NaCl solution. The results for the CTRL and MC contained coatings are presented in Figure 8. It can be seen that the incorporation of MCs to the matrix moved the corrosion potential (Ecorr) to more positive potentials and decreased the corrosion current density (icorr) which confirms the higher corrosion resistance and slower corrosion rate of healed scratched coatings [29, 41, 42]. According to the results, the sample containing 1%wt MCs had the highest corrosion potential as well as the lowest corrosion current density among the samples confirming its superior performance against corrosion. This resistance is attributed to the reaction between the healing agents (epoxy resin and amine) leaking from the raptured MCs during crack formation [43]. In other words, the performance of the utilized healing system restrained the possibility of ions attack at the interface of metal coating by consequence chemical reactions between the released epoxy resin and polyamine hardener (self-healing reaction). Moreover, the results reveal that increasing the concentration of MCs from 1%wt decreased the corrosion resistance of the prepared coatings. As mentioned before, the lower performance of the samples containing 5% and 10% MCs may be due to MC agglomeration which will cause porosity in the matrix as well as their negative effect on the adhesion of the coating [44]. In addition, Figure 8 declares passive oxidation for sample CTRL (log $i \sim$ -4.5) around the surface of scratches which is designated to the constitution of oxidation layer and is detected by constant current despite increasing of potential while for samples containing MCs no passive oxidation observed which could refer to the performance of healing agents via self-healing processes.

The EIS measurements were also carried out on the scratched and immersed coatings to investigate their corrosion properties and healing efficiency [45]. Figure 9 represents the EIS results for these coatings after 14 days of immersion in a 3.5% NaCl solution. Regarding the Nyquist diagrams (Figure 9(a)), the diameter of the resulted semicircles is referred to the coating's corrosion resistance; thereby, the largest semicircle diameter is attributed to the highest resistance against corrosion and vice versa. On the other hand, the total impedance vs. frequency is presented in Bode modulus plots (Figure 9(b)) for better analyzing the results and evaluate the total system resistance (@ 10^{-2} Hz) including the coating's pore resistance and charge transfer resistance [46]. According to the results, a two-time constant electrical equivalent circuit model was also used to analyze the EIS data by the Z-view software (Figure 10) [47, 48]. Rs, CPEcoat, Rpore, Rct, CPEDL, and (n) stand for the electrolyte resistance, coating capacitance, pore resistance, charge transfer resistance, double-layer capacitance, and potential factor, respectively. Constant phase elements (CPE) were used in the electrical equivalent circuit model, owing to the capacitance behavior has some deviations from the pure capacitance in practice. The calculated parameters, according to the proposed circuit models, are presented in Table 6. The charge transfer resistance (Rct) was used in this research to compare the performance of the coatings since it is associated with the active area of the electrode and the rate at which Faradic processes occur at its interface. Both the higher intrinsic energy barrier of the charge transfer process and the smaller active area of the electrode which limit the electron transfer and corrosion reactions can be observed as higher Rct. In fact, as Rct is inversely proportional to the exposed active area of the electrode (according to the Ohm law), higher is the Rct, smaller is the area of the underneath metal exposed to the aggressive solution which might be driven by the self-healing reaction occurring in the coating's scratch [47, 49]. According to the calculated charge transfer resistance, adding 1% of MCs to the coating formulation increased the Rct dramatically, but it started to decrease by increasing the MC content from 1 wt%. These results were

Table 5: The results of the gloss measurement for prepared coatings.

Sample	20 degrees (GU)	60 degrees (GU)	85 degrees (GU)
CTRL	89.7 ± 2	102.5 ± 2	57.2 ± 2
Coating containing 1 wt% MCs	84.8 ± 2	100.7 ± 2	55.8 ± 2
Coating containing 5 wt% MCs	79.3 ± 3	96.4 ± 3	51.5 ± 2
Coating containing 10 wt% MCs	71.3 ± 2	91.2 ± 3	47.7 ± 3

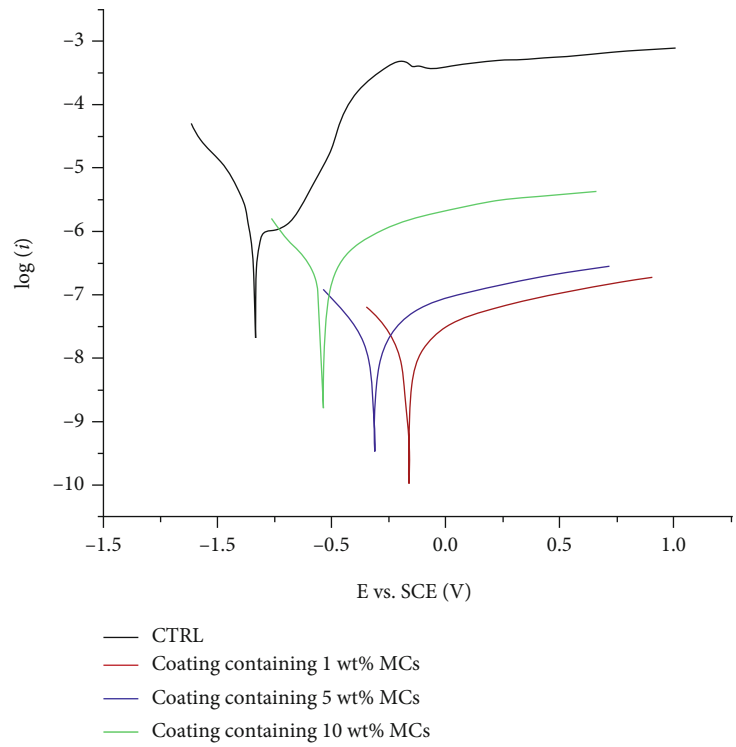

Figure 8: Potentiodynamic polarization curves for the scratched control and MC contained coatings after 14 days of immersion in 3.5% NaCl solution (0.785 cm^2 circular contact area).

consistent with previous corrosion resistance experiments. The results showed that the CTRL sample coating (without MCs) did not provide efficient corrosion protection and healing reaction against the electrolyte aggressive media. Although the sample with 10% MCs was qualified to support the self-healing reaction by releasing the healing agents in scratches, the probable agglomeration of MCs decreased the corrosion resistance by increasing the coating porosity.

The Bode modulus plots presented in Figure 9(b) prove the abovementioned explanations. It should be noted that the impedance modulus values at low frequencies are related to coating-metal interfaces. According to the results, the sample 1% presented the highest impedance value of $(z) = 3.7 \times 10^6$ at the lowest frequency which is clearly in good agreement with other evaluation techniques. The good compatibility between potentiodynamic polarization and EIS results confirmed that a 1 wt% MC incorporating was adequate to heal the crack and protect the substrate. By comparing the present results with the previous researches, it can be concluded that submicron scale capsules provide sufficient healing at lower amounts of capsule concentration which is one of the most important advantageous achieved in the current research. Bode phase results, presented in Figure 9(c), confirm the other corrosion evaluation results.

The self-healing efficiency (HE) of the samples was calculated by Eq. (3) [50].

$$\%\mathrm{HE} = \left(1 - \frac{\mathrm{Rct}_0}{\mathrm{Rct}}\right) \times 100. \quad (3)$$

Rct_0 and Rct are the charge transfer resistances calculated for the control and self-healing coatings, respectively. According to the results, the maximum HE was calculated to be 99% for the 1 wt % sample indicating its superior resistance against corrosion.

SEM was also used on the scratched and immersed coating containing 1 wt% of MCs to visually investigate the healing process [45, 51]. Figure 11 shows the micrographs of the scratched coating after healing. It can be seen a thin layer of

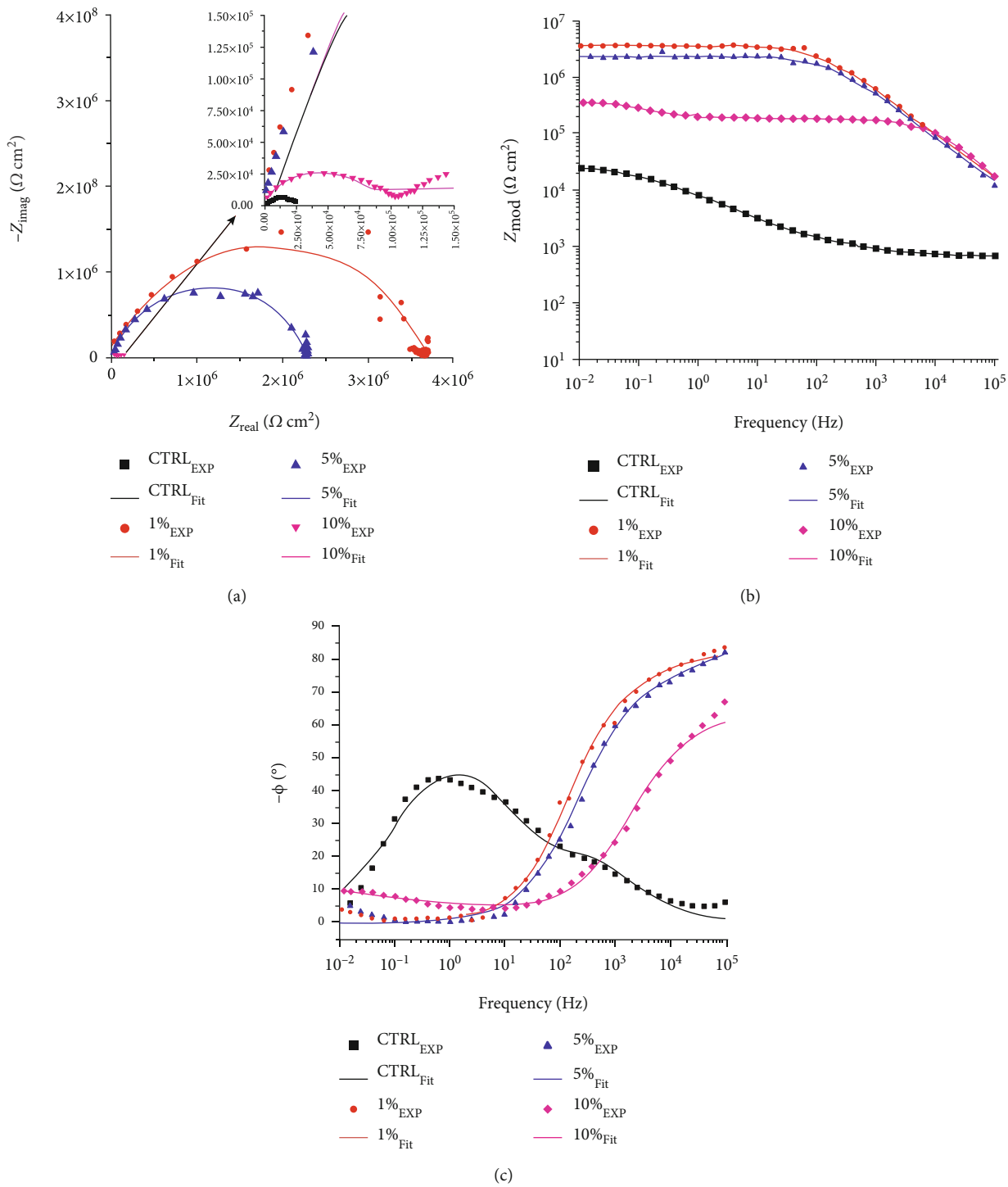

Figure 9: (a) Nyquist, (b) Bode modulus, and (c) Bode phase, plots of the scratched control and MC contained coatings after 14 days of immersion in 3.5% NaCl solution (0.785 cm^2 circular contact area).

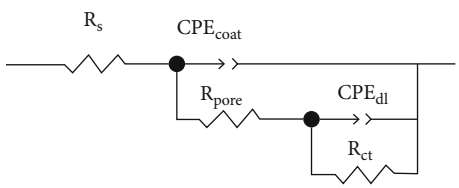

Figure 10: The incorporated electrical equivalent circuit model.

the healing polymer has been formed in the crack and covered the substrate. According to the SEM image, despite the fact that the released healing agents were not enough to fill the crack completely and provide full mechanical recovery, it sealed the crack with the aforementioned thin layer. This thin formed layer was enough to protect the substrate against the corrosive environment [52].

Table 6: The EIS parameters for the scratched control and MC containing coatings after being immersed in 3.5% NaCl solution for 14 days (0.785 cm^2 circular contact area).

Sample	Rs (Ω cm^2)	Qcoat ($sn.\Omega^{-1}.cm^{-2}$)	ncoat	Rpore (Ω cm^2)	Qdl ($sn.\Omega^{-1}.cm^{-2}$)	ndl	Rct (Ω cm^2)	Goodness of fit
CTRL	0.65*E*+03	2.46*E*-05	5.28*E*-01	1.33*E*+03	1.60*E*-05	5.77*E*-01	2.67*E*+04	2.12*E*-03
Coating containing 1 wt% MCs	1.51*E*+03	6.22*E*-09	7.34*E*-01	8.89*E*+03	8.53*E*-09	1.00*E*-01	3.79*E*+06	2.02*E*-03
Coating containing 5 wt% MCs	1.38*E*+03	6.04*E*-09	7.31*E*-01	1.03*E*+04	6.59*E*-09	1.00*E*-02	2.25*E*+06	1.87*E*-03
Coating containing 10 wt% MCs	0.25*E*+03	1.65*E*-08	7.01*E*-01	8.83*E*+04	1.85*E*-05	3.24*E*-01	2.00*E*+05	1.41*E*-03

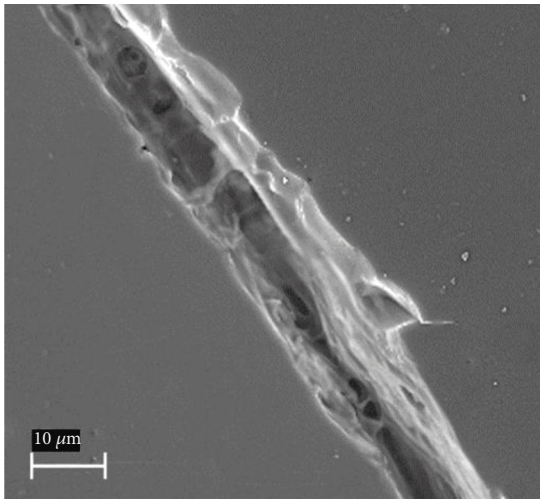

Figure 11: SEM micrographs of scratched and immersed coating containing 1 wt% of MCs after the healing process.

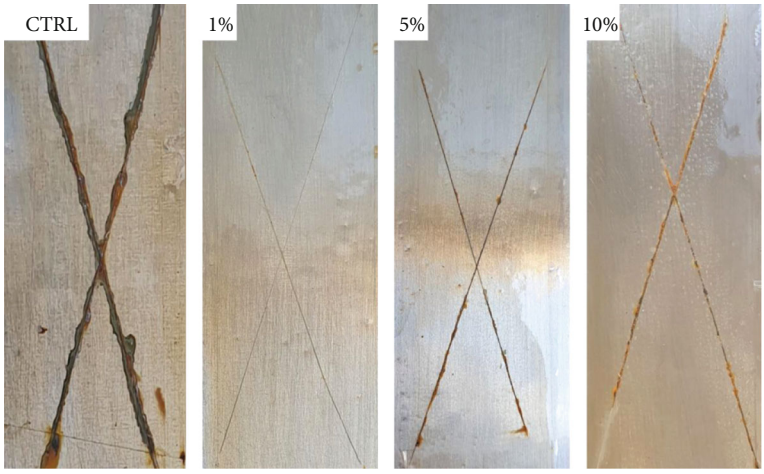

Figure 12: Samples after 72 hours of exposure in the salt spray chamber. The control coating and the coatings containing 1, 5, and 10 wt% MCs.

3.7. Salt Spray Corrosion Test. Figure 12 shows the images of scratched coatings after 72 hours in a salt spray chamber. According to the corrosion rust present in the scratch areas, MC contained coatings showed better corrosion resistance in comparison with the CTRL sample. This better performance can be referred to the MC rapture and subsequent self-healing reaction provoked by the scratch formation. As can be seen, 1% sample showed the best performance, but a loss in corrosion resistance was observed for the samples with higher MC content. This lower performance might be due to the negative effect of high MC content on the adhesion strength of the coating which facilitates the corrosive liquid penetration into the metal coating interface [29]. It should be noted that the higher amount of MCs will decrease the adhesion strength due to higher resin adsorption and lower interfacial contact between the substrate metal and the

matrix [24]. On the other hand, according to salt spray results for samples containing 5 and 10% MCs, some blisters can be observed on the unscratched area of 5% and 10% coatings as a result of NaCl solution penetration through the pores present in their matrix. The absence of these blisters on the 1% sample can be referred to the suitable dispersion of MCs in its matrix, while conversely excessive addition of MCs and their further agglomeration led to an increased porosity in the matrix of the 5% and 10% samples.

4. Conclusions

An extrinsic dual capsule self-healing system was developed for anticorrosion epoxy coatings. Core-shell MCs were prepared by using the emulsion electrospray method. Morphological investigations using SEM showed that core-shell spherical MCs can be prepared by setting the electrospray process parameters. In addition, the average particle size of the prepared capsules containing epoxy resin and the amine core were calculated to be 827 ± 356 nm and 749 ± 190 nm, respectively. The FT-IR spectroscopy results revealed no chemical reactions during the encapsulation process between the SAN shell and both of the core materials. Moreover, the extraction test results revealed that the practical encapsulation yield was obtained to be 73% and 67.8% for the epoxy and amine contained MCs, respectively. The corrosion evaluation test results on the scratched coatings showed the sample containing 1 wt % of core-shell MCs (1 : 1 by weight mixture of epoxy and amine-containing MCs) provided high corrosion resistance in comparison with the control sample and coatings containing higher capsule contents. The adhesion strength of the prepared coatings to the metal substrate decreased by increasing the amount of MCs, which could be due to the presence of MCs at the matrix-metal interface and reducing the effective contact area. The healing efficiency was calculated to be 99% for the coating containing 1% of MCs according to the EIS results.

Data Availability

The data used to support the findings of this study are available from the corresponding author upon request.

Conflicts of Interest

The authors declare that there is no conflict of interest regarding the publication of this paper.

References

[1] V. Amendola and M. Meneghetti, "Self-healing at the nanoscale," *Nanoscale*, vol. 1, no. 1, pp. 74–88, 2009.

[2] E. Alibakhshi, E. Ghasemi, M. Mahdavian, and B. Ramezanzadeh, "A comparative study on corrosion inhibitive effect of nitrate and phosphate intercalated Zn-Al- layered double hydroxides (LDHs) nanocontainers incorporated into a hybrid silane layer and their effect on cathodic delamination of epoxy topcoat," *Corrosion science*, vol. 115, pp. 159–174, 2017.

[3] E. Alibakhshi, E. Ghasemi, M. Mahdavian, B. Ramezanzadeh, and S. Farashi, "Active corrosion protection of Mg-Al- PO_4^{3-} LDH nanoparticle in silane primer coated with epoxy on mild steel," *Journal of the Taiwan Institute of Chemical Engineers*, vol. 75, pp. 248–262, 2017.

[4] M. Guo, W. Li, N. Han et al., "Novel dual-component microencapsulated hydrophobic amine and microencapsulated isocyanate used for self-healing anti-corrosion coating," *Polymers*, vol. 10, no. 3, p. 319, 2018.

[5] C. Zhang, H. Wang, and Q. Zhou, "Preparation and characterization of microcapsules based self-healing coatings containing epoxy ester as healing agent," *Progress in organic coatings*, vol. 125, pp. 403–410, 2018.

[6] E. K. Karaxi, I. A. Kartsonakis, and C. A. Charitidis, "Assessment of self-healing epoxy-based coatings containing microcapsules applied on hot dipped galvanized steel," *Frontiers in Materials*, vol. 6, p. 222, 2019.

[7] R. V. S. P. Sanka, B. Krishnakumar, Y. Leterrier, S. Pandey, S. Rana, and V. Michaud, "Soft self-healing Nanocomposites," *Frontiers in Materials*, vol. 6, p. 137, 2019.

[8] X. Yan, Y. Chang, and X. Qian, "Preparation and self-repairing properties of urea formaldehyde-coated epoxy resin microcapsules," *International Journal of Polymer Science*, vol. 2019, Article ID 7215783, 11 pages, 2019.

[9] R. Samiee, B. Ramezanzadeh, M. Mahdavian, and E. Alibakhshi, "Assessment of the smart self-healing corrosion protection properties of a water-base hybrid organo-silane film combined with non-toxic organic/inorganic environmentally friendly corrosion inhibitors on mild steel," *Journal of cleaner production*, vol. 220, pp. 340–356, 2019.

[10] G. Huyang, A. E. Debertin, and J. Sun, "Design and development of self-healing dental composites," *Materials & design*, vol. 94, pp. 295–302, 2016.

[11] W. Li, Z. Jiang, Z. Yang, and H. Yu, "Effective mechanical properties of self-healing cement matrices with microcapsules," *Materials & design*, vol. 95, pp. 422–430, 2016.

[12] F. Cotting, A. Koebsch, and I. V. Aoki, "Epoxy self-healing coating by encapsulated epoxy ester resin in poly (urea-formaldehyde-melamine) microcapsules," *Frontiers in Materials*, vol. 6, p. 314, 2019.

[13] R. Esmaeely Neisiany, M. S. Enayati, P. Sajkiewicz, Z. Pahlevanneshan, and S. Ramakrishna, "Insight into the current directions in functionalized nanocomposite hydrogels," *Frontiers in materials*, vol. 7, p. 25, 2020.

[14] Y. Hao, Y. Zhao, B. Li, L. Song, and Z. Guo, "Self-healing effect of loaded with benzotriazole for carbon steel," *Corrosion science*, vol. 163, article 108246, 2020.

[15] F. Sordo and V. Michaud, "Processing and damage recovery of intrinsic self-healing glass fiber reinforced composites," *Smart Materials and Structures*, vol. 25, no. 8, article 084012, 2016.

[16] Z. Wang, X. Lu, S. Sun, C. Yu, and H. Xia, "Preparation, characterization and properties of intrinsic self-healing elastomers," *Journal of Materials Chemistry B*, vol. 7, no. 32, pp. 4876–4926, 2019.

[17] Z. Wang, L. Scheres, H. Xia, and H. Zuilhof, "Developments and challenges in self-healing antifouling materials," *Advanced functional materials*, vol. 30, no. 26, article 1908098, 2020.

[18] S. K. Ghosh, *Self-Healing Materials: Fundamentals, Design Strategies, and Applications*, John Wiley & Sons, 2009.

[19] B. J. Blaiszik, S. L. Kramer, S. C. Olugebefola, J. S. Moore, N. R. Sottos, and S. R. White, "Self-healing polymers and composites," *Annual Review of Materials Research*, vol. 40, no. 1, pp. 179–211, 2010.

[20] R. Malekkhouyan, R. E. Neisiany, S. N. Khorasani, O. Das, F. Berto, and S. Ramakrishna, "The influence of size and healing content on the performance of extrinsic self-healing coatings," *Journal of Applied Polymer Science*, vol. 138, no. 10, p. 49964, 2021.

[21] R. Samiee, B. Ramezanzadeh, M. Mahdavian, E. Alibakhshi, and G. Bahlakeh, "Designing a non-hazardous nano-carrier based on graphene (III) for fabrication of the active/passive anti-corrosion coating," *Journal of hazardous materials*, vol. 398, article 123136, 2020.

[22] A. Habibiyan, B. Ramezanzadeh, M. Mahdavian, G. Bahlakeh, and M. Kasaeian, "Rational assembly of mussel-inspired polydopamine (PDA)-Zn (II) complex nanospheres on graphene oxide framework tailored for robust self-healing anti-corrosion coatings application," *Chemical Engineering Journal*, vol. 391, p. 123630, 2020.

[23] S. R. White, N. R. Sottos, P. H. Geubelle et al., "Autonomic healing of polymer composites," *Nature*, vol. 409, no. 6822, pp. 794–797, 2001.

[24] R. Malekkhouyan, S. Nouri Khorasani, R. Esmaeely Neisiany, R. Torkaman, S. M. Koochaki, and O. Das, "Preparation and characterization of electrosprayed nanocapsules containing coconut-oil-based alkyd resin for the fabrication of self-healing epoxy coatings," *Applied Sciences*, vol. 10, no. 9, p. 3171, 2020.

[25] R. E. Neisiany, M. S. Enayati, A. Kazemi-Beydokhti, O. Das, and S. Ramakrishna, "Multilayered bio-based electrospun membranes: a potential porous media for filtration applications," *Frontiers in Materials*, vol. 7, p. 67, 2020.

[26] J.-H. Park and P. V. Braun, "Coaxial electrospinning of self-healing coatings," *Advanced Materials*, vol. 22, no. 4, pp. 496–499, 2010.

[27] M. W. Lee, S. An, C. Lee, M. Liou, A. L. Yarin, and S. S. Yoon, "Self-healing transparent core–shell nanofiber coatings for anti-corrosive protection," *Journal of Materials Chemistry A*, vol. 2, no. 19, pp. 7045–7053, 2014.

[28] I. L. Hia, P. Pasbakhsh, E.-S. Chan, and S.-P. Chai, "Electrosprayed multi-core alginate microcapsules as novel self-healing containers," *Scientific Reports*, vol. 6, no. 1, p. 34674, 2016.

[29] M. S. Koochaki, S. Nouri Khorasani, R. Esmaeely Neisiany, A. Ashrafi, M. Magni, and S. P. Trasatti, "Facile strategy toward the development of a self-healing coating by electrospray method," *Materials Research Express*, vol. 6, no. 11, p. 116444, 2019.

[30] S. Ataei, A. Hassan, P. Azari et al., "Electrosprayed PMMA microcapsules containing green soybean oil-based acrylated epoxy and a thiol: a novel resin for smart self-healing coatings," *Smart Materials and Structures*, vol. 29, no. 8, article 085037, 2020.

[31] R. E. Neisiany, J. K. Y. Lee, S. N. Khorasani, and S. Ramakrishna, "Towards the development of self-healing carbon/epoxy composites with improved potential provided by efficient encapsulation of healing agents in core-shell nanofibers," *Polymer testing*, vol. 62, pp. 79–87, 2017.

[32] G. Zhao, H. Ni, S. Ren, and G. Fang, "Correlation between solubility parameters and properties of alkali lignin/pva composites," *Polymers*, vol. 10, no. 3, p. 290, 2018.

[33] E. Rezvani Ghomi, R. Esmaeely Neisiany, S. Nouri Khorasani et al., "Development of an epoxy self-healing coating through the incorporation of acrylic acid-co-acrylamide copolymeric gel," *Progress in organic coatings*, vol. 149, article 105948, 2020.

[34] R. E. Neisiany, S. N. Khorasani, J. Kong Yoong Lee, and S. Ramakrishna, "Encapsulation of epoxy and amine curing agent in PAN nanofibers by coaxial electrospinning for self-healing purposes," *RSC Advances*, vol. 6, no. 74, pp. 70056–70063, 2016.

[35] Q. Li, A. K. Mishra, N. H. Kim, T. Kuila, K.-t. Lau, and J. H. Lee, "Effects of processing conditions of poly(methylmethacrylate) encapsulated liquid curing agent on the properties of self-healing composites," *Composites Part B: Engineering*, vol. 49, pp. 6–15, 2013.

[36] T. J. Mitchell and M. W. Keller, "Coaxial electrospun encapsulation of epoxy for use in self-healing materials," *Polymer International*, vol. 62, no. 6, pp. 860–866, 2013.

[37] F. Ahangaran, A. H. Navarchian, M. Hayaty, and K. Esmailpour, "Effect of mixing mode and emulsifying agents on micro/nanoencapsulation of low viscosity self-healing agents in polymethyl methacrylate shell," *Smart Materials and Structures*, vol. 25, no. 9, article 095035, 2016.

[38] L. Vertuccio, S. Russo, M. Raimondo, K. Lafdi, and L. Guadagno, "Influence of carbon nanofillers on the curing kinetics of epoxy-amine resin," *RSC Advances*, vol. 5, no. 110, pp. 90437–90450, 2015.

[39] D. Raps, T. Hack, M. Kolb, M. Zheludkevich, and O. Nuyken, "Development of corrosion protection coatings for AA2024-T3 using micro-encapsulated inhibitors," Smart Coatings III. ACS Publications, 2010.

[40] S. Hatami Boura, M. Peikari, A. Ashrafi, and M. Samadzadeh, "Self-healing ability and adhesion strength of capsule embedded coatings–micro and nano sized capsules containing linseed oil," *Progress in Organic Coating*, vol. 75, no. 4, pp. 292–300, 2012.

[41] R. Samiee, B. Ramezanzadeh, M. Mahdavian, E. Alibakhshi, and G. Bahlakeh, "Graphene oxide nano-sheets loading with praseodymium cations: adsorption- desorption study, quantum mechanics calculations and dual active-barrier effect for smart coatings fabrication," *Journal of industrial and engineering chemistry*, vol. 78, pp. 143–154, 2019.

[42] S. U. Rahman and A. Atta Ogwu, "Corrosion and Mott-Schottky probe of chromium nitride coatings exposed to saline solution for engineering and biomedical applications," in *advances in medical and surgical engineering*, W. Ahmed, D. A. Phoenix, M. J. Jackson, and C. P. Charalambous, Eds., pp. 239–265, Academic press, 2020.

[43] S. Neuser, P. W. Chen, A. R. Studart, and V. Michaud, "Fracture toughness healing in epoxy containing both epoxy and amine loaded capsules," *Advanced Engineering Materials*, vol. 16, no. 5, pp. 581–587, 2014.

[44] X. Liu, H. Zhang, J. Wang, Z. Wang, and S. Wang, "Preparation of epoxy microcapsule based self-healing coatings and their behavior," *Surface and coatings technology*, vol. 206, no. 23, pp. 4976–4980, 2012.

[45] M. S. Koochaki, S. N. Khorasani, R. E. Neisiany, A. Ashrafi, S. P. Trasatti, and M. Magni, "A highly responsive healing agent for the autonomous repair of anti-corrosion coatings on wet surfaces. In operando assessment of the self-healing process," *Journal of Materials Science*, vol. 56, no. 2, pp. 1794–1813, 2021.

[46] E. Bakhshandeh, A. Jannesari, Z. Ranjbar, S. Sobhani, and M. R. Saeb, "Anti-corrosion hybrid coatings based on epoxy–silica nano-composites: toward relationship between the morphology and EIS data," *Progress in Organic Coatings*, vol. 77, no. 7, pp. 1169–1183, 2014.

[47] W. Wang, L. Xu, X. Li, Z. Lin, Y. Yang, and E. An, "Self-healing mechanisms of water triggered smart coating in seawater," *Journal of Materials Chemistry A*, vol. 2, no. 6, pp. 1914–1921, 2014.

[48] M. Hasanzadeh, M. Shahidi, and M. Kazemipour, "Application of EIS and EN techniques to investigate the self-healing ability of coatings based on microcapsules filled with linseed oil and CeO_2 nanoparticles," *Progress in Organic Coatings*, vol. 80, pp. 106–119, 2015.

[49] E. R. Ghomi, S. N. Khorasani, M. K. Kichi et al., "Synthesis and characterization of TiO2/acrylic acid-co-2-acrylamido-2-methyl propane sulfonic acid nanogel composite and investigation its self-healing performance in the epoxy coatings," *Colloid and Polymer Science*, vol. 298, no. 2, pp. 213–223, 2020.

[50] A. M. Atta, O. E. el-Azabawy, H. Ismail, and M. Hegazy, "Novel dispersed magnetite core-shell nanogel polymers as corrosion inhibitors for carbon steel in acidic medium," *Corrosion Science*, vol. 53, no. 5, pp. 1680–1689, 2011.

[51] H. Li, Y. Cui, Z. Li, Y. Zhu, and H. Wang, "Fabrication of microcapsules containing dual-functional tung oil and properties suitable for self-healing and self-lubricating coatings," *Progress in organic coatings*, vol. 115, pp. 164–171, 2018.

[52] S. H. Cho, H. M. Andersson, S. R. White, N. R. Sottos, and P. V. Braun, "Polydimethylsiloxane-based self-healing materials," *Advanced materials*, vol. 18, no. 8, pp. 997–1000, 2006.

Hindawi
International Journal of Polymer Science
Volume 2021, Article ID 6650499, 13 pages
https://doi.org/10.1155/2021/6650499

Research Article

Evaluation of Corrosion Protection of Self-Healing Coatings Containing Tung and Copaiba Oil Microcapsules

Nicolas Augusto Paolini,[1] Alexandre Gonçalves Cordeiro Neto,[1] Alana Cristine Pellanda,[1] Agne Roani de Carvalho Jorge,[1] Bryan de Barros Soares,[1] João Batista Floriano,[2] Marcos Antonio Coelho Berton,[1] Poornima Vijayan P,[3] and Sabu Thomas[4,5,6]

[1]*Senai Innovation Institute for Electrochemistry, Av. Comendador Franco 1341, Curitiba, Brazil*
[2]*Chemistry and Biology Department, Technological Federal University of Paraná, R. Dep. Heitor Alencar Furtado 5000, Curitiba, Brazil*
[3]*Sree Narayana College for Women (Affiliated to University of Kerala), 691001, Kollam, Kerala, India*
[4]*International and Inter University Centre for Nanoscience and Nanotechnology, Mahatma Gandhi University, Kottayam, Kerala, India*
[5]*School of Chemical Sciences, Mahatma Gandhi University, Kottayam, Kerala, India*
[6]*School of Energy Materials, Mahatma Gandhi University, Kottayam, Kerala, India*

Correspondence should be addressed to Alexandre Gonçalves Cordeiro Neto; alexandre.neto@sistemafiep.org.br

Received 22 November 2020; Revised 28 January 2021; Accepted 11 February 2021; Published 4 March 2021

Academic Editor: Zhi Li

The objective of the current research is to evaluate and compare the corrosion protection efficiency of the microcapsules containing tung oil and copaiba oil using stereoscopic images, electrochemical tests, open circuit potential (OCP), and polarization curves (Tafel analysis). Carbon steel plates were painted with three different coating systems: (a) a coating system with an automotive primer which served as the control, (b) a coating system with microcapsules containing 3% tung oil, and (c) a coating system with microcapsules containing 3% copaiba oil. A crosscut was performed using a scalpel on the coating surfaces to promote the release of the oils, and after drying, electrochemical cells were assembled using electrolyte 3% NaCl. From OCP analyses, it was verified that the coating system containing tung oil loaded microcapsules obtained more positive final values than the control system and the coating system containing copaiba oil loaded microcapsules. The stereoscope images corroborate the OCP results, and the polarization curve analyses also indicated that the microcapsules containing tung oil offer better corrosion protection than the other systems studied.

1. Introduction

The excessive corrosion of metals through structural degradation, chemical reactions, and wear deteriorates their performance and makes them unsuitable for use [1]. The failure of structures and equipment caused by corrosion generates a huge repair or replacement cost, in addition to safety issues. According to data between 2013 and 2015, global costs related to corrosion are estimated at US$ 2.5 trillion annually, representing about 3.4% of the world's gross domestic product (GDP) [2]. There are several ways to reduce corrosion and, consequently, increase the service life of those metals. The most common way is to apply organic coatings, which are paints or varnishes that create a barrier to corrosive processes in harsh environments [3]. However, this type of protection becomes ineffective during physical-chemical processes. For instance, ultraviolet and infrared radiations begin to alter the properties of the coating, making

it susceptible to failures, cracks, or microcracks. Once a crack develops on the coating, corrosive species such as water and salts in the corrosive medium may permeate through the coating until they reach the metallic substrate. Once corrosion has been triggered in the material, the coating would no longer be able to protect the damaged area [3]. One of the latest corrosion protection strategies is the use of self-regenerating coatings, called self-healing coatings, which can repair the damaged surface of the substrate without any human interference [4].

Examples of self-healing coatings include those containing complexes of polyelectrolytes, malleable polymers, and healing agents encapsulated in nano/microcapsules [5–7]. The capsules used to load the healing agents are either polymeric or inorganic in nature. Such micro- or nanocapsules are usually loaded with resins, corrosion inhibitors, and drying oils, which would be released by triggers such as pH changes, ion exchange processes, or mechanical damage [8, 9]. Figure 1 shows an illustration of a microcapsule, in which the material of interest is retained in the nucleus of the microcapsule (core) and protected by the structure of the wall (shell).

The use of natural oils as core materials in microcapsules is of great significance in the protection of metal surfaces from corrosion. In this case, the cure reaction occurs through the oxidation of double bonds in natural oils by atmospheric oxygen, making them a green alternative since they do not need any external catalyst to cure the oil [4, 10–13]. The popular natural oils used for this purpose are tung oil [14], linseed oils [15], neem oil [16], etc.

However, there is no report on a comparison between coatings containing microcapsules that encapsulated different natural oils, to assess which of the oils has a better effect against corrosion. The present study is aimed at comparing qualitatively the anticorrosion protection ability of two different drying oils (tung oil and copaiba oil) encapsulated in poly(urea-formaldehyde) (PUF) microcapsules in smart coatings. Intelligent coatings based on drying oil encapsulated in PUF microcapsules and a polyester-based automotive primer have been assessed for their self-healing efficiency using optical analysis and electrochemical tests.

2. Experimental

2.1. Materials and Synthesis of Microcapsules. Urea, ammonium chloride, sodium chloride, resorcinol, sodium dodecyl sulfate (SDS), sodium hydroxide, poly(ethylene-alt-maleic anhydride) (EMA) with a molecular weight of 100,000 to 500,000 $g \cdot mol^{-1}$, 1-octanol, tung oil, and copaiba oil were obtained from Sigma-Aldrich. Cyclohexane and isopropyl alcohol were obtained from Dynamics. Aqueous formaldehyde solution 37 wt% was obtained from J.T.Baker. Triton X-100 was obtained from Vetec. Polyurethane sealant adhesive was obtained from Solufix. Corrosion tests were carried out using 1020 carbon steel specimens with dimensions of $150 \times 100 \times 3$ mm (BS1) and an automotive primer based on polyester. All reagents were used as received without further purification.

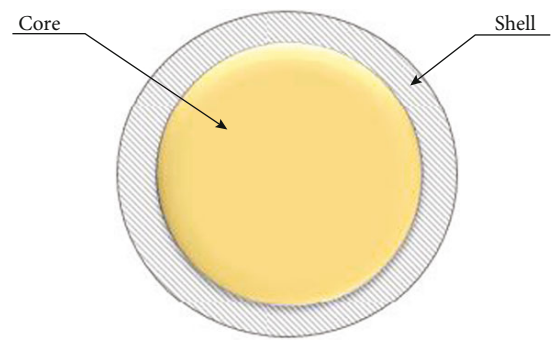

Figure 1: Illustration of a core-shell microcapsule.

Poly(urea-formaldehyde) microcapsules containing tung oil or copaiba oil have been prepared according to Neto et al. in 2020 [17]. Poly(urea-formaldehyde) microcapsules containing either tung oil or copaiba oil were synthesized via in situ polymerization in an oil-in-water emulsion. In a beaker, 5.0 g of urea, 0.5 g of ammonium chloride, and 0.5 g of resorcinol were dissolved in 250 mL of 0.5 wt% aqueous EMA solution under stirring and at room temperature ($20 \pm 2°C$). The pH of the mixture was adjusted to 3.5 using an aqueous sodium hydroxide solution ($1.0\ mol \cdot L^{-1}$). After pH adjustment, 0.2 g of SDS and 0.2 g of Triton X-100 were added to the solution. After the dissolution of the surfactants, the pH was adjusted to 3.5 again.

The reaction medium was placed in a thermostatic bath (Tecnal TE-184) and coupled to a mechanical stirrer (Fisatom 713D). To prevent foaming, approximately 5 drops of 1-octanol were added to the solution. Under stirring at a speed of 1200 rpm, 35.0 g of tung oil or copaiba oil was added dropwise to the solution to prepare the emulsion. The emulsion was kept under stirring for 30 minutes for stabilization. Then, 11.5 mL of aqueous formaldehyde solution (37%) was added, and the temperature was gradually increased to about $55 \pm 1°C$. Stirring was continued, and the reaction proceeded for 4 hours. The suspension containing the microcapsules was cooled to room temperature ($20 \pm 2°C$), and then the microcapsules were taken to the purification step. Empty microcapsules were synthesized based on the same procedure but without the addition of oil.

The microcapsule purification procedure was performed in two steps: washing and sieving, both in a batch. In the washing step, filtration was performed using a Büchner funnel under reduced pressure. The microcapsules were washed with 200 mL ultrapure water, 80 mL isopropyl alcohol, and 40 mL cyclohexane followed by drying at room temperature ($20 \pm 2°C$). In the second stage, the dried microcapsules were sieved on a sieve shaker using three 180, 90, and 60 μm aperture sieves.

2.2. Characterization of the Prepared Microcapsules. The synthesized microcapsules containing tung oil or copaiba oil were characterized by optical microscopy (OM) to evaluate parameters such as morphology, size regularity, and presence of residual material. Aliquots of the material were deposited on glass slides and were observed in a Zeiss Axio Imager Z2m Optical Microscope, using the image manipulation

software AxioVision SE64. Aliquots of crude material and microcapsules were analyzed after washing and filtration. The objective was used with a magnification of 5x. Scanning electron microscopy analyses were performed using a Hitachi microscope (TM3000) to evaluate the morphology of the microcapsules, in addition to structural integrity and roughness. Infrared analyses with Fourier transform were performed to confirm the encapsulation of the oils. The analyses were performed using the Bruker Vertex 70 with ATR mode in the range of 400 to 4000 cm^{-1}. Particle size analyses were performed by laser granulometry using the Microtrac model S3500 Bluewave granulometer and the Microtrac Bluewave software. The analysis was carried out in a wet method using deionized water as the medium, in which the microcapsules were previously submitted to the equipment's ultrasound process for 3 minutes for the dispersion of agglomerates.

2.3. Preparation of Coating Samples. Three different coating samples were prepared for analysis. The control coating was prepared by adding 50% of the polyester-based automotive primer to the 10% (*w*/*w*) xylene-based diluent according to the recommended proportion by the manufacturer. The mixture was maintained at 250 rpm on a mechanical stirrer (Fisatom 713D) for 10 min for complete homogenization of the paint.

For the other systems, before the incorporation of the diluent in the primer, microcapsules of tung oil or copaiba oil were added manually in the diluent, in a proportion of 3% (*w*/*w*), to later incorporate it into the primer. These systems were named MCOT and MCOC, respectively. After adding the diluent with microcapsules in the ink, the system was maintained at 250 rpm in a mechanical stirrer (Fisatom 713D) for 10 min for total homogenization.

The coatings were applied to blasted and degreased 1020 carbon steel substrates with dimensions of $150 \times 100 \times 3\ mm^3$ inside an automotive paint booth using a 1.8 spray gun (SATAjet 100 B), and two coats were applied, with a 5-minute interval between coats. After painting, the specimens remained inside the painting booth at a temperature of 25°C for approximately 24 hours for drying. They were then taken to a bench at room temperature (~ 20 ± 2°C), where they remained for an additional 72 hours until complete drying.

The morphology of the coating surface was viewed using a Zeiss SteREO Discovery V.12 stereoscope with the aid of image manipulation software AxioVision SE64. The brightness of the applied film was determined using a brightness meter (micro-TRI-gloss μ, BYK), analyzing a triplicate of samples, and they were classified according to their brightness range. The thickness of the dry applied coating was determined by the magnetic field attenuation method using the byko-test 8500 (BYK) equipment.

2.4. Analysis of Corrosion Resistance and Self-Healing Action. The study of corrosion protection and self-healing action was performed using an electrochemical cell consisting of three electrodes, made on the specimens, based on the contraption proposed by Cordeiro Neto et al. in 2020 [17]. For this, 40 mm long cut-off defects were caused using a scalpel blade over one region of each sample, and the samples remained at room temperature (20 ± 2°C) for 24 hours for healing. These defects were made to cause the microcapsules to rupture mechanically and to force the release of tung oil and copaiba oil, simulating a real microfissure situation under the microcapsule shell. In each defective region, a cylindrical compartment made of 17 cm^2 polypropylene was fixed, this being the active area of the working electrode. To make the electrochemical cell, 40 mL of electrolyte and 3.5 wt% NaCl were added. The reference electrode used was Ag/AgCl/KCl (sat.) (Metrohm), and the counter electrode served as the platinum net and the exposed sample served as the working electrode.

OCP tests were carried out up to 240 hours after the solution came into contact with the coating, and measurements were taken at 1, 2, 4, 8, 24, 48, 72, 144, 170, 192, 216, and 240 hours. The first hour of immersion was measured constantly. A Metrohm Multi Autolab Cabinet MAC80058 potentiostat was used for the experiment, and NOVA 1.11 software was used for data analysis.

For the analysis of polarization curves, a carbon steel plate was used as the working electrode (WE), the silver/silver chloride electrode with a saturated KCl (Ag/AgCl (KCl (sat.))) was used as the reference electrode (RE), and the platinum mesh was used as the counter electrode (CE). The analysis was carried out one hour after the solution came into contact with the coatings to stabilize the OCP. The scanning speed used was 1 mV/s. The measurements started at 100 mV below the OCP and ended at a fixed value of -0.2 mV. The Metrohm Multi Autolab Cabinet MAC80058 potentiostat was used for the experiment, and NOVA 1.11 software was used for data analysis.

3. Results and Discussions

3.1. Characterization of Tung Oil Encapsulated in Microcapsules. The optical microscopy image of the raw material is shown in Figure 2(a). The image analysis shows that there was formation of microcapsules and the presence of a considerable amount of a residual polymer. The purification process by filtration and washing with solvents is aimed at removing this residual material existing at the end of the synthesis, and the microscopy analysis was performed to find out if there was any degradation of the microcapsules after washing. Figure 2(b) shows the optical microscopy image of the purified material. It is observed that the microcapsules are spherical, presenting a wall with characteristic roughness. It is also noted that the amount of residual material decreased and that there was no deterioration of the microcapsules after washing.

Figure 3 shows the SEM images of the tung oil microcapsules. It is observed that the microcapsules have a spherical morphology. The wall of the synthesized microcapsules is uniform and appears to have a coating of adhered poly(urea-formaldehyde) nanoparticles that cause this characteristic roughness.

The FTIR analysis of the prepared microcapsules is intended to chemically confirm the encapsulation of tung

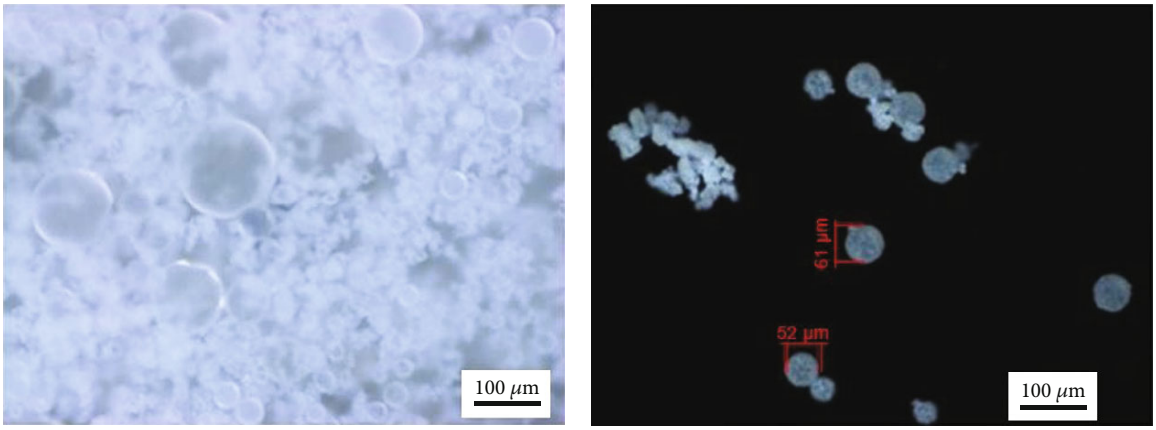

(a) (b)

Figure 2: Optical microscopy images of tung oil microcapsules (a) raw material and (b) microcapsules after washing.

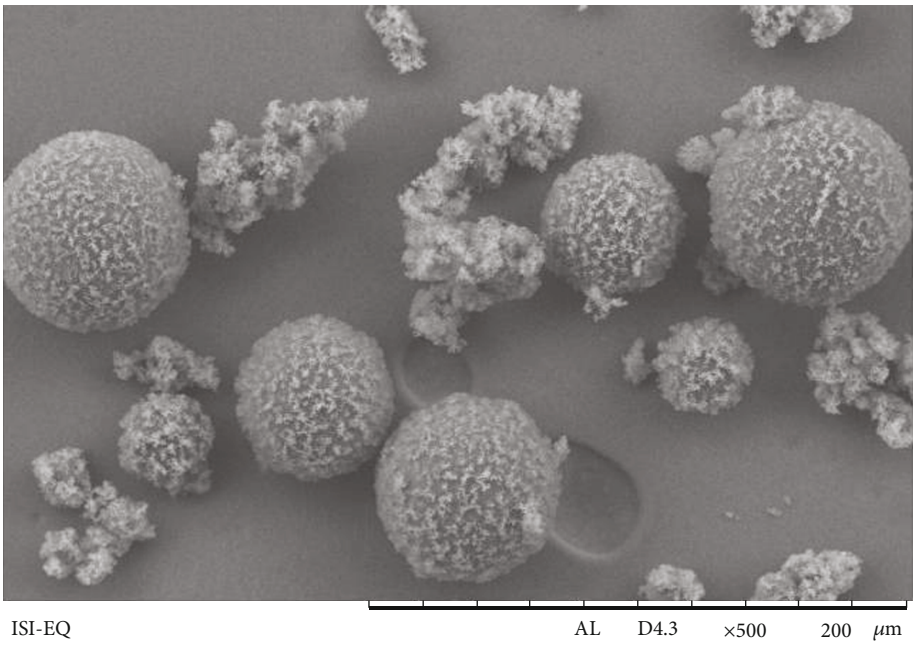

Figure 3: SEM images of tung oil microcapsules.

oil. To provide identification, the wall and core materials were analyzed separately, and the spectra were compared with the microcapsule spectrum. Figure 4 shows the FTIR spectra of microcapsules without tung oil, that is, only the wall material (PUF), the synthesized microcapsules (MCOT), and the core material (tung oil). The contribution of both the core material and the wall material in the spectrum of the microcapsules is evident. Upon analyzing the spectra of the wall material and MCOT, the presence of the bands between 3500 and 3200 cm^{-1}corresponding to the O-H absorption band, the presence of the band at 1631 cm^{-1}corresponding to the stretch C=O, and the presence of the band at 1552 cm^{-1} corresponding to the stretch N-H are detected [18]. Comparing the spectrum of the core material with the MCOT spectrum, there is also a correlation between the spectra, due to the presence of the band at 2924 cm^{-1}corresponding to the O-H stretch, the band at 2854 cm^{-1} corresponding to the C-H stretch, and the band at 1741 cm^{-1}corresponding to the C=O stretch [19, 20]. From these correlations, it is possible to confirm the satisfactory encapsulation of the tung oil by the wall material of PUF.

To verify the size distribution of the synthesized microcapsules, laser particle size analysis was carried out. Figure 5 shows that the average diameter of the microcapsules is 24.66 μm and that 95% of the microcapsules do not exceed the size of 50 μm.

3.2. Characterization of Copaiba Oil Encapsulated in Microcapsules. The optical microscopic images of the

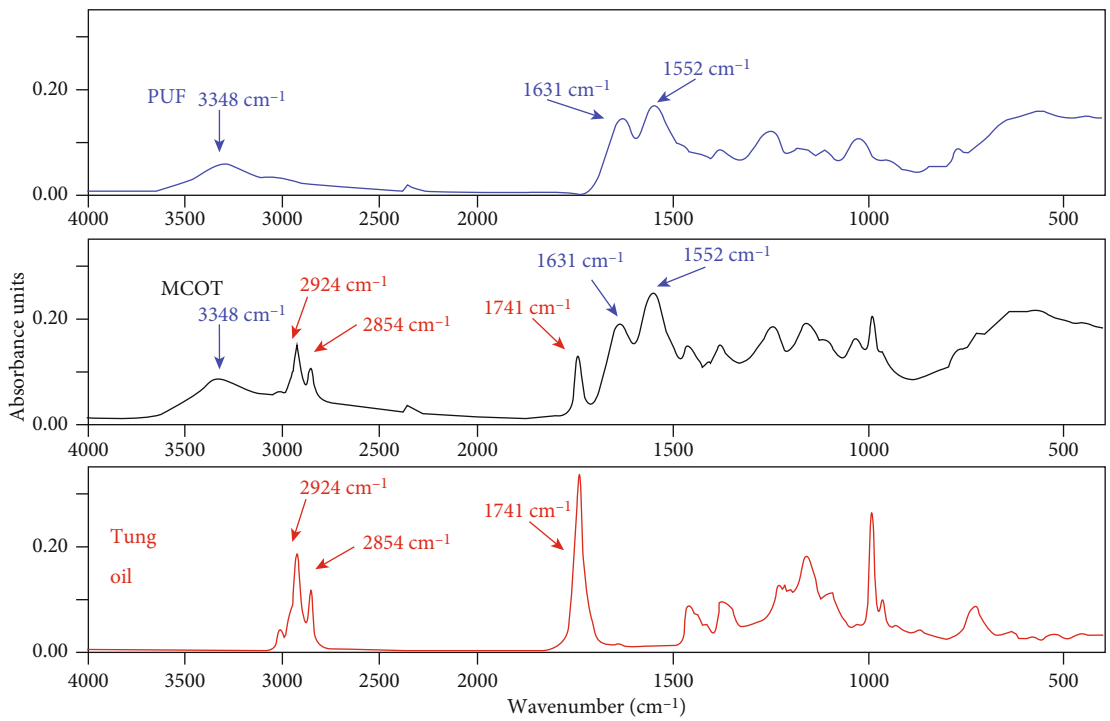

Figure 4: FTIR spectra of the wall material (poly(urea-formaldehyde)), the core material (tung oil), and the burst microcapsules.

Percentiles	
%Tile	Size (μm)
10.00	14.23
20.00	17.68
30.00	20.18
40.00	22.44
50.00	24.66
60.00	27.08
70.00	29.91
80.00	33.76
90.00	40.50
95.00	48.14

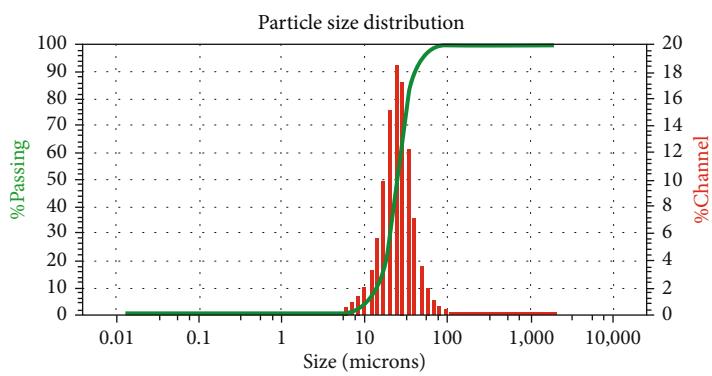

Figure 5: Particle size distribution chart for tung oil microcapsules.

synthesized copaiba oil encapsulated in microcapsules are shown in Figure 6. While Figure 6(a) shows the image of the raw material, Figure 6(b)shows the image of the purified material. It is observed that the microcapsules are spherical, having a wall with a roughness like that found in the tung oil encapsulated in microcapsules (Figure 2). After washing, there is an evident decrease in the residual material.

SEM analyses were performed to observe the morphology of the synthesized copaiba oil encapsulated in microcapsules (Figure 7). From the images, it is possible to verify that the microcapsules are spherical, with a morphology like that of tung oil encapsulated in microcapsules (Figure 3). The wall of the microcapsules appears to have a coating of adhered poly(urea-formaldehyde) nanoparticles. The existence of smaller agglomerated microcapsules is greater than that of the microcapsule sample containing encapsulated tung oil.

The morphological studies confirmed that the microcapsules are intact, without defects or holes, and have a morphology like that of tung oil encapsulated in microcapsules.

Figure 8 shows the FTIR spectra of the wall material (PUF), the synthesized microcapsules, and the core material (copaia oil). It is possible to observe the contribution of the spectra of both the core material and the wall material in the microcapsule spectrum; by initially analyzing only the spectra of the wall material and the MCOC, we see the correlation between the spectra due to the presence of the bands between 3500 and 3200 cm^{-1}corresponding to the OH absorption band, the band at 1631 cm^{-1}corresponding to the C=O stretch, and the band at 1552 cm^{-1} corresponding to the N-H stretch [18]. Comparing the spectrum of the core material with the MCOC spectrum, there is also a correlation between the spectra due to the presence of the band at

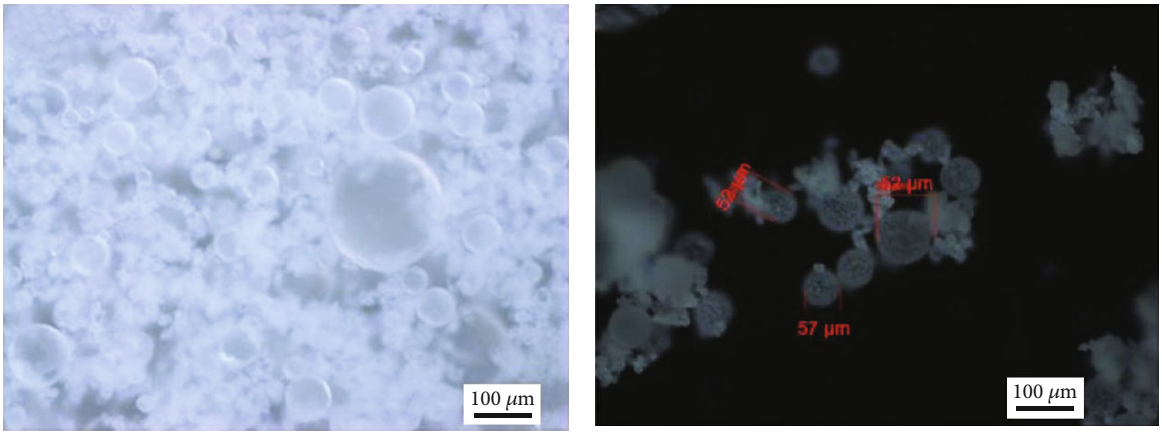

(a) (b)

Figure 6: Optical microscopy images of copaiba oil microcapsules (a) raw material and (b) the material after washing.

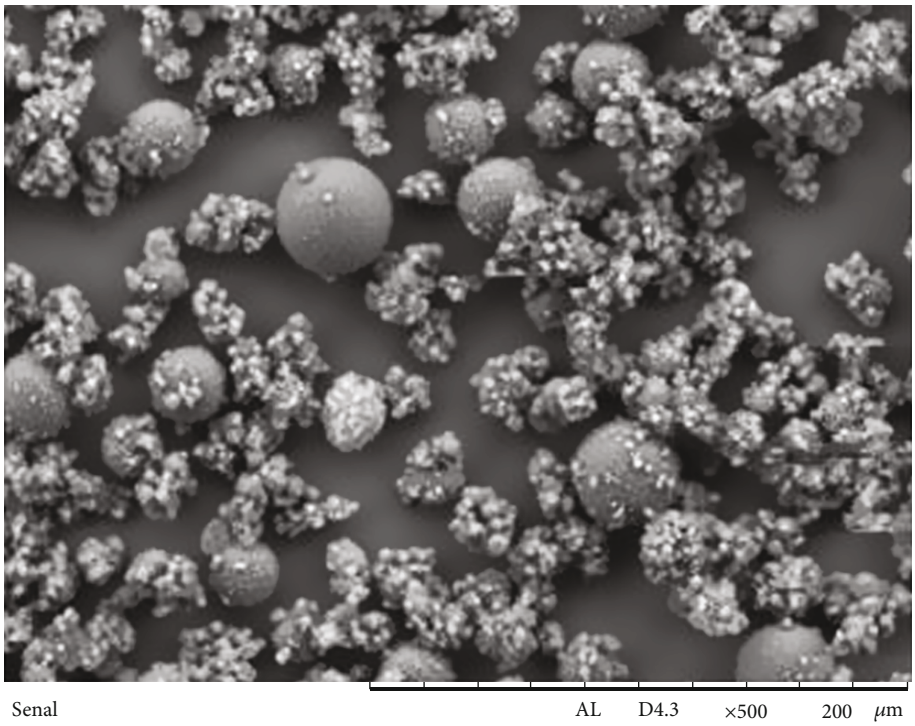

Figure 7: SEM images of copaiba oil microcapsules.

2925 cm^{-1}corresponding to the C-H stretch, the band at 1726 cm^{-1} corresponding to the C=O stretch, and the band at 1446 cm^{-1}corresponding to the C-O stretch [21]. Due to these correlations, it is confirmed that there was satisfactory encapsulation of the copaiba oil by the poly(urea-formaldehyde) wall material.

The results of the particle size laser analysis are shown in Figure 9. It is noticed that the average diameter of the microcapsules is close to the microcapsules of tung oil (22.50 μm against 24.66 μm). Also, it is observed that the maximum size of the microcapsules does not exceed the diameter of 50 μm.

3.3. Characterizations of the Coatings. Figure 10 shows the optical microscopy images of the surfaces of the control, MCOC, and MCOT plates. It is noted that the roughness of the plates containing microcapsules is greater than that of the control, and it is possible to observe that the roughness of the plate containing MCOT is greater than the plate containing MCOC, leading to the conclusion that the amount of capsules present in the ink is greater. This may indicate that the copaiba oil microcapsules have not completely resisted the paint application process, with the rupture of some microcapsules, or this may be related to a difference in the accommodation of the microcapsules in the coating.

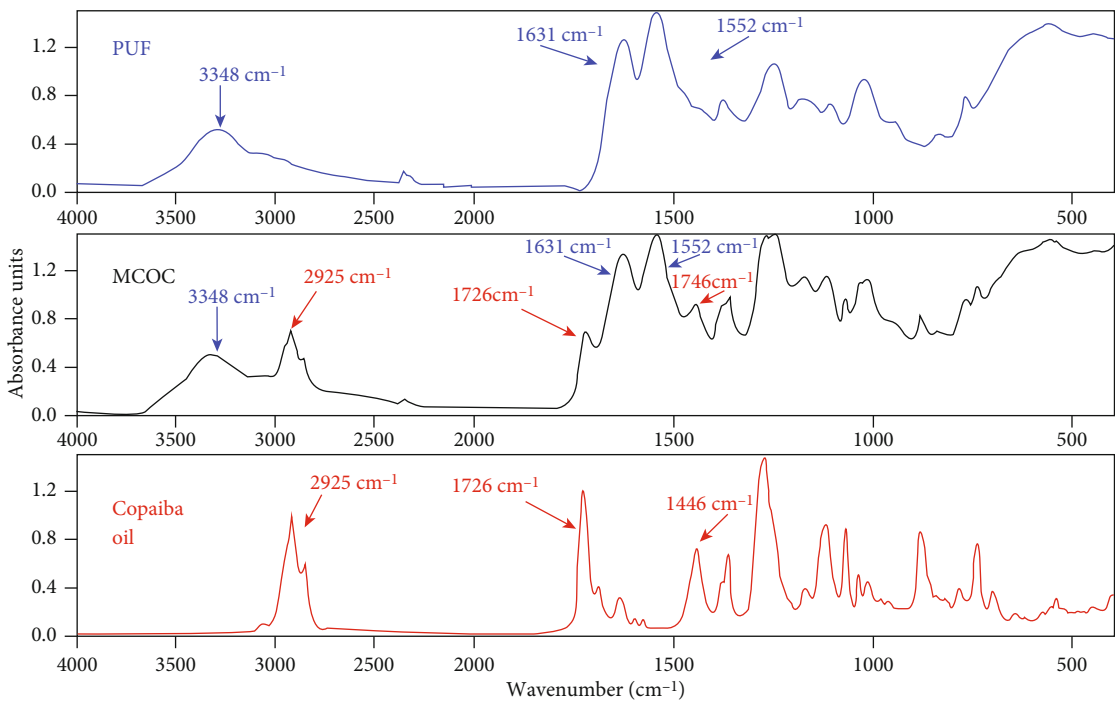

Figure 8: FTIR spectra of the wall material (poly(urea-formaldehyde), the core material (copaiba oil), and the burst microcapsules.

Percentiles	
%Tile	Size (μm)
10.00	15.62
20.00	17.63
30.00	19.28
40.00	20.84
50.00	22.50
60.00	24.39
70.00	26.76
80.00	30.23
90.00	36.91
95.00	45.26

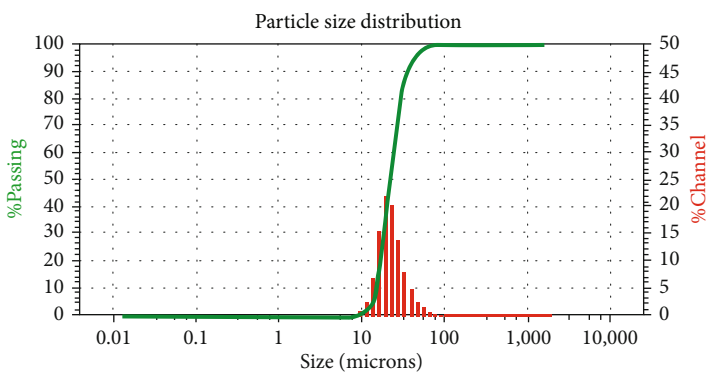

Figure 9: Particle size distribution chart of copaiba oil microcapsules.

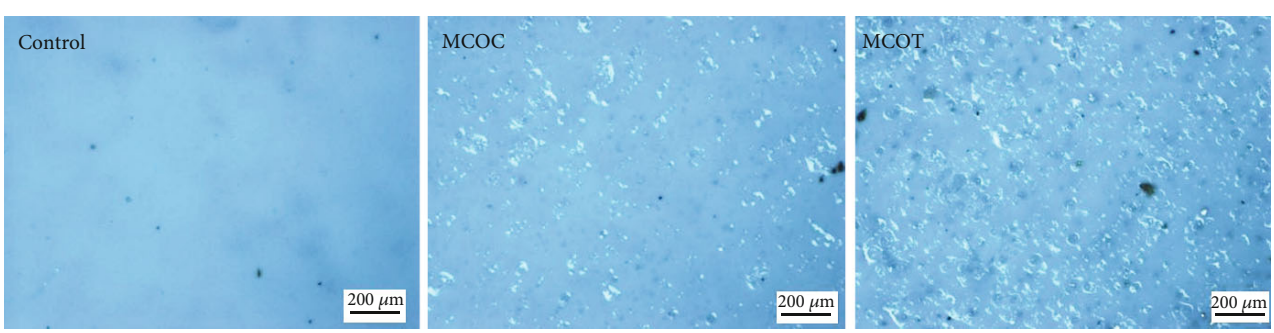

Figure 10: Optical microscopy images of the surfaces of the control, MCOC, and MCOT plates.

The copaiba microcapsules may have been positioned closer to the metallic substrate while the tung microcapsules may have been positioned at the top of the coating.

After curing the coating, thickness measurements were made to ensure that the applied coatings were of similar thickness. In all, ten measurements were made on the plates.

Table 1: Dry film thickness (ϕ) analysis of applied samples.

Sample	ϕ (μm)
Control	47 ± 3
MCOC	47 ± 2
MCOT	45 ± 3

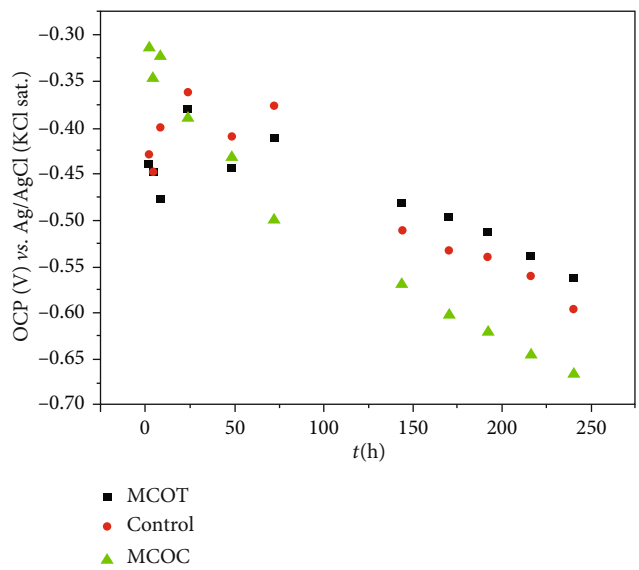

Figure 11: Compilation of OCP data up to 240 hours: the measurements on the plate that contain (a) 3% (m/m) MCOT are represented by the black squares, (b) those that contain 3% (m/m) MCOC are represented by green triangles, and (c) the measurements of the control plate are represented by red dots.

The average values of the thickness (ϕ), as well as the respective standard deviations, are shown in Table 1. It is possible to observe that all plates were coated with a dry film of close thickness, demonstrating that the application was carried out satisfactorily.

3.4. Electrochemical Characterization

3.4.1. Evaluation of Open Circuit Potential (OCP). Figure 11 shows the OCP graphs as a function of time (t) for the three systems studied. In the graph, the black points are the measurements of the plate containing 3% (w/w) of MCOT, the green points are those of the plate containing 3% (w/w) of MCOC, and the red points are those of the control plate.

As described by Souza et al. in 2005 [22], the OCP in metallic materials is equivalent to the corrosion potential, so when obtaining more positive values, it may indicate resistance to corrosion. In systems with self-healing properties obtained by incorporating microcapsules, when a defect occurs, there is a sudden decrease in potential and a gradual return to the passivation level indicating occurrence of self-regeneration [23]. For the tests, the coating was completely cured and, as in the systems where there was regeneration, this gradual return has already occurred, so the system will be more protected.

It can be observed that up to the period of 8 hours after adding the solution, the coating containing MCOC showed less negative OCP values than the control, and the coating containing MCOT showed itself to be more protective so far; however, over time, the MCOT coating shows more positive values among the three, indicating that it is the system with the best protection. In addition, over time, the MCOC system becomes worse than the control, with results far different from what was expected with the addition of microcapsules.

In order to understand this greater protection of the MCOC system at shorter times and the greater protection of the MCOT system at longer times, we compared the images of the damage done with the scalpel on the three plates at zero time and after drying in an oven. Figure 12 shows the optical microscopy images of the control, MCOC, and MCOT plates at both times.

It is possible to verify that in the control plate and in the plate containing MCOC, the risk was almost completely regenerated by the primer itself, demonstrating that the primer has a certain elasticity that was superior to the drying capacity of copaiba oil. This effect is different when compared to the plate containing MCOT, as it is observed that the damage was not covered by the paint, so it is believed that for this difference to occur, some component created a barrier preventing the return of the paint, and that component can precisely be the released tung oil that filled the risk. Due to the regeneration of the primer in the plate containing MCOC and adding this to the barrier effect that the addition of the microcapsules provides, it is believed that these combined factors caused the improvement of the observed OCP for the first hours of contact of the solution; however, over time the microcapsules proved inefficient.

For MCOTs, the system showed the best OCP values from 144 hours until the end of the experiment, showing the efficiency of tung oil in forming a protective barrier to inhibit the passage of the electrolyte and start the corrosive process and also in possibly stopping corrosive processes that start after several hours upon coming in contact with the electrolyte.

In order to compare the control system with systems containing microcapsules (in addition to the action of the drying oil), the action of inserting the microcapsules, which causes a barrier property to the primer (in addition to other influences that may cause it), should also be considered. Comparing with the control, the two systems containing microcapsules showed better results at different exposure times: the MCOC system for a few hours after contact with the solution and the MCOT system for longer times.

As a consideration when comparing the effect of the oils, the comparison should be made only between the two systems containing microcapsules, because this way it is possible to remove the influence of the insertion of the microcapsules. Analyzing the curves, it can be concluded that tung oil is more effective for the system, since in one application it is appreciated that the microcapsules improve the results for the entire exposure period, and not only for the first contact times.

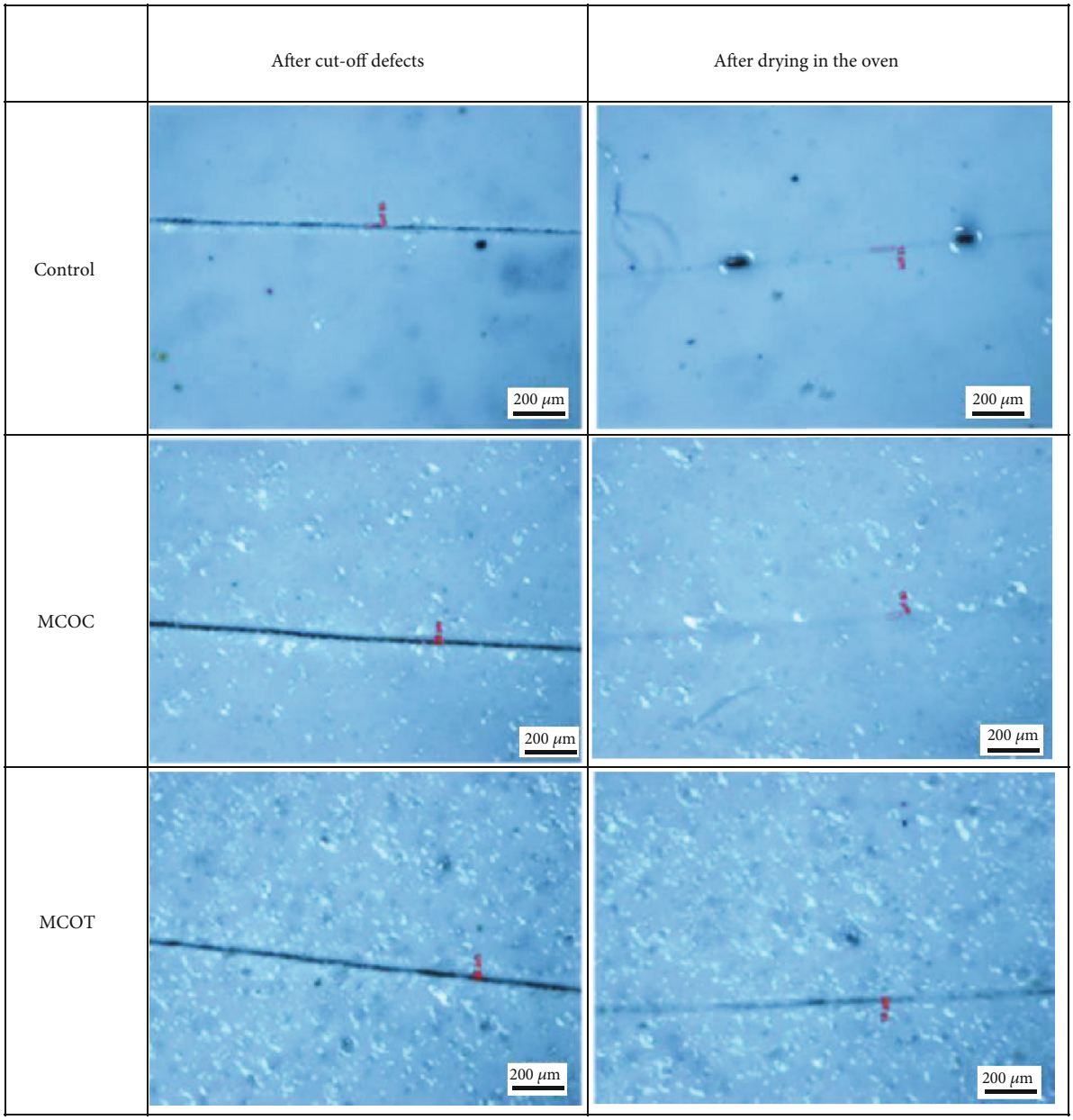

Figure 12: Optical microscopy images of the MCOC and MCOT control plates at the times after cutting and after the oven.

Parallel to the OCP analyses, stereoscopic images of the cells were taken at the same exposure times. The results of up to 24 hours of exposure to the electrolyte are shown in Figure 13, for the control, MCOC, and MCOT systems. It appears that the images of the three systems remain similar even up to 8 hours of exposure. After 4 more hours, there is a focus of corrosion, and after 8 more hours, the systems have two or three small points of corrosion. After 24 hours, a change is noted; the control system has two foci of corrosion at the ends of the site where the damage was done with the scalpel showing the formation of iron oxides. After 24 hours, the system containing MCOC presents several corrosion spots spread both in the delimitation of the risk and in other points, also presenting formation of iron oxides. In compensation, the system containing MCOT presents more contained spots of corrosion, and without the most intense coloring of the formed oxides.

The images of the control system, the MCOT system, and the MCOC system at the exposure times between 48 and 240 hours are shown in Figure 14. Between 48 and 72 hours of immersion, the differences between the systems become more highly expressed. The system containing MCOC has several points of corrosion along the cut and in other places of the cell. The control system also presents several points of corrosion, and the intensification of corrosion in the outbreaks presents at 24 hours, but visually, the corrosion is not as highly expressed when compared with the MCOC system. The MCOT system has the best resistance and corrosion inhibition for up to 72 hours, with more significant corrosion only at the center of the risk.

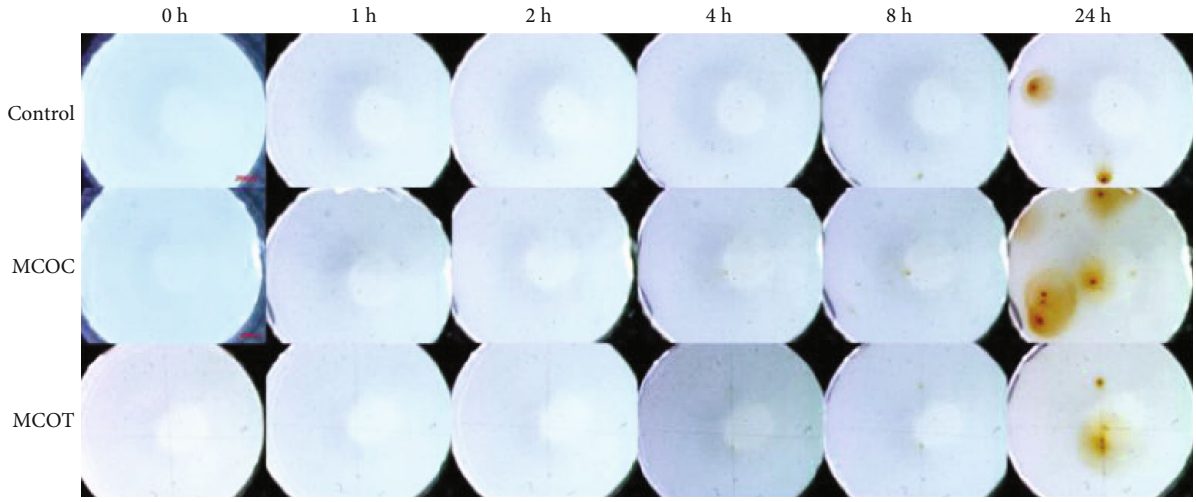

Figure 13: Control system, MCOT system, and MCOC system images up to 24 hours of electrolyte exposure.

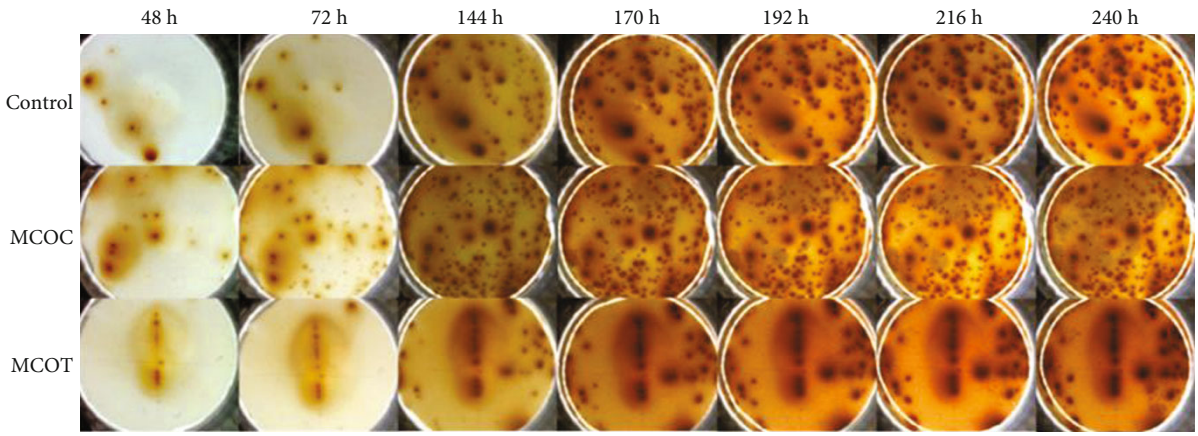

Figure 14: Control system, MCOT system, and MCOC system images with exposure hours between 48 and 240 hours.

After 144 hours, the MCOT system tends to have better protection than the other systems studied. The control system has numerous points of oxidation throughout the entire coating and in some points a very aggressive corrosion. In the MCOC system, in addition to the corrosion spots, it is observed that in some places there is a darkening of the primer, potentially indicating that the electrolyte has permeated the coating and is causing the coating to detach. This permeation of the electrolyte may be an explanation why the OCP of the MCOC system is the worst of the three systems in these analyses (144-240 hours), considering that in the other systems, this permeation is not observed. Finally, the MCOT system shows corrosion spots only along the scratch and at the ends of the cell.

From the images, it is concluded that for the visual analysis of electrochemical cells, the MCOT system is the most protective among those studied. This conclusion corroborates with the presented OCP data, in which the MCOT system had more positive OCP values than the others.

3.4.2. Polarization Curves. Figure 15 shows the polarization curves obtained from the control system, the MCOC system, and the MCOT system. Through the polarization curves, the two MCOC and MCOT systems have less corrosion potential than the control, with MCOT being the most positive, indicating that thermodynamically, these systems have less corrosion tendency [24]. After obtaining the polarization curves, the data were adjusted in the NOVA 1.11 software to obtain the data of corrosion potential (E_{corr}), corrosion current density (j_{corr}), corrosion rate (CR), and polarization resistance (R_p). The compilation of this data for unpainted, control, MCOT, and MCOC systems is shown in Table 2.

Analyzing initially the data of the column of the corrosion potential (E_{corr}), it is noticed that the values of the systems containing microcapsules are less negative than the control, with the MCOT system having the lowest negative value, and as explained previously, these less negative values indicate that thermodynamically, these systems are less prone to corrosion [24]. In the corrosion current density column (j_{corr}), there is a considerable drop in the value caused by the addition of the MCOC and MCOT in the coating, with both systems presenting practically identical values. This decrease in current density indicates greater corrosion inhibition efficiency, as described by Pontes et al. in 2016 [25].

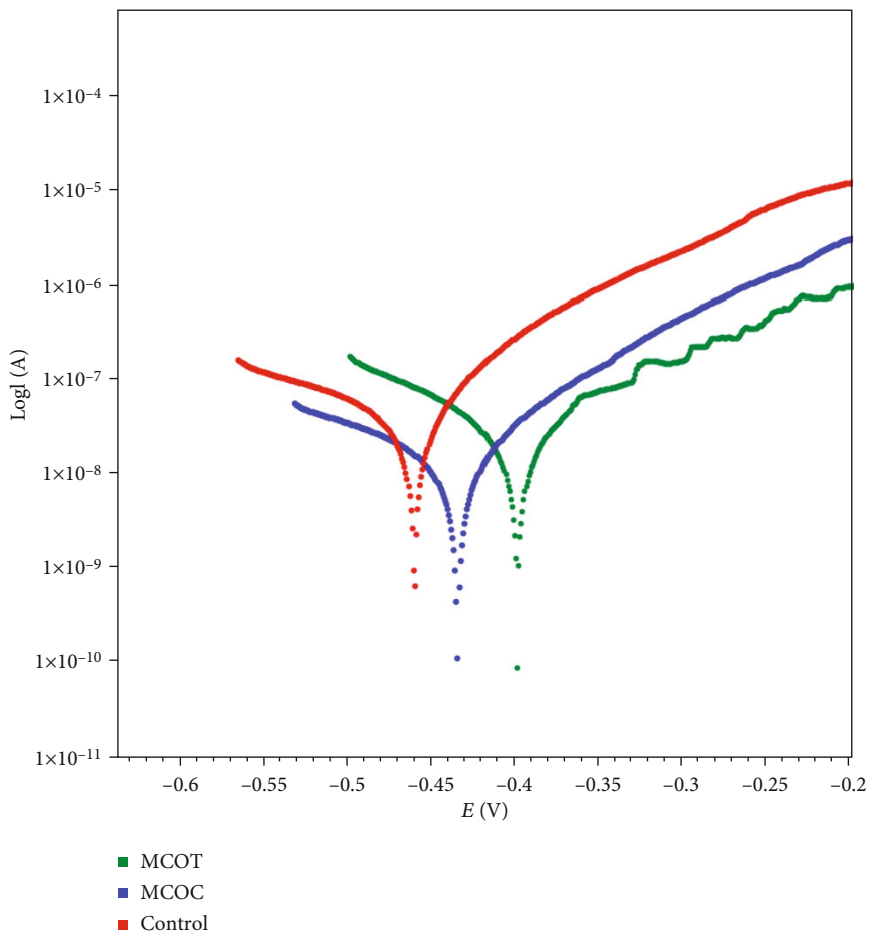

Figure 15: Polarization curves obtained from the control system (red), the MCOC system (dark blue), and the MCOT system (green).

Table 2: Corrosion potential data, corrosion current density, corrosion rate, and polarization resistance of the unpainted plate, the control, and the systems containing MCOC and MCOT.

Sample	E_{corr} (mV)	j_{corr} (μA/cm^2)	C_r (mm/year)	R_p (kΩ)
Control	-531	9.00×10^{-3}	1.05×10^{-4}	301
MCOC	-466	2.51×10^{-3}	3.16×10^{-5}	815
MCOT	-399	2.59×10^{-3}	3.01×10^{-5}	736

Analyzing the polarization resistance values, it is noted that in systems containing microcapsules, there was an increase in the polarization resistance, and since the polarization resistance can be defined as the resistance of the sample to oxidation during the application of an external potential, this indicates greater resistance to corrosion [26].

Finally, when analyzing the corrosion rate data, an industrial parameter of great importance, it is noted that the rate decreases considerably with the addition of microcapsules in the coating. Previous studies by Pontes et al. in 2016 [25] and by Okonkwo et al. in 2015 [27] demonstrated that, for an unprotected sheet exposed in marine environments, the corrosion rate can vary up to 0.6 mm/year. The value obtained by the control coating confirmed the effectiveness of adding a coating to protect carbon steel, and with the addition of microcapsules, the corrosion rate decreases to values of 3.0×10^{-5} mm/year, which is equivalent to 30 nm/year, confirming this protection when adding microcapsules.

From the data obtained by adjusting the polarization curves, it is possible to conclude that the addition of a coating on the carbon steel plate brings anticorrosion protection to the studied system; however, this protection is improved with the addition of microcapsules containing drying oils. When comparing the protection obtained with the addition of copaiba oil microcapsules with those of tung oil microcapsules, the two systems showed similar values in some data; however, in the general analysis, tung oil microcapsules proved to be the most protective against corrosion.

4. Conclusion

The present research successfully synthesized microcapsules that contained tung oil and copaiba oil. The morphological analysis concluded that the microcapsule wall is intact without any defects or holes. In addition, due to the polymerization efficiency of urea and formaldehyde monomers in the formation of the PUF, the wall polymer was proven and the formation of microcapsules was verified. By correlating the infrared spectra of the wall material and the core material

of the microcapsules, a satisfactory encapsulation of the oils by the wall material was confirmed. The granulometry analysis of the sieved microcapsules proved the efficiency of the screening process, obtaining final materials with similar average diameters (between 22 μm and 25 μm) and with 95% of the materials having a diameter less than 50 μm.

From the OCP results, it was concluded that tung oil was more effective for the system, as it presented the most positive values at the end of the experiment and consequently the best protection over the studied exposure time. Stereoscope images confirmed this conclusion, since over time, the MCOT system was the one that presented the best protection visually.

From the data of the polarization curves and the adjustments, it is concluded that when comparing the protection obtained by the addition of copaiba oil microcapsules with those of tung oil microcapsules, the two systems presented similar values in some data; however, when analyzing in general, tung oil microcapsules proved to be the most protective against corrosion for the studied system.

Although the results between MCOC and MCOT present close values, differentiating between 5 and 10%, it can be said that the resistance provided by the addition of MCOT was more highly expressed when carrying out a global assessment of the results such as OCP evaluation, visual analysis, and polarization curves.

This work focused on a qualitative and comparative analysis of the corrosion protection provided by the addition of the two microcapsules (MCOT and MCOC) in the studied system. To obtain a more concrete confirmation of the microcapsule's mechanisms of action, it is necessary to use nondestructive electrochemical techniques, as in the case of EIS. The group is carrying out work to investigate the mechanism behind the addition of MCOC and MCOT to various coatings.

Data Availability

The data used to support the findings of this study are available from the corresponding author upon request.

Conflicts of Interest

The authors declare that they have no conflicts of interest.

References

[1] V. Gentil, *Corrosão, LTC–Livros Técnicos e Científicos Editora S.A., 6a Ed.*, 2012.

[2] G. Koch, J. Varney, N. Thompson, O. Moghissi, M. Gould, and J. Payer, "International measures of prevention, application, and economics of corrosion technologies study," *NACE International*, 2016.

[3] M. L. Zheludkevich, S. K. Poznyak, L. M. Rodrigues et al., "Active protection coatings with layered double hydroxide nanocontainers of corrosion inhibitor," *Corrosion Science.*, vol. 52, no. 2, pp. 602–611, 2010.

[4] M. Behzadnasab, S. M. Mirabedini, M. Esfandeh, and R. R. Farnood, "Evaluation of corrosion performance of a self-healing epoxy-based coating containing linseed oil-filled microcapsules via electrochemical impedance spectroscopy," *Progress in Organic Coatings*, vol. 105, pp. 212–224, 2017.

[5] D. O. Grigoriev, K. Köhler, E. Skorb, D. G. Shchukin, and H. Möhwald, "Polyelectrolyte complexes as a "smart" depot for self-healing anticorrosion coatings," *Soft Matter*, vol. 5, no. 7, pp. 1426–1432, 2009.

[6] V. Sauvant-Moynot, S. Gonzalez, and J. Kittel, "Self-healing coatings: an alternative route for anticorrosion protection," *Progress in Organic Coatings*, vol. 63, no. 3, pp. 307–315, 2008.

[7] P. P. Vijayan and M. Al-Maadeed, "TiO_2 nanotubes and mesoporous silica as containers in self-healing epoxy coatings," *Scientific Reports*, vol. 6, no. 1, 2016.

[8] D. A. Leal, *Síntese E Caracterização De Microcápsulas Com Dupla-Função Contendo Óleo De Linhaça E Benzotriazol Para Aplicação Em Revestimentos Anticorrosivos Inteligentes*, Master's Theses. UFPR, Paraná Brazil, 2016.

[9] M. B. Restrepo, *Estudo Do Efeito De Autorreparação Nos Revestimentos Aditivados Com Microcápsulas Contendo Óleo De Linhaça. Master's Theses*, USP, São Paulo Brazil, 2012.

[10] H. Wang and Q. Zhou, "Evaluation and failure analysis of linseed oil encapsulated self-healing anticorrosive coating," *Progress in Organic Coatings*, vol. 118, pp. 108–115, 2018.

[11] G. Kurt Çömlekçi and S. Ulutan, "Encapsulation of linseed oil and linseed oil based alkyd resin by urea formaldehyde shell for self-healing systems," *Progress in Organic Coatings*, vol. 121, pp. 190–200, 2018.

[12] T. Nesterova, K. Dam-Johansen, and S. Kiil, "Synthesis of durable microcapsules for self-healing anticorrosive coatings: a comparison of selected methods," *Progress in Organic Coatings*, vol. 70, no. 4, pp. 342–352, 2011.

[13] P. Al-Maadeed, "Self-repairing composites for corrosion protection: a review on recent strategies and evaluation methods," *Materials*, vol. 12, no. 17, p. 2754, 2019.

[14] H. Li, Y. Cui, Z. Li, Y. Zhu, and H. Wang, "Fabrication of microcapsules containing dual-functional tung oil and properties suitable for self-healing and self-lubricating coatings," *Progress in Organic Coating*, vol. 115, pp. 164–171, 2018.

[15] H. Abdipour, M. Rezaei, and F. Abbasi, "Synthesis and characterization of high durable linseed oil-urea formaldehyde micro/nanocapsules and their self-healing behaviour in epoxy coating," *Progress in Organic Coating*, vol. 124, pp. 200–212, 2018.

[16] U. D. Bagale, S. H. Sonawane, B. A. Bhanvase, R. D. Kulkarni, and P. R. Gogate, "Green synthesis of nanocapsules for self-healing anticorrosion coating using ultrasound-assisted approach," *Green Processing and Synthesis*, vol. 7, no. 2, pp. 147–159, 2018.

[17] A. G. Cordeiro Neto, A. C. Pellanda, A. R. de Carvalho Jorge, J. B. Floriano, and M. A. Coelho Berton, "Preparation and evaluation of corrosion resistance of a self-healing alkyd coating based on microcapsules containing tung oil," *Progress in Organic Coatings*, vol. 147, p. 105874, 2020.

[18] C. Suryanarayana, K. C. Rao, and D. Kumar, "Preparation and characterization of microcapsules containing linseed oil and its use in self-healing coatings," *Progress in Organic Coatings*, vol. 63, no. 1, pp. 72–78, 2008.

[19] M. Samadzadeh, S. H. Boura, M. Peikari, A. Ashrafi, and M. Kasiriha, "Tung oil: an autonomous repairing agent for self-healing epoxy coatings," *Progress in Organic Coatings*, vol. 70, no. 4, pp. 383–387, 2011.

[20] K. Thanawala, A. S. Khanna, and R. K. Singh Raman, "Tung oil-urea formaldehyde microcapsules for anti-corrosive self-healing epoxy coatings," *Materials Science & Surface Engineering*, vol. 3, pp. 151–156, 2015.

[21] J. B. Almeida, *Desenvolvimento de Filme Magnético Utilizando Maguemita Recoberta com Óleo de Copaíba. Master's Theses*, UNB, Brasília Brazil, 2014.

[22] A. R. Souza, D. P. Mota, S. R. D. Paula, S. M. L. Agostinho, and M. M. P. Silva, "Medidas de potencial de circuito aberto: um experimento para o ensino de eletroquímica," in *Sociedade Brasileira de Química (SBQ)*, 32a Reunião Anual da Sociedade Brasileira de Química, 2009.

[23] E. M. Fayyad, M. A. Almaadeed, A. Jones, and A. M. Abdullah, "Evaluation techniques for the corrosion resistance of self-healing coatings," *Int. J. Electrochem Sci*, vol. 9, pp. 4989–5011, 2014.

[24] M. Kouhi, A. Mohebbi, and M. Mirzaei, "Evaluation of the corrosion inhibition effect of micro/nanocapsulated polymeric coatings: a comparative study by use of EIS and Tafel experiments and the area under the Bode plot," *Research on Chemical Intermediates*, vol. 39, no. 5, pp. 2049–2062, 2013.

[25] J. F. R. Pontes, E. V. Bendinelli, C. da Costa Amorim, M. M. de Sá, and A. P. Ordine, "Effect of corrosion inhibitor used in surface treatment on the anticorrosive performance of an epoxy paint system," *Materials Sciences and Application*, vol. 7, no. 10, pp. 593–609, 2016.

[26] S. Hiromoto, "Corrosion of metallic biomaterials," in *Metals for Biomedical Devices*, pp. 99–121, Woodhead Publishing Limited, 2010.

[27] P. C. Okonkwo, A. Shakoor, and A. M. A. Mohamed, "Environmental factors affecting corrosion of pipeline steel: a review," *Int. J. of Mechanical and Production Engineering Research and Development*, vol. 5, pp. 57–70, 2015.

Hindawi
International Journal of Polymer Science
Volume 2021, Article ID 6630194, 16 pages
https://doi.org/10.1155/2021/6630194

Research Article

Performance Evaluation of Layered Double Hydroxides Containing Benzotriazole and Nitrogen Oxides as Autonomic Protection Particles against Corrosion

Alana Cristine Pellanda,[1] Alexandre Gonçalves Cordeiro Neto,[1] Agne Roani de Carvalho Jorge,[1] Marcos Antonio Coelho Berton,[1] João Batista Floriano,[2] Sabu Thomas,[3,4,5] and Poornima Vijayan P[6]

[1]*SENAI Innovation Institute for Electrochemistry, Av. Comendador Franco 1341, Curitiba, Brazil*
[2]*Universidade Tecnológica Federal do Paraná, R. Deputado Heitor Alencar Furtado 5000, Curitiba-, Brazil*
[3]*International and Inter University Centre for Nanoscience and Nanotechnology, Mahatma Gandhi University, Kottayam, Kerala, India*
[4]*School of Chemical Sciences, Mahatma Gandhi University, Kottayam, Kerala, India*
[5]*School of Energy Materials, Mahatma Gandhi University, Kottayam, Kerala, India*
[6]*Sree Narayana College for Women (Affiliated to University of Kerala), 691001, Kollam, Kerala, India*

Correspondence should be addressed to Alana Cristine Pellanda; alana.pellanda@sistemafiep.org.br

Received 10 October 2020; Revised 28 January 2021; Accepted 10 February 2021; Published 3 March 2021

Academic Editor: Qinglin Wu

Layered double hydroxides (LDH) are lamellar structures with positively charged laminates and charge-compensating interlayer anions. The ion-exchange capacity of LDHs makes them as promising hosts for corrosion inhibitor anions with stimulus-responsive release and self-healing anticorrosion. In the current work, LDHs loaded with two different corrosion inhibitors (nitrogen oxides and benzotriazole) were evaluated for their ion-exchange capacity and autonomic protection against corrosion on carbon steel. Studies on nitrogen oxide-loaded LDH (NO_x-LDH) showed that nitrogen oxides were successfully intercalated in LDH structure, which were released in chloride media. Open Circuit Potential (OCP) results showed that NO_x-LDH extract shifted OCP to nobler values, indicating the protection of metal. For benzotriazole-loaded LDH (BTZ-LDH), the results indicated the presence of benzotriazole in the structure, but its release was not observed. OCP results showed no significant increase of carbon steel protection, corroborating with the conclusion that benzotriazole ions did not migrate to metal surface. Considering these results, the insertion of NO_x-LDH in an automotive primer was proceeded, under three different concentrations (0.2. 1.0, and 3.0%). Electrochemical impedance spectroscopy (EIS) showed that the more effective NO_x-LDH concentration on corrosion delay was 0.2%, which better balanced protection level conferred by LDH with a possible loss on effectiveness of coating due to increase in porosity.

1. Introduction

Layered double hydroxides (LDH), also known as 'anionic clays', consist of positively charged hydroxide layers (having structural similarity to brucite compounds) with anions and water molecules intercalated between these layers. LDH can be represented by the general formula $[M^{II}{}_{1-x}M^{III}{}_{x}(OH)_2]^{x+}(A^{n-})_{x/n}\cdot yH_2O$, where M^{II} and M^{III} are divalent and trivalent metal cations, respectively, and A^{n-} is the anion located between the layers to balance the positive charges. Distance between hydroxide layers allows the insertion of a wide range of anions, either organic or inorganic, with different sizes and on different spatial orientations [1–3].

LDH structures have been used in anticorrosion studies for the insertion of corrosion inhibitors in their anionic form

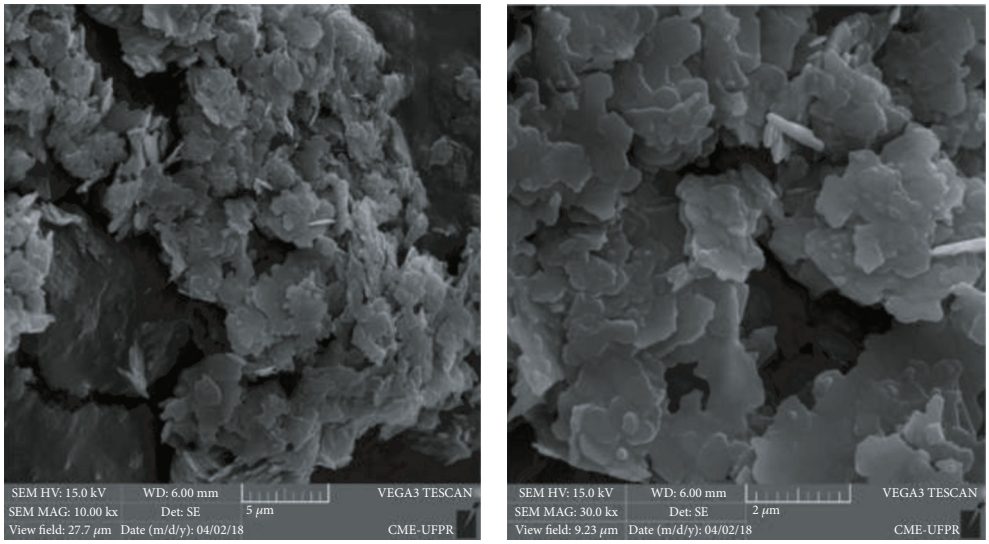

(a) (b)

Figure 1: SEM images of (a) NO_x-LDH and (b) BTZ-LDH.

between the layers [1, 4–6], so that the release of these anions is triggered by the anionic change with chloride ions of aggressive medium. Thus, LDH containing corrosion inhibitors play a double role on corrosion protection process: (a) promote controlled release of corrosion inhibitors, which may migrate to metal surface to create a passive barrier, and (b) accomplish corrosive ion trapping, decreasing the aggressiveness of medium [1, 7]. In this sense, LDH containing corrosion inhibitors may be inserted as additives on ordinary organic coatings, aiming to provide autonomic protection against extensive corrosion of metal substrates.

The current research work is aimed at evaluating and comparing the anticorrosion performance of two types of corrosion inhibitor-loaded Zn/Al-based LDH coating over carbon steel. Different from previous investigations, this research considered two different approaches to make LDH-based coating over carbon steel, LDH in extract form (acting as a kind of electrolyte 'pretreatment') and LDH dispersed in a coating matrix. The focus was on electrochemical discussions, which were supported by characterization data analysis.

2. Materials and Methods

Benzotriazole-loaded LDH (BTZ-LDH) and nitrogen oxide-loaded LDH (NO_x-LDH) were supplied from Smallmatek® and were analyzed by scanning electron microscopy (SEM) for structural evaluation of morphology, physical form, and agglomeration patterns. LDH powder samples were dispersed in ethanol using ultrasound bath for 1 h to distruct clusters of particles, and the morphological analysis was performed using a scanning electron microscope (TESCAN VEGA3 LMU equipment).

Chemical analysis of LDH samples was performed through fourier transform infrared spectroscopy (FTIR) technique using a Bruker OPTIK GmbH HTS-XT Vertex 70 equipment. In this procedure, KBr pastilles containing LDH aliquots were inserted on equipment's sample holder and spectra were acquired in an observation range of 4000 cm^{-1} to 400 cm^{-1} resolution of 4 cm^{-1} and 32 scans. As a complementary analysis to FTIR, the X-ray diffraction (XRD) technique was employed to investigate LDH's structure and calculate interlamellar distances. Diffractograms were collected in the range of 5° to 70°, with a step amplitude of 0.02° using a Bruker-AXS D2-Phaser equipment, operating at 30 kV and 10 mA with $CuK_{\alpha 1}$ ($\lambda = 1.540$ Å) radiation.

BTZ-LDH and NO_x-LDH were evaluated on their ability to prevent corrosion under two different approaches: after suspension in the electrolyte (LDH extracts) and dispersed on a coating matrix over the metal substrate.

For LDH extract preparation, the LDH powders were suspended in 3.5% NaCl solution under magnetic stirring for 24 h to promote ion exchange between inhibitor ions and chloride ions. After stirring, suspensions were centrifuged to obtain a clear solution containing released inhibitor ions and a precipitate composed by LDH containing entrapped chloride ions. The obtained precipitate was washed with ultrapure water and dried at 55°C to obtain a dry powder and analyzed through FTIR and XRD techniques employing the same procedures described above. The clarified solution obtained was employed as electrolyte on electrochemical tests. For OCP, PP (potentiostatic polarization) and EIS measurements, presanded and degreased carbon steel plates were employed. On each plate, three areas of 17 cm^2 were delimited to proceed measurements in triplicate and 40 mL of clarified solutions was added to each area. For electrochemical measurements, a three-electrode arrangement was employed, being the reference electrode Ag/AgCl (KCl saturated), the counter electrode a platinum wire, and the working electrode the carbon plate itself. Data was acquired using a PGSTAT302N Metrohm Autolab equipment. PP measurements were accomplished in the range of -200 mV to +400 mV vs. OCP with a scanning speed of 1 $mV \cdot s^{-1}$. EIS measurements were acquired in a frequency range of

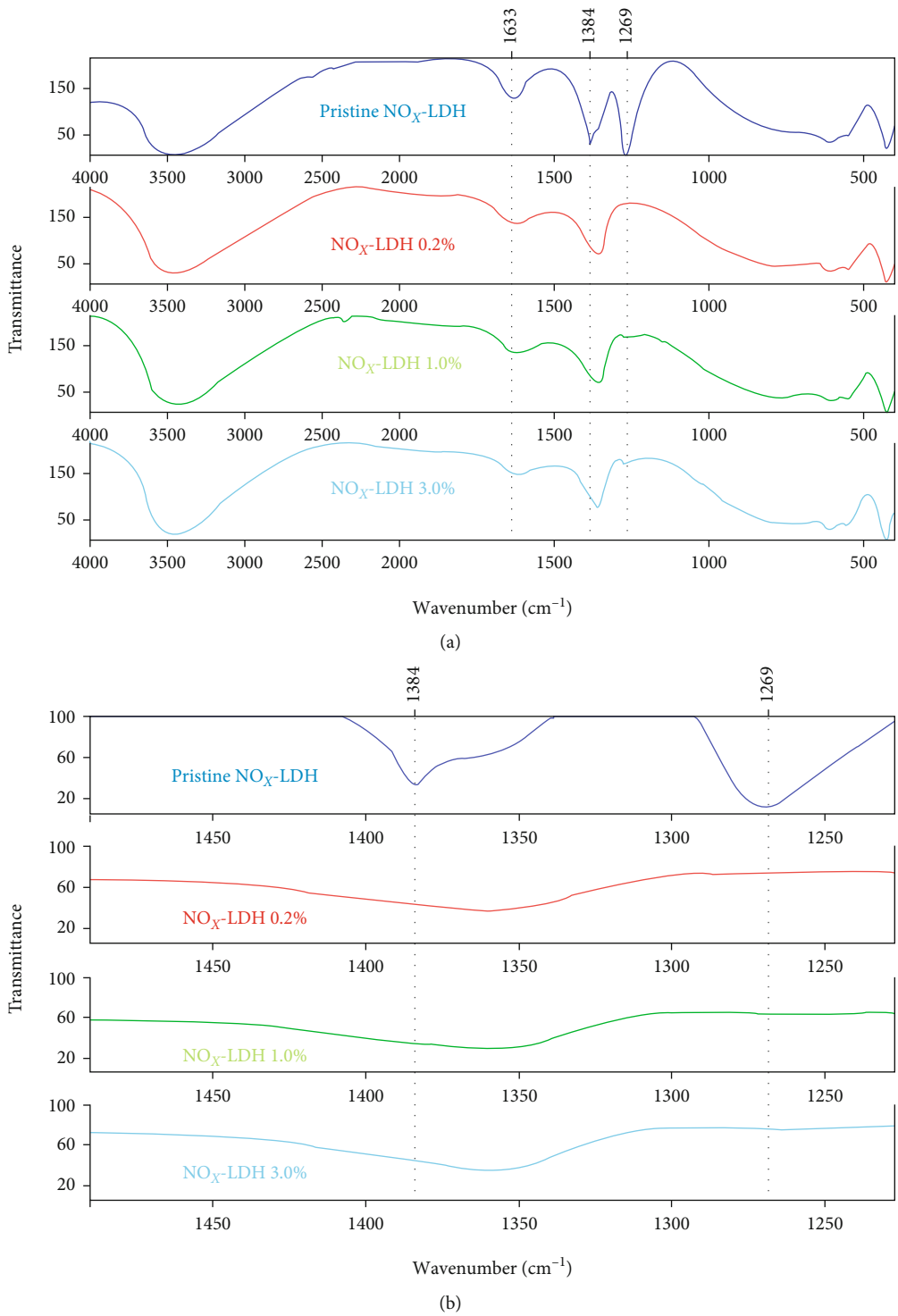

Figure 2: Comparative spectra of pristine NO_x-LDH before and after exposure to 3.5% NaCl (a) spectrum in full and (b) zoom in the 1384 cm^{-1} region.

10 kHz to 0.01 Hz with applied 10 mV sinusoidal perturbation and collecting 10 points per decade.

For developing LDH on a coating matrix, a polyester-based automotive primer coating was used as matrix. LDH powders were dispersed in primer under mechanical stirring on mass fraction of 0.2%, 1.0%, and 3.0%. The LDH-enriched primer was applied to presanded and degreased carbon steel 1020 plates using a professional paint gun so that the dried thickness was around 40 μm. After drying, three areas were delimited on each plate surface and 3.5% NaCl solution was added to proceed electrochemical measurements. Parameters and arrangement of electrochemical measurements were the same as described above, but in this case, EIS data was collected from 100 kHz to 0.01 Hz.

Table 1: Characteristic bands of FTIR spectrum obtained for NO_x-LDH.

Wavenumber (cm^{-1})	Assignment
3436	Water molecules adsorbed and hydroxyl groups [11]
1633	Bending stretching of water molecules [11]
1383	Nitrates symmetrical stretching [11]
1269	Nitrite ion deformation [12]
551	Zn/Al-OH translation [13]
426	Al-O condensed groups [13]

3. Results and Discussion

SEM analysis was performed in order to get insight into morphology and agglomeration patterns of LDH. Figure 1 shows SEM images obtained for both NO_x- and BTZ-loaded LDH. SEM analysis indicated that both types of LDH showed agglomeration patterns and plate-like morphology as reported previously [8–10].

FTIR analysis was made to verify characteristic bands of chemical bonds present on particle structure, as hydroxide groups, water molecules, Zn-Al bonds, and specific bonds of inhibitors. FTIR spectra of NO_x-LDH after exposure to 3.5% NaCl at 0.2, 1.0, and 3.0% w/v were acquired and are showed in Figure 2. Characteristic bands in pristine NO_x-LDH spectrum are given in Table 1. NO_x-LDH FTIR spectrum presented some band characteristics of structural components, such as water molecules and hydroxyl groups, besides nitrate and nitrite (inhibitors) characteristic bands, indicating the presence of these anions in the structure. Figure 2(a) shows that, after chloride exposure, the noticeable changes were the absence of bands at 1384 cm^{-1} and 1270 cm^{-1} which are characteristic of nitrate and nitrite ions, respectively. However, while observing the 1384 cm^{-1} region with more details (Figure 2(b)), it is possible to infer that this peak is composed by the overlap of two bands, one more defined (on the left of stretching) and a 'shoulder' on the right, initially of unknown nature. Figure 2(b) shows that, after chloride exposure, there is a significant decrease in the intensity of 1384 cm^{-1} stretching (and not its complete absence), maintaining the associated 'shoulder'. As 1384 cm^{-1} is associated with nitrate ions, it is inferred that such significant decrease on peak intensity was related to majority release of nitrate ions from the interlayer galleries, and the associated "shoulder" would be related to some structural portion of LDH, once it remained intact on spectrum. This result indicates that the nitrate and nitrite ions were initially located at the interlayer gallery and were satisfactorily released and exchanged with chloride ions after exposure.

Figure 3 shows the FTIR spectrum obtained for BTZ-LDH before and after exposure to 3.5% NaCl. The spectrum obtained for BTZ-LDH also allowed the identification of structural characteristic bands, such as water molecules and Zn/Al hydroxides (Table 2). The 1384 cm^{-1} stretching is marked in Table 2 with an asterisk due to the dubiety of its assignment: although it has been reported on literature that this stretching may be related to triazole ring deformation, it is also possible to relate it to the symmetrical stretching of nitrates, or even both contributions simultaneously. The presence of nitrate groups would be related to incomplete exchange of these ions (coming from the pristine LDH) for benzotriazole ions. Likewise, the peak on the region of 778 cm^{-1} highlighted on Table 2 with two asterisks may be interpreted in a first moment in two different ways: Al-OH (present in LDH structure) bond deformation or C-H bonds stretching from benzotriazole molecule. To settle this ambiguity, FTIR spectra of BTZ-LDH after chloride exposure were considered. The results obtained for the three investigated concentrations are shown in Figure 3. The peaks observed for the material after exposure to the medium rich in chlorides are the same as the pristine BTZ-LDH. Such as what was observed to NO_x-LDH, the exception is the stretching at 1384 cm^{-1} which presented the same kind of significant decrease in intensity after exposition when compared to the original LDH. This behavior is better seen in Figure 4(b) (zoom in the region of 1384 cm^{-1}). This result corroborates with the previous conclusion that the peak at 1384 cm^{-1} wwould be related to nitrate ions remaining in the interlayer galleries, which represents majority release and exchange of chloride ions. Despite this peak having been identified on isolated spectrum of benzotriazole (not shown), it is refused the hypothesis of this peak be related only to ring deformations which could be refused, since the other peaks attributed to benzotriazole remained in the spectrum after exposition, indicating that insertion of benzotriazole as interlayer anion was not achieved.

XRD measurements were done as a complementary technique to FTIR to characterize LDH structure to confirm the presence or absence of inhibitor anion intercalations in the interlayer gallery.

Basal space 'd' was calculated through XRD results employing Bragg's law (Equation (1)) [17].

$$d = \frac{\lambda}{2 \sin \theta}, \tag{1}$$

where λ is the wavelength of X-ray (1.54062 Å) and θ is the angle of the most intense peak. Other lattice parameters were obtained through relations established for rhombohedral systems, as shown on Figure 4. According to Figure 4, for systems with rhombohedral symmetry, the lattice parameter 'c' is the triple of basal space 'd'. The lattice parameter 'a' is related to lamella's atom nature, and its value can be estimated through the distance obtained by the (110) plane,

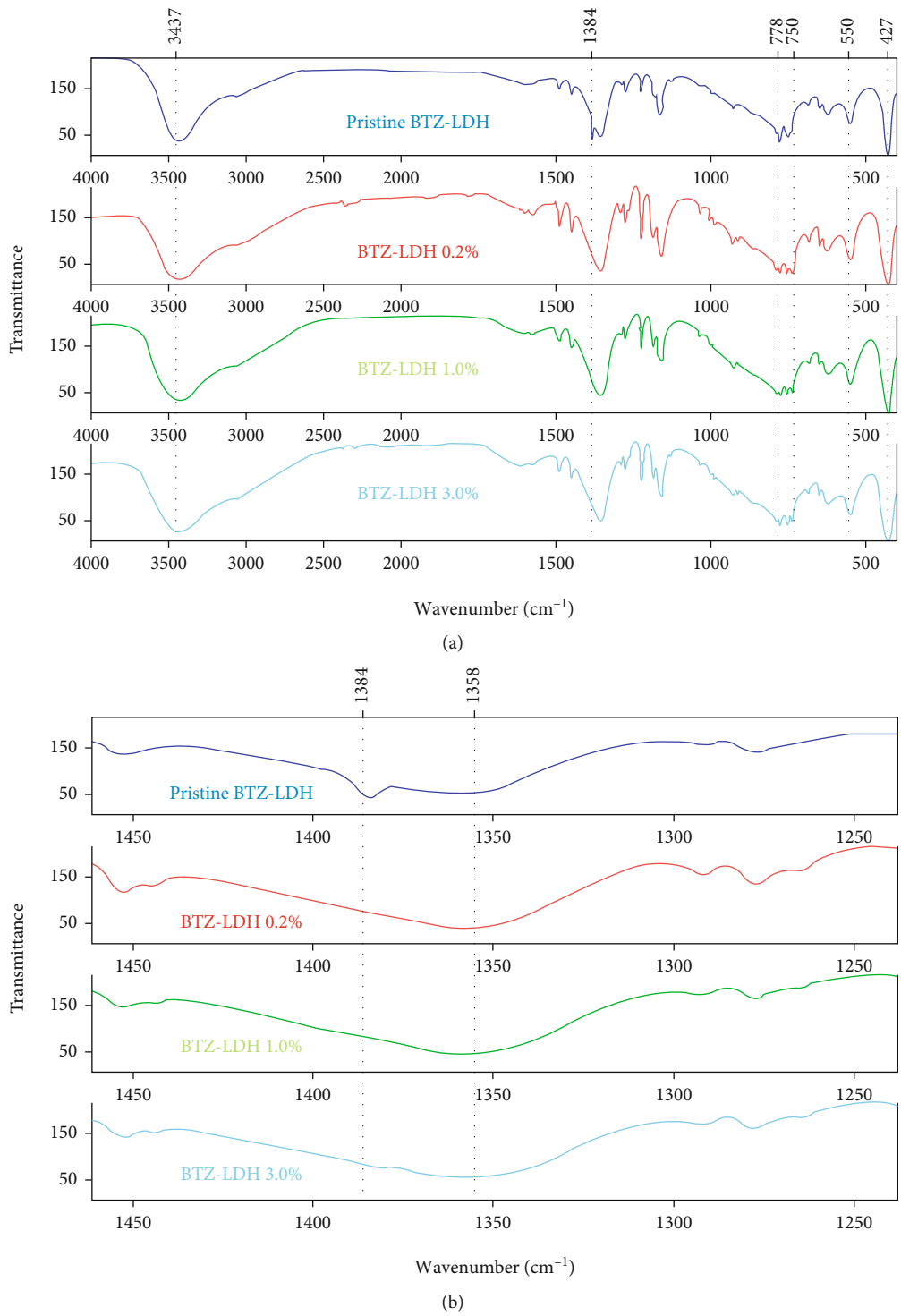

Figure 3: Comparative spectra of BTZ-LDH before and after exposure to 3.5% NaCl (a) spectrum in full and (b) zoom in the 1384 cm^{-1} region.

according to Equation (3).

$$a = 2d_{(110)}. \quad (2)$$

The parameter 'h', related to lamellar interstice size, was estimated by subtracting the value of hydroxide layer thickness (around 47.1 Å for Zn/Al LDH [18]) from 'd' basal space value.

The analysis and comparison of pristine LDHs with LDH after exposure to chloride-rich medium were made to verify structural changes associated with the ion exchange. Figure 5 shows the diffractogram obtained for NO_x-LDH before and after exposure to 3.5 wt% NaCl. The diffractogram

Table 2: Characteristic bands of FTIR spectrum obtained for BTZ-LDH.

Wavenumber (cm^{-1})	Assignment
3437	Adsorbed water molecules and hydroxyl groups in the structure [11]
1384*	Triazolic ring (from benzotriazole) [14]/nitrate symmetrical stretching* [11]
778**	Al-OH deformation [13]/out of plane C-H stretching (from benzotriazole)** [15]
750	Aromatic ring=C-H bond (benzotriazole) [16]
550	Zn/Al-OH translation [13]
427	Al-O condensed groups [13]

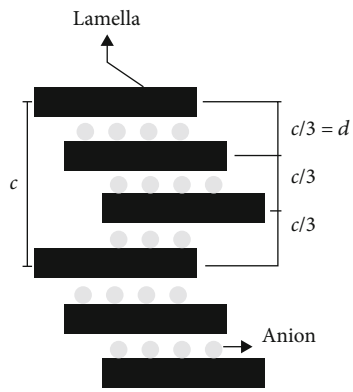

Figure 4: Relation between rhombohedral structure parameters for LDH. Adapted from Crepaldi and Valim (1998) [19].

presents characteristics of layered materials such as thin and intense peaks at low values of 2θ and less intense peaks (usually asymmetric) at higher values of 2θ. These are characteristics of hexagonal network systems with rhombohedral symmetry (R-3m special group), which are commonly used to describe LDH [20]. The NO_x-LDH diffractogram showed defined peaks at 11.32° and 23.10°, related to diffraction by planes (003) and (006), respectively. The diffractogram of NO_x-LDH before exposure to saline medium is quite similar to that reported on literature [8, 11, 21]. The maximum space that a nitrate ion can occupy is 3.80 Å [22]. The inorganic ions may be arranged between layers at different ways: perpendicularly, horizontally, or tilted at an angle [23], which may reduce the space occupied by these ions by some extension. Hence, the interlayer space value of 3.10 Å may be associated with a more compact orientation of nitrate ions, in addition to the presence of nitrite ions which tend to present a smaller spatial diameter.

XRD analysis was also employed as a complementary technique to FTIR to determine LDH efficiency to trap chloride ions. Table 3 shows the parameters calculated for LDH before and after exposure to the NaCl medium. Figure 5 shows a comparison between obtained diffractograms in both situations, and the region of $7° < 2\theta < 31°$ was enlarged to evidence changes on main peaks. Comparing the diffractograms obtained for NO_x-LDH before and after exposition, it is possible to observe displacement on (003) and (006) planes to higher 2θ values, which indicates a decrease on interlayer spacing according to Bragg's law. This result corroborates with the previous conclusion that the ion exchange was effective in this case, since chloride ions are smaller than nitrate/-nitrite ions, promoting layer structure contraction. In addition to that, no displacement was observed on the (110) plane, indicating that the nature of elements which comprise the layer structure (Zn and Al) did not change [18]. Figure 6 shows a schematic drawing of the ion-exchange process of NO_x-LDH when exposed to a saline medium.

Diffractogram obtained for BTZ-LDH is showed in Figure 7. The diffractogram of BTZ-LDH showed characteristic peaks of lamellar system. Basal spaces were calculated through the same methodology employed to NO_x-LDH, and Table 4 shows the obtained results. Comparison between diffractograms before and after exposure is showed in Figure 8. In this case, '*d*' and '*h*' parameters are quite similar to the values (7.56 Å and 2.85 Å, respectively) reported by Serdechnova and coworkers for the same material [18]. According to them, it would not be possible for the benzotriazole anion to locate in an interlayer space ('*h*') in the order of magnitude found in this case, due to the relatively big spatial volume of benzotriazole. Serdechnova and coworkers also investigated the insertion of benzotriazole in Mg/Al LDH and mercaptobenzotriazole in Zn/Al LDH. For both cases, the values obtained for '*d*' and '*h*' parameters were in the range of 15 Å and 11 Å, respectively. These results show that benzotriazole anions and its derivatives, like mercaptobenzotriazole, demand bigger interlayer space for their intercalation to be possible. In addition to that, the diffractogram in Figure 7 shows the presence of unknown peaks (identified with asterisks). Serdechnova and coworkers attributed these peaks to reaction products between LDH hydroxide layers and benzotriazole, since it is known that there is high affinity between benzotriazole and zinc and the tendency of them to form complexes [24]. Thus, it was concluded that the attempt to insert benzotriazole in pristine nitrogen oxides containing Zn/Al LDH resulted in partial decomposition of LDH, and the portion that remained intact may be filled with hydroxyls as the interlayer ion. Moreover, the comparison between the diffractograms obtained for BTZ-LDH before and after exposure did not show displacements on main peaks, indicating that the interlayer space did not change and, consequently, ion exchange did not seem to happen. Absence of displacement on the (110) peak indicated the permanence of Zn and Al in lamellar structure.

Those results, aligned to FTIR spectra, indicate that benzotriazole insertion as interlayer ion was not effective in the

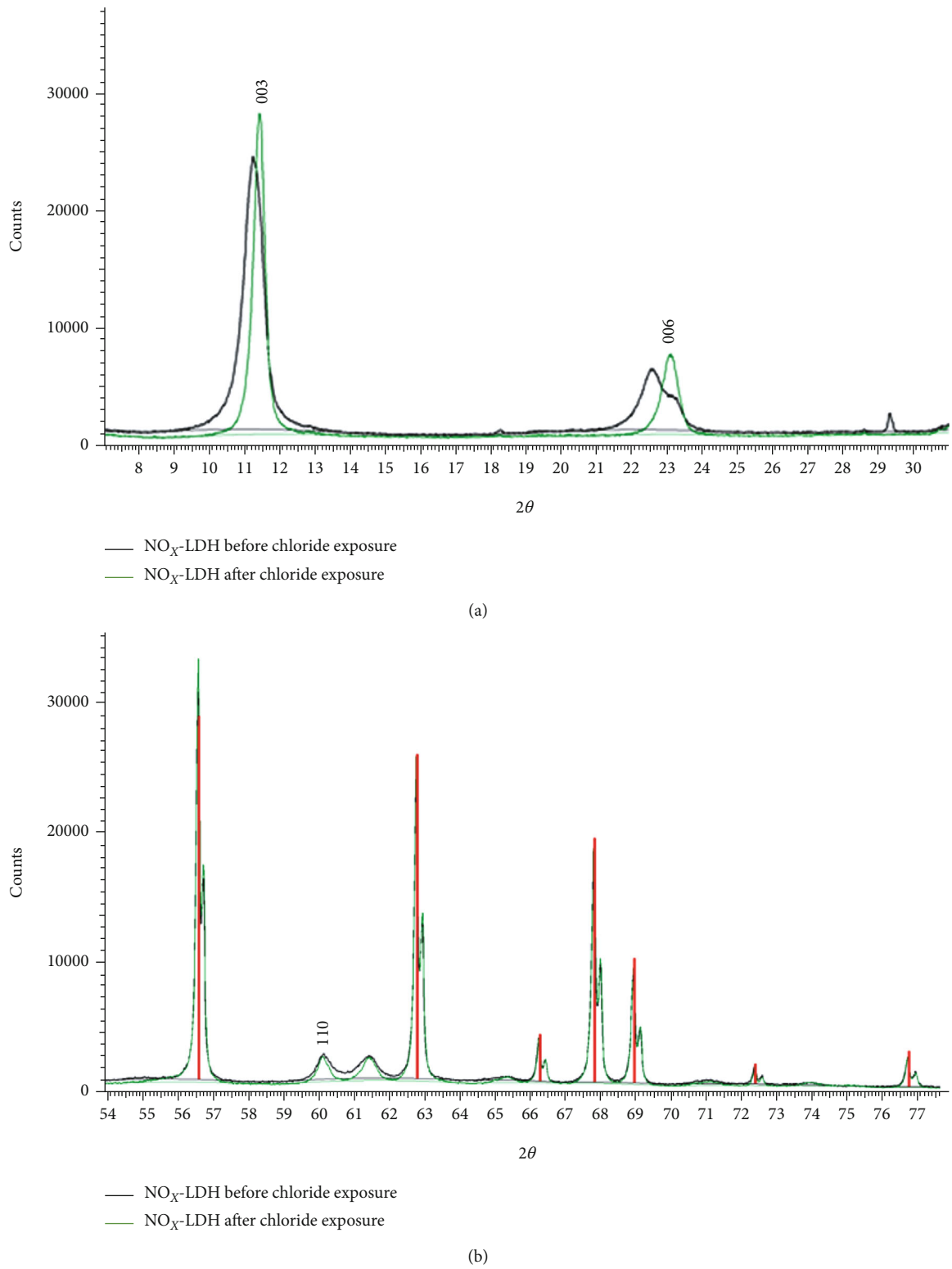

Figure 5: Diffractograms obtained for NO$_X$-LDH before (black) and after (green) exposure to 3.5% NaCl (a) region between 8 and 31° and (b) region between 54 and 77°. Peaks assigned with red risk are related to the standard ZnO added to the sample to the correction of peak position.

productive process of BTZ-LDH, resulting in the inefficiency of ion exchange when exposed to the saline medium. Figure 9 shows an illustrated scheme of proposed mechanism from the BTZ-LDH obtainment until its exposition to the saline medium. In Figure 9, pink rectangles, which represent benzotriazole molecules, appear anchored to the LDH structure, in an allusion to the possibility of them to be complexed with structural zinc.

Table 3: Structural parameters calculated for NO_x-LDH.

	d_{basal} (Å)	***h*** (Å)	***c*** (Å)	***a*** (Å)
Before Cl^- exposure	7.81	3.10	23.43	3.07
After Cl^- exposure	7.71	3.00	23.13	3.07

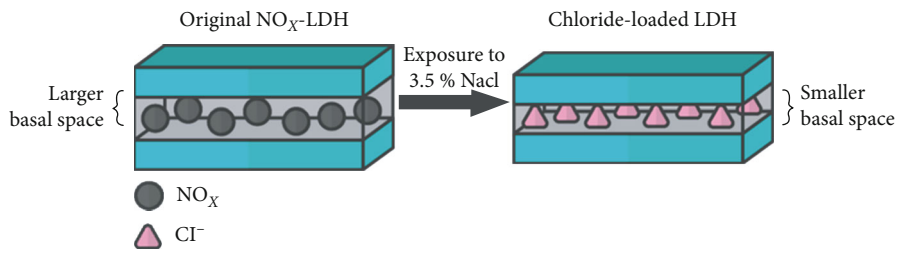

Figure 6: Schematic drawing of the ion-exchange process of pristine NO_x-LDH in 3.5% NaCl medium.

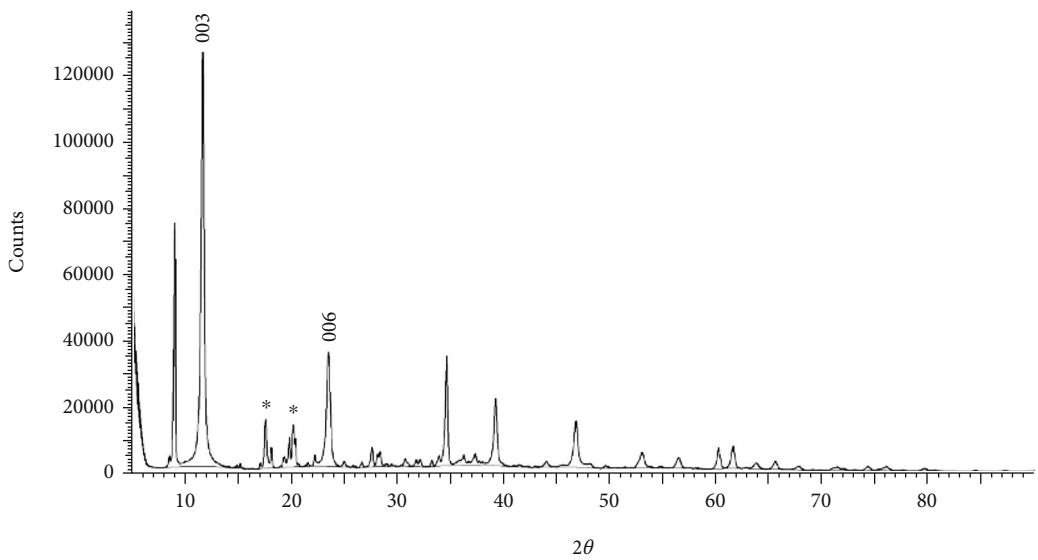

Figure 7: Diffractogram obtained for BTZ-LDH.

Table 4: Structural parameters calculated for BTZ-LDH.

	d_{basal} (Å)	*h* (Å)	*c* (Å)	*a* (Å)
Before Cl^- exposition	7.58	2.87	22.74	3.07
After Cl^- exposition	7.58	2.87	22.74	3.07

The low solubility of LDH in the neutral medium does not make it possible to evaluate its efficiency regarding active mechanism against corrosion through its direct insertion on the electrolyte, because particle decantation would lead to the formation of a film which would act as a physical passive barrier on the metal. Thus, a 'treatment' was made by putting LDH in a 3.5% NaCl solution to perform ion exchange; then, the LDH particles were removed. This approach allowed evaluation of each system efficiency on trapping chlorides and releasing inhibitor ions by avoiding factors, which may provide wrong results. Figure 10 shows OCP profiles of carbon steel 1020 for different systems employing LDH on extract form. OCP migrated to values that are more negative over immersion time for all systems, and this profile is a result of progressive penetration of the electrolyte in the metal and consequent increase of oxidized species concentration. For the control system (black curve), the initial value was -0.540 V, which decreased quickly to a stabilization value of -0.750 V. This value was reached after approximately 400 min (6 hours) of immersion, and the value stayed constant until the end of analysis. For NO_x-LDH systems, it was observed that all concentrations shifted OCP to nobler values, meaning that the higher the concentration, the greater the displacement. These results indicate that NO_x-LDH addition to the electrolyte was effective to decrease the aggressiveness of the medium through chloride entrapment. In addition to that, the late stabilization and irregular profile of decay may indicate the adsorption of inhibitor ions on metal surface.

BTZ-LDH systems showed decay profiles quite similar to those observed for the control system, with a slight increment

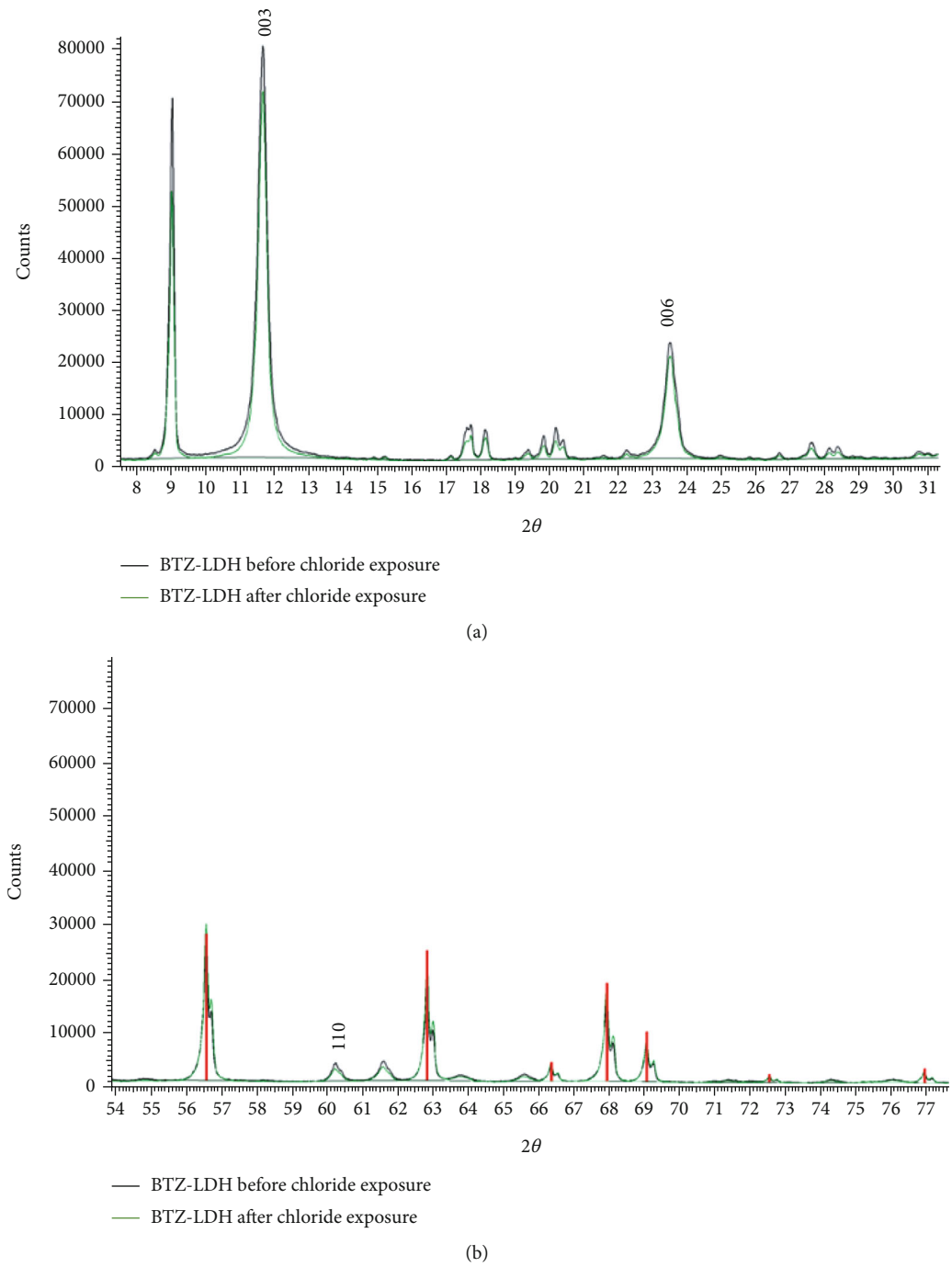

Figure 8: Diffractograms obtained for BTZ-LDH before (black) and after (green) exposure to 3.5% NaCl (a) region between 8 and 31° and (b) region between 54 and 77°. Peaks assigned with a red line are related to the standard ZnO added to the sample to the correction of peak position.

of OCP values to a nobler direction as long as the concentration increased. However, such increment was too subtle to be attributed to benzotriazole inhibitor release, especially in higher concentrations in which a more pronounced inhibitive effect would be expected. Thus, these results corroborate with what was said before about nonrelease of benzotriazole from LDH to act as corrosion inhibitor on a metal surface, meaning that the observed slight effect resulted in few remaining NO_x ions on LDH structure (as shown in Figure 9).

As better results were obtained for LDH extracts at 3.0%, potentiostatic polarization analyses were performed employing extracts in this concentration. Figure 11 shows obtained potentiostatic polarization curves, and electrochemical parameters obtained after Tafel extrapolation are tabulated in Table 5. Comparing blue and red curves in Figure 11, it was observed that the BTZ-LDH extract addition did not cause significant changes on sample behavior in comparison with the control system, indicating again that in this case,

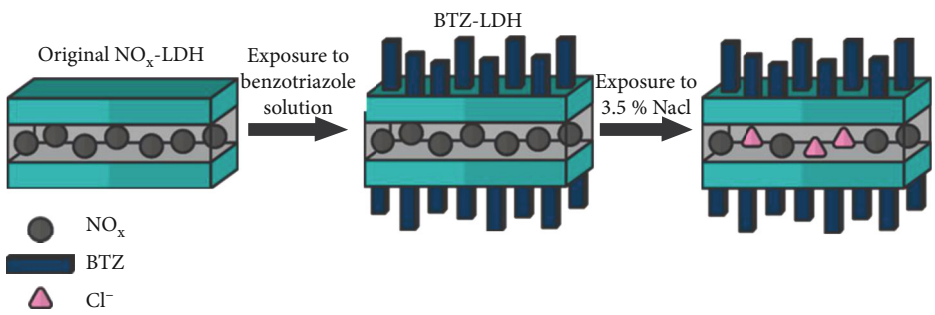

Figure 9: Schematic drawing of ion-exchange process from pristine NO$_x$-LDH until BTZ-LDH obtainment and its posterior exposition to 3.5% NaCl medium.

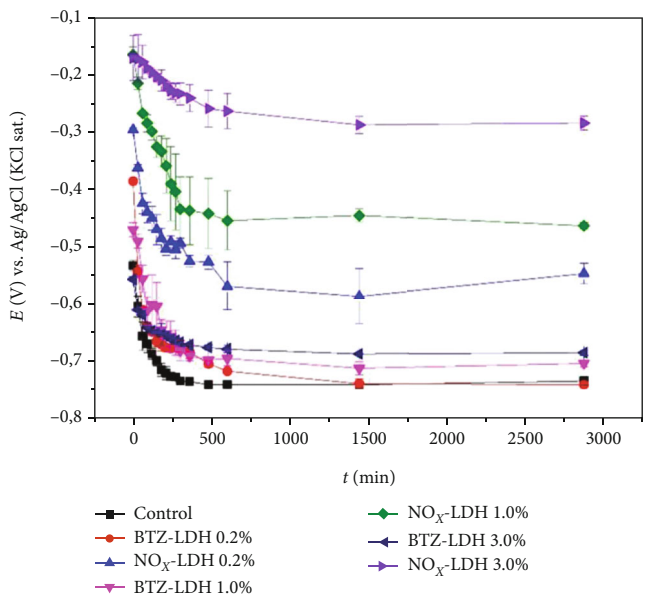

Figure 10: OCP profiles obtained for extract form LDH systems.

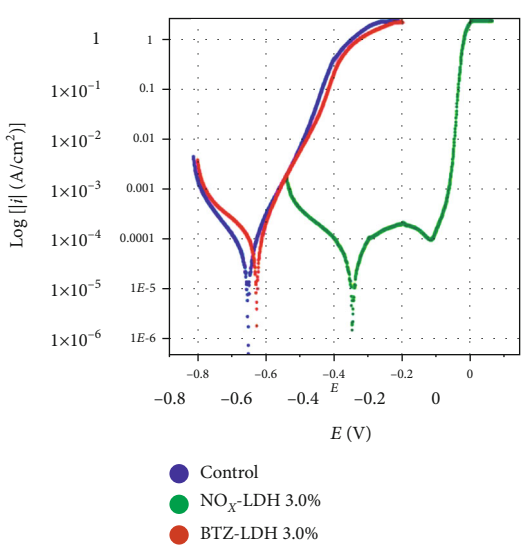

Figure 11: Potentiostatic polarization curves obtained for different LDH extract systems (E vs. Ag/AgCl reference electrode and scanning speed of 1 mV·s^{-1}).

Table 5: Electrochemical parameters obtained from polarization curves for carbon steel samples.

Extract	E_{corr} (V)	i_{corr} (μA·cm^{-2})	cr (10^{-4} mm·d^{-1})	R_{pol} (Ω·cm^2)
Control	-0.650	3.36	1.07	330.84
BTZ-LDH	-0.626	9.01	48.77	182.51
NO$_x$-LDH	-0.345	3.56	1.10	533.00

there was not enough inhibitor ion concentration on electrolyte. Values reported on Table 5 show that current density (i_{corr}) suffered an increase in the presence of the BTZ-LDH extract, as well as corrosion rate (cr). Polarization resistance (R_{pol}) suffered a decrease in comparison to the control system. These results indicate that the BTZ-LDH extract system becomes more susceptible to corrosion than the control system. For the NO$_x$-LDH system, displacements of both

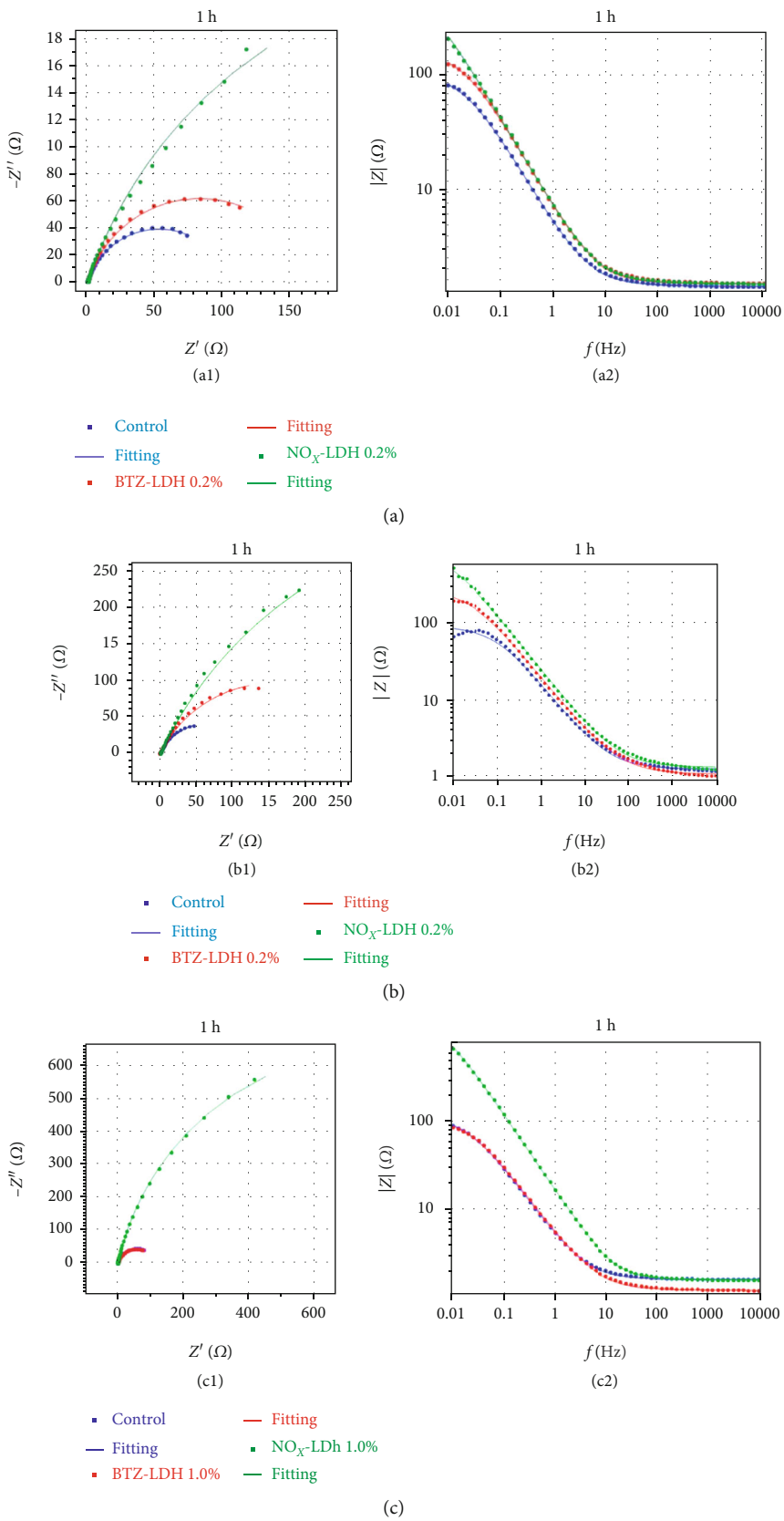

Figure 12: Nyquist plots (1) and Bode modulus plots (2) obtained for systems containing (a) 0.2%, (b) 1.0%, and (c) 3.0% extracts after 1 h of immersion (exposed area: 17 cm^2).

portions (anodic and cathodic) of polarization curve to less negative potential values were observed. This system showed a well-defined passivation region, showing the action of inhibitor ions on the formation of a barrier on metal sites. In this case, polarization resistance suffered an increment of around 1.6 times. Corrosion current and corrosion rate remained equivalent to those of the control system.

Electrochemical impedance spectroscopy (EIS) analyses were made as an additional technique to obtain information about corrosion resistance of different systems. Figure 12 shows obtained results for extract systems at different concentrations after 1 h of immersion. Scattered points represent experimental data, and lines represent fitting. All curves of Figure 12 were fitted to an $R(RQ)$ equivalent circuit, as shown on Figure 13.

The equivalent circuit in Figure 13 is known as the Randles circuit and is commonly employed to describe uncoated metals exposed to an electrolyte [25, 26]. In this model, there is only one time constant, referring to the metal-electrolyte interface. In this way, R_s element refers to uncompensated resistance between work and reference electrodes and refers to electrolyte resistance [27]. R_{ct} element refers to charge transference resistance, and Q_{dl} element (constant phase element) refers to double-layer capacitance ('dl' subscribed index). In real systems, the change of a pure capacitive element for a constant phase element usually facilitates curve fitting, because this element describes semicircles flattening better. Constant phase elements are expressed by Equation (3) [27].

$$Q = \frac{1}{Y_0 (j\omega)^N}. \quad (3)$$

Q_{dl} has two components, being Y_0 an element referred to admittance and N a dimensionless exponent, where $N = 1$ represents an ideal capacitor [25]. j is a complex number ($j^2 = -1$), and ω is the angular frequency ($\omega = 2\pi f$).

Table 6 shows obtained values for parameters after graph adjustment to equivalent circuit. R_{ct} values of the BTZ-LDH system showed slight increases in comparison to the control system on 0.2% and 1.0%, which reveals a discreet increasing on corrosion protection performance. For 3.0% concentration, the R_{ct} value of the BTZ-LDH system was slightly smaller than the control system's. These results indicated that BTZ-LDH was not efficient on promoting carbon steel protection against corrosion on extract tests.

Regarding NO_x-LDH, significant increases on R_{ct} values in comparison with control system were observed. The biggest increase was observed in the 3.0% NO_x-LDH system. This result suggests that nitrate/nitrite ions initially free in solution were efficient in adsorbing on the metal surface in sufficient amount, blocking metal sites, and decreasing corrosive processes development. Values for N (Q_{dl}) components showed essentially equivalents for all systems. In this case, as there is no coating applied on the substrate, this parameter may be related to metallic surface morphology. As all bodyproofs had the same composition and received the same previous treatment (sanding and degreasing), this result is coherent.

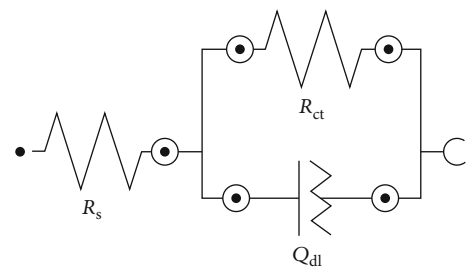

Figure 13: Equivalent circuit $R(RQ)$ fitted on EIS results for extract systems.

Table 6: Values of parameters obtained through attribution of EIS results to equivalent circuits.

Concentration	System	OCP (V)	R_s (Ω)	R_{ct} (Ω)	Y_0 (Q_{dl}) (mS)	N (Q_{dl})
0.2%	Control	-0.667	1.43	105	49.3	0.804
	BTZ-LDH	-0.660	1.50	165	33.8	0.815
	NO_x-LDH	-0.507	1.50	630	34.8	0.796
1.0%	Control	-0.662	1.23	80	15.1	0.751
	BTZ-LDH	-0.663	1.04	310	13.8	0.709
	NO_x-LDH	-0.328	1.29	1000	10.8	0.721
3.0%	Control	-0.699	1.65	120	46	0.81
	BTZ-LDH	-0.692	1.25	117	43.5	0.793
	NO_x-LDH	-0.122	1.65	1600	12.1	0.865

Initially, it could be considered that the development of corrosive processes on bodyproofs over the exposure time would lead to the formation of a new interface (electrolyte-corrosion products). However, this behavior was not evidenced by EIS measurements, since all results were satisfactorily adjusted to $R(RQ)$ circuits. A reason for this behavior may be the fact that bodyproofs were uncoated metals, leading the corrosion products to leave the metal surface and migrate to the medium due to its low substrate adherence. This dynamic process would avoid the formation of a properly new interface, justifying the obtained result. Figure 14 shows a schematic drawing of the proposed mechanism.

Therefore, there are evidences that NO_x ions protected the metallic surface mainly through competitive adsorption with chloride ion mechanism and not through stabilization of formed oxides. Considering the results obtained on extract tests, incorporation of LDH in an organic coating matrix was accomplished by employing only NO_x-LDH. Figure 15 shows EIS results for carbon steel samples coated with NO_x-LDH-enriched primer in three different concentrations. The 0.2% NO_x-LDH system presented very particular behavior, with

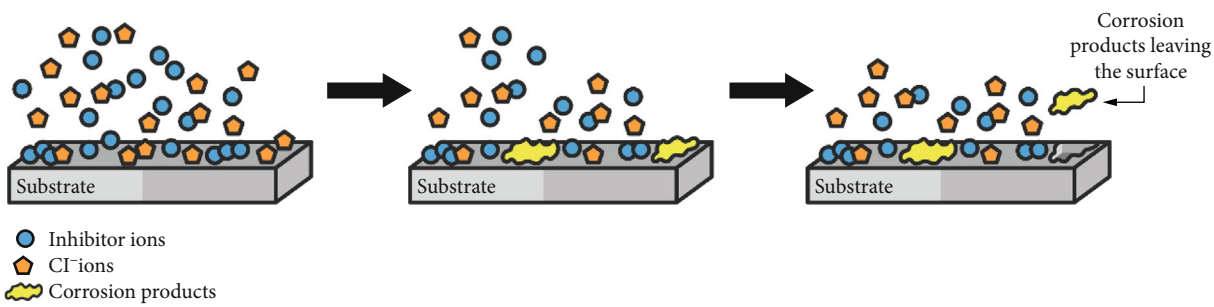

Figure 14: Schematic drawing of proposed processes of formation and migration of corrosion products on metallic surface without coating.

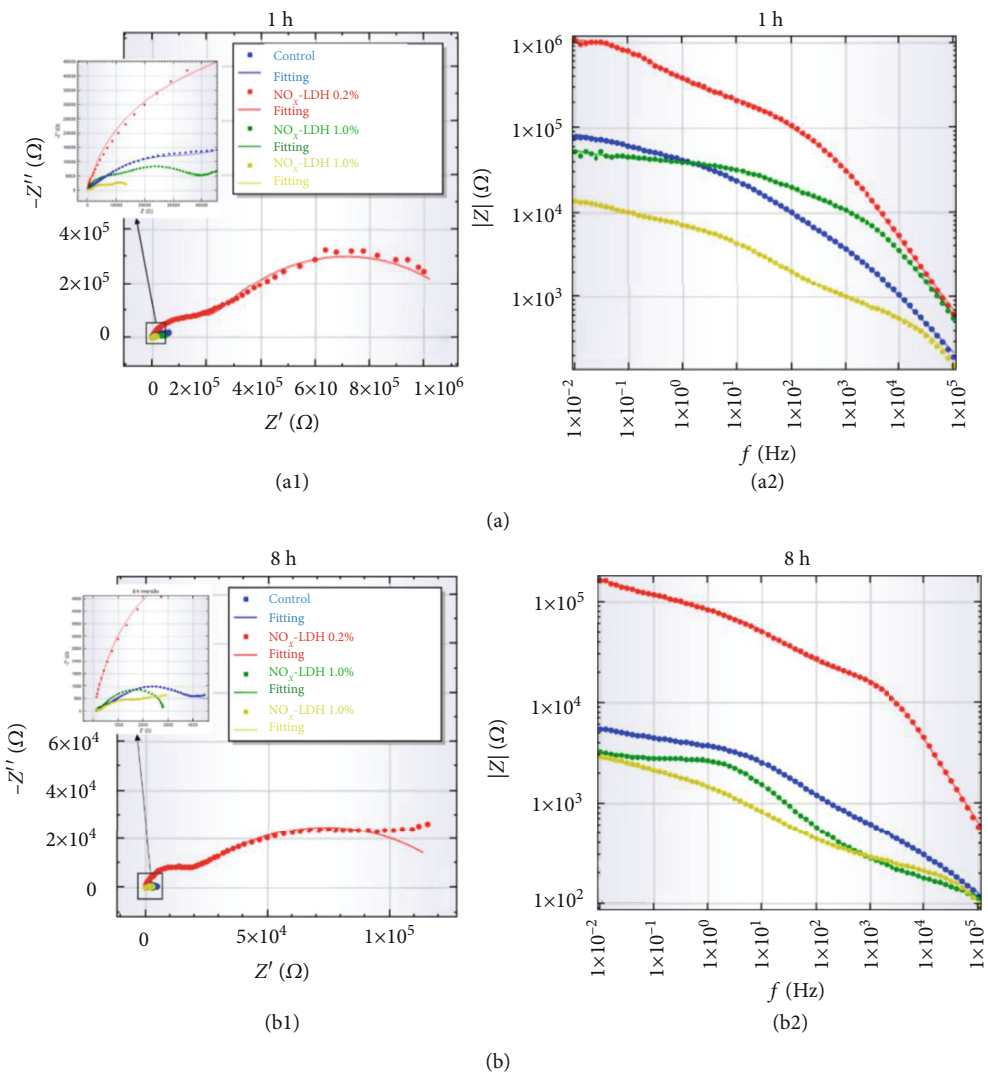

Figure 15: Nyquist plots (1) and Bode modulus plots (2) for coated systems after (a) 1 h and (b) 8 h of immersion (exposed area: 17 cm^2).

total impedance values higher than other systems. In this case, a $R(RQ)(RQ)$ circuit fit all experimental data. In the carbon steel samples coated with a primer layer, there was the presence of a coating-electrolyte interface (beyond metal-electrolyte interface already identifiable due to primer porosity), characterizing two time constants of two (RQ) pairs. In this circuit, beyond R_s and R_{ct} (parameters described above), there is the presence of a R_{coat}. Capacitive elements in this case were related to coating capacitance (Q_{coat}) and double-layer capacitance (Q_{dl}). Unlike in extract tests (where corrosion products showed low adherence on substrate and migrated to the medium), the formation of a new time constant was observed in this case, suggesting the presence of a new interface on the system. As the reference primer was

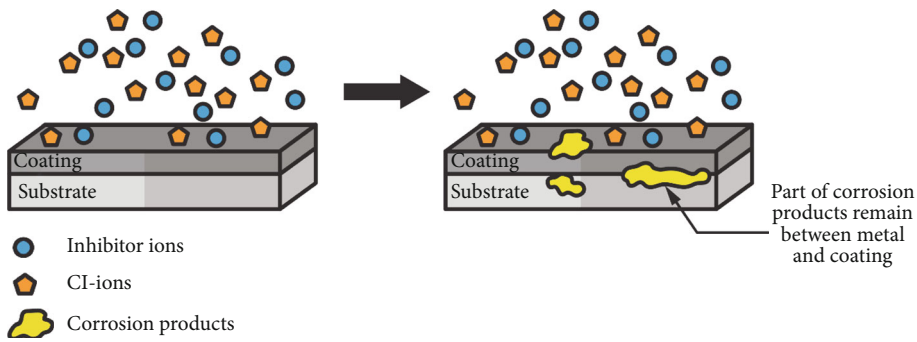

Figure 16: Proposed scheme for the formation and trapping processes of corrosion products at the substrate-coating interface.

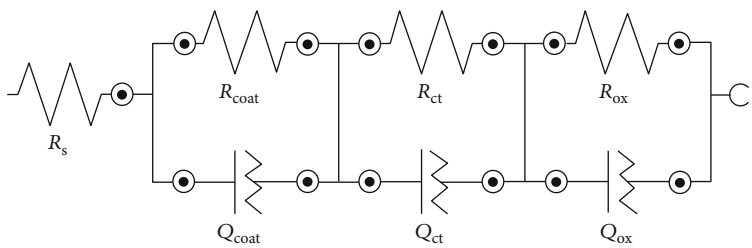

Figure 17: $R(RQ)(RQ)(RQ)$ equivalent circuit attributed to EIS results for samples coated with NO_x-LDH-enriched primer.

Table 7: Electrochemical parameters obtained after fitting EIS data of coated samples to equivalent circuit $R(RQ)(RQ)(RQ)$.

	Control		0.2%		1.0%		3.0%	
Immersion time (h)	1	8	1	8	1	8	1	8
OCP (V)	-0.447	-0.482	-0.503	-0.484	-0.472	-0.560	-0.515	-0.529
R_{coat} (kΩ)	60.7	11.6	1030	134	28.1	4.29	9.17	6.16
Y_0 (Q_{coat}) (μS)	23.1	1400	1.21	25	64.1	843	315	660
N (Q_{coat})	0.585	0.419	0.673	0.557	0.534	0.171	0.593	0.278
R_{ct} (kΩ)	31.1	3.35	150	66.8	27.5	1.09	7.31	0.697
Y_0 (Q_{dl}) (μS)	2.14	22.3	0.0726	1.34	0.869	25.7	16.7	199
N (Q_{dl})	0.634	0.616	0.842	0.64	0.659	1.02	0.55	0.662
R_{ox} (kΩ)	2.77	0.504	50	16.3	8.73	0.801	0.613	0.124
Y_0 (Q_{ox}) (μS)	0.366	5.90	0.0152	0.0109	0.0236	27.3	0.217	0.091
N (Q_{ox})	0.762	0.568	0.894	0.913	0.862	0.766	0.766	0.915

relatively porous and the layer was not that thick, the occurrence of electrolyte penetration through the coating layer and the consequent formation of a layer of corrosion products between metal and primer were admitted. It was then considered that the primer layer was efficient on trapping corrosion products reducing its migration to medium and forming a layer identifiable by EIS technique. Figure 16 shows a representative scheme of this hypothesis.

Thus, after some time of immersion, the appropriate equivalent circuit was $R(RQ)(RQ)(RQ)$, where the new (R Q) pair (R_{ox} and Q_{ox}) refers to the corrosion product layer as shown in Figure 17. Values of electrochemical parameters obtained by fitting EIS data to equivalent circuit are shown in Table 7. OCP values were similar on all cases. Regarding R_{coat}, a decrease of values in all systems was observed as long as the immersion time increased, with this being a result of progressive penetration of electrolyte through coating pores. The NO_x-LDH 0.2% system showed R_{coat}, R_{ct}, and R_{ox} significantly increased in comparison to other systems over the time period investigated. These results suggest that NO_x-LDH insertion in this concentration promoted an improvement on primer's barrier properties, increasing the resistance to electrolyte passage and to the development of corrosive processes on metal. R_{ox} increment of values on concentration of 0.2% may be explained by the action of inhibitors on stabilization and increase of adherence of corrosion products on coating matrix, with this being one mechanism of action of anodic inhibitors. For other systems (NO_x-LDH at 1.0% and 3.0%), a tendency of resistance values decreasing in the order control >1.0% > 3.0% was observed. These results

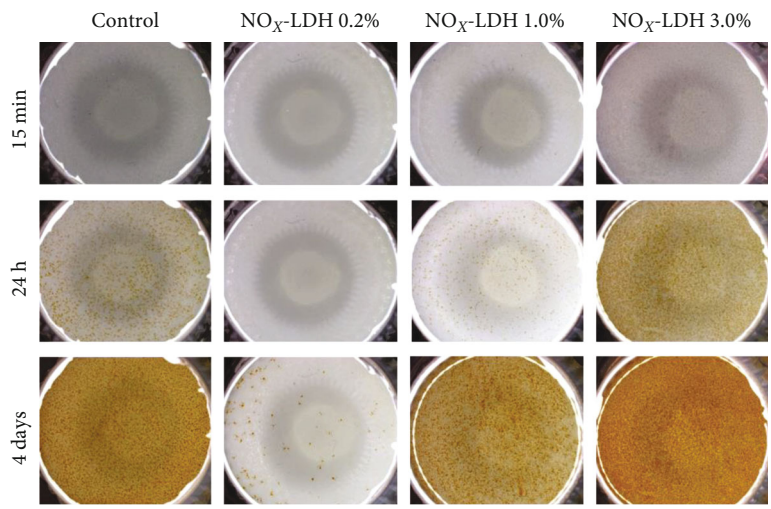

Figure 18: Physical aspect of metallic surfaces coated using primer with and without NO_x-LDH during immersion time.

indicate that higher concentrations of LDH on primer may cause an increase in porosity, harming original barrier properties. In this case, the protective effect conferred by NO_x-LDH would be compromised or even canceled by the increase of electrolyte permeability, resulting on less effective protection than on the control medium. Another parameter employed to measure the influence of LDH addition on coating matrix was $Y_0\,(Q_{coat})$ values. The increase of these values along time indicates progressive delamination of coating from the metallic surface [27]. Thus, a lower increment on $Y_0\,(Q_{coat})$ values observed for coating containing 0.2% of NO_x-LDH indicates improvement on adhesion of primer on substrate in this case in comparison with other systems, where $Y_0\,(Q_{coat})$ values suffered higher increments. These results indicate that LDH addition on primer was efficient only in the lower investigated concentration, which was capable of improving barrier properties conferring higher protection to metal. NO_x-LDH addition at 1.0% did not show significant differences in comparison with control system, whereas the 3.0% addition clearly made the coating more susceptible to electrolyte penetration, as since the beginning of exposure, this system showed quite lower values for total impedance.

Figure 18 shows images of the physical aspect of surfaces coated using primer with and without NO_x-LDH during immersion time. These images corroborate with EIS results, indicating the high corrosion inhibition capacity of the system containing 0.2% of NO_x-LDH in comparison with other systems. After 24 h of immersion, control, 1.0%, and 3.0% systems already showed corrosion product formation in significant amounts, whereas the 0.2% system remained intact. After 4 days of exposure, control, 1.0%, and 3.0% systems were completely recovered by corrosion products and the 0.2% system showed some isolated points of corrosion (moreover in low amount than other systems after only 24 h).

4. Conclusions

LDH containing two different corrosion inhibitors (benzotriazole and nitrogen oxides) were characterized, and their ability to promote autonomic protection against corrosion was evaluated. Chemical analyses indicated that benzotriazole was not found as interlamellar ion in BTZ-LDH (therefore unavailable for ionic change) as it might adsorb to structural Zn. XRD results also confirmed that the identified interlamellar space would be incompatible to benzotriazole ion size. For NO_x-LDH, it was identified that nitrogen oxides were satisfactorily intercalated and available for ion change. Performance tests in extract form showed that BTZ-LDH did not show any significant protection in comparison with control system, not even at elevated concentration. For NO_x-LDH, a higher protection of metal in comparison with control system was observed and was proportional to the concentration of extract. In NO_x-LDH-incorporated organic coating, the existence of an optimum concentration of NO_x-LDH to enhance the protection against corrosion without impairing original barrier properties of coating was observed. The concentration, which better balanced the benefic action of NO_x-LDH with the deleterious effect of porosity increase of coating, was 0.2%.

It was concluded that NO_x-LDH comprised a good alternative as anticorrosive additive and self-healing action on corrosion protection. As complementary future studies, it is suggested to investigate optimal concentration around 0.2% (as 0.05%, 0.1%, and 0.15%, for example) of NO_x-LDH in the organic coating matrix, to optimize the minimum amount required to provide protection effects similar to what was observed at 0.2%.

Data Availability

The data used to support the findings of this study are available from the corresponding author upon request.

Conflicts of Interest

The authors declare that they have no conflicts of interest.

References

[1] To Thi Xuan Hang, T. A. Truc, N. T. Duong, N. Pébère, and M.-G. Olivier, "Layered double hydroxides as containers of inhibitors in organic coatings for corrosion protection of carbon steel," *Progress in Organic Coatings*, vol. 74, no. 2, pp. 343–348, 2012.

[2] X. Guo, F. Zhang, D. G. Evans, and X. Duan, "Layered double hydroxide films: synthesis, properties and applications," *Chemical Communications*, vol. 46, no. 29, pp. 5197–5210, 2010.

[3] X. Yuan and W. Li, "Graphitic-C 3 N 4 modified ZnAl-layered double hydroxides for enhanced photocatalytic removal of organic dye," *Applied Clay Science*, vol. 138, pp. 107–113, 2017.

[4] E. Alibakhshi, E. Ghasemi, M. Mahdavian, and B. Ramezanzadeh, "A comparative study on corrosion inhibitive effect of nitrate and phosphate intercalated Zn-Al- layered double hydroxides (LDHs) nanocontainers incorporated into a hybrid silane layer and their effect on cathodic delamination of epoxy topcoat," *Corrosion Science*, vol. 115, pp. 159–174, 2016.

[5] J. Tedim, M. L. Zheludkevich, A. N. Salak, A. Lisenkov, and M. G. S. Ferreira, "Nanostructured LDH-container layer with active protection functionality," *Journal of Materials Chemistry*, vol. 21, no. 39, p. 15464, 2011.

[6] M. L. Zheludkevich, S. K. Poznyak, L. M. Rodrigues et al., "Active protection coatings with layered double hydroxide nanocontainers of corrosion inhibitor," *Corrosion Science*, vol. 52, no. 2, pp. 602–611, 2010.

[7] N. Y. Abu-Thabit and A. S. Hamdy, "Stimuli-responsive polyelectrolyte multilayers for fabrication of self-healing coatings - a review," *Surface and Coatings Technology*, vol. 303, pp. 406–424, 2016.

[8] M. L. Zheludkevich, J. Tedim, and M. G. S. Ferreira, ""Smart" coatings for active corrosion protection based on multifunctional micro and nanocontainers," *Electrochimica Acta*, vol. 82, pp. 314–323, 2012.

[9] T. T. X. Hang, T. A. Truc, N. T. Duong, P. G. Vu, and T. Hoang, "Preparation and characterization of nanocontainers of corrosion inhibitor based on layered double hydroxides," *Applied Clay Science*, vol. 67-68, pp. 18–25, 2012.

[10] J. Tedim, S. K. Poznyak, A. Kuznetsova et al., "Enhancement of active corrosion protection via combination of inhibitor-loaded nanocontainers," *ACS Applied Materials & Interfaces*, vol. 2, no. 5, pp. 1528–1535, 2010.

[11] Y. Dong, F. Wang, and Q. Zhou, "Protective behaviors of 2-mercaptobenzothiazole intercalated Zn–Al-layered double hydroxide coating," *Journal of Coatings Technology and Research*, vol. 11, no. 5, pp. 793–803, 2014.

[12] F. A. Miller and C. H. Wilkins, "Infrared spectra and characteristic frequencies of inorganic ions," *Analytical Chemistry*, vol. 24, no. 8, pp. 1253–1294, 1952.

[13] F. Z. Mahjoubi, A. Khalidi, M. Abdennouri, and N. Barka, "Zn–Al layered double hydroxides intercalated with carbonate, nitrate, chloride and sulphate ions: synthesis, characterisation and dye removal properties," *Journal of Taibah University for Science*, vol. 11, no. 1, pp. 90–100, 2018.

[14] Y. H. Lei, N. Sheng, A. Hyono, M. Ueda, and T. Ohtsuka, "Effect of benzotriazole (BTA) addition on polypyrrole film formation on copper and its corrosion protection," *Progress in Organic Coatings*, vol. 77, no. 2, pp. 339–346, 2014.

[15] K. Dokken, L. C. Davis, L. E. Erickson, and S. Castro, "Fourier-Transform Infrared Spectroscopy As a Tool To Monitor Changes in Plant Structure in Response To Soil Contaminants," *Proceedings-water research Technology*, vol. 2002, p. 1, 2002.

[16] M. Miao, X.-Y. Yuan, X.-G. Wang, Y. Lu, and J.-K. Liu, "One step self-heating synthesis and their excellent anticorrosion performance of zinc phosphate/benzotriazole composite pigments," *Dyes and Pigments*, vol. 141, pp. 74–82, 2017.

[17] W. D. Callister Jr., *Ciencia e Engenharia dos materiais: Uma introdução*, vol. 589, John Wiley & Sons, Hoboken, NJ, USA, 2002.

[18] M. Serdechnova, A. N. Salak, F. S. Barbosa et al., "Interlayer intercalation and arrangement of 2-mercaptobenzothiazolate and 1,2,3-benzotriazolate anions in layered double hydroxides: in situ X-ray diffraction study," *Journal of Solid State Chemistry*, vol. 233, pp. 158–165, 2016.

[19] E. L. Crepaldi and J. B. Valim, "Hidróxidos duplos lamelares: síntese, estrutura, propriedades e aplicações," *Quimica Nova*, vol. 21, no. 3, pp. 300–311, 1998.

[20] F. Cavani, F. Trifiro, and A. Vaccari, "Hydrotalcite-type anionic clays: preparation, properties and applications," *Catalysis Today*, vol. 11, no. 2, pp. 173–301, 1991.

[21] H. Hayatdavoudi and M. Rahsepar, "Smart inhibition action of layered double hydroxide nanocontainers in zinc- rich epoxy coating for active corrosion protection of carbon steel substrate," *Journal of Alloys and Compounds*, vol. 711, pp. 560–567, 2017.

[22] G. G. C. Arizaga, A. S. Mangrich, J. E. F. da Costa Gardolinski, and F. Wypych, "Chemical modification of zinc hydroxide nitrate and Zn-Al-layered double hydroxide with dicarboxylic acids," *Journal of Colloid and Interface Science*, vol. 320, no. 1, pp. 168–176, 2008.

[23] T. Nogueira, N. Gonçalves, R. Botan, F. Wypych, and L. Lona, "Layered double hydroxides as fillers in poly(l-lactide) nanocomposites, obtained by in situ bulk polymerization," *Polímeros*, vol. 26, no. 2, pp. 106–114, 2016.

[24] J. V. Custódio, S. M. L. Agostinho, and A. M. P. Simões, "Electrochemistry and surface analysis of the effect of benzotriazole on the cut edge corrosion of galvanized steel," *Electrochimica Acta*, vol. 55, no. 20, pp. 5523–5531, 2010.

[25] D. A. Leal, I. C. Riegel-Vidotti, M. G. S. Ferreira, and C. E. B. Marino, "Smart coating based on double stimuli-responsive microcapsules containing linseed oil and benzotriazole for active corrosion protection," *Corrosion Science*, vol. 130, 2018.

[26] A. R. Deip, *Estudo da eficiência de proteção contra a corrosão em aço aisi 1020 utilizado na indústria petroquímica empregando revestimentos inteligentes: incorporação de trocadores iônicos do tipo hdl-bta em matriz epoxídica*, Digital Dissertation from DSpace software, 2017, https://hdl.handle.net/1884/54536.

[27] A. Amirudin, C. Barreau, R. Hellouin, and D. Thierry, "Evaluation of anti-corrosive pigments by pigment extract studies, atmospheric exposure and electrochemical impedance spectroscopy," *Progress in Organic Coatings*, vol. 25, no. 4, pp. 339–355, 1995.